Novel resonant and light-guiding phenomena in photonics

by

Rafif E Hamam

B.S. Physics, American University of Beirut (2004)

Submitted to the Department of Physics
in partial fulfillment of the requirements for the degree of

Doctor of Philosophy in Physics

at the

MASSACHUSETTS INSTITUTE OF TECHNOLOGY

September 2010

Author .....
Department of Physics
July 20, 2010

Certified by .....
Marin Soljačić
Associate Professor of Physics and MacArthur Fellow
Thesis Supervisor

Accepted by .....
Professor Krishna Rajagopal
Associate department Head for Education

Novel resonant and light-guiding phenomena in photonics

by

Rafif E Hamam

Submitted to the Department of Physics
on July 20, 2010, in partial fulfillment of the
requirements for the degree of
Doctor of Philosophy in Physics

Abstract

We investigate theoretically five novel resonant and light-guiding photonics phenomena.

First, we develop a universal coupled mode theory (CMT) treatment of the free-space scattering of waves from resonant objects. This analytical framework very accurately models the scattering and absorption cross sections, as long as the resonant scatterer has spherical/cylindrical symmetry, or is sufficiently smaller than the resonant wavelength of the incident wave. We apply it to study the scattering of light from spherically symmetrical resonant objects and atoms, and also the neutron scattering off nuclei.

Then, we propose an efficient weakly-radiative Wireless Energy Transfer (WET) scheme between two identical classical resonant objects, strongly coupled to an intermediate one having the same resonance frequency. The transfer mechanism, analyzed by CMT, relies on the adiabatic evolution of a dark eigenstate of the 3-object system. We explore its performance in various parameter regimes, and illustrate it by witricity-type WET between resonant inductively-coupled capacitively-loaded metallic loops.

Third, we develop an analytical CMT model for the electric field generated by an arbitrary polarization source in a general photonic structure (that could involve loss, gain and/or nonlinearities). Based on this model, we investigate the criteria for enhancing the efficiency of nonlinear effects, and produce efficient terahertz sources. The results, validated by Finite-Difference Time-Domain (FDTD) calculations, suggest that this approach could potentially be a substitute for the more numerically intensive FDTD method.

Next, we propose a 2D PhC structure that supports super-collimation over a large frequency range. We theoretically and numerically investigate the collimation mechanism in this 2D structure, in comparison to that of two other frequently used related PhC structures. We also point out the potential importance of this structure in designing super-collimation-based devices for monochromatic and polychromatic light.

Finally, we present numerical simulations of anisotropic multilayers that strongly

discriminate certain incidence angles of light, over a broad range of frequencies and irrespective of polarization. Such systems could improve the efficiency of solar cells.

Thesis Supervisor: Marin Soljačić
Title: Associate Professor of Physics and MacArthur Fellow

Acknowledgments

I would like to express my deepest and most sincere gratitude to Prof. Marin Soljačić, my research supervisor, for his wonderful and dedicated supervision and for all the encouragement and invaluable support especially at difficult times. I am also thankful to Marin's advice and guidance on the personal and career level. Without Marin's help, this thesis wouldn't have been possible. I would also like to especially thank Prof. John Joannopoulos for the great support and precious advice. It has been truly an honor for me to get this chance.

I would like to acknowledge the tremendous help of Dr. Peter Bermel and Prof. Steven Johnson, especially in computational issues. I would also like to thank my colleagues and collaborators from the Joannopoulos, Johnson, and Soljacic groups, including Dr. Aristeidis Karalis, Dr. Mihai Ibanescu, Dr. Björn Maes, Dr. Chiyan Luo, Dr. Jorge Bravo-Abad, Dr. David Chan, Andre Kurs, Dr. Yidong Chong, Dr. Alejandro Rodriguez and Dr. Ardavan Farjadpour. I am also thankful to Dr. Ivan Celanovic for the fruitful discussions, and also to Prof. Erich Ippen and Dr. Peter Rakich. I extend my thanks to all the Condensed Matter Theory and Physics Community at MIT, especially to Prof. Patrick Lee, Prof. Xiao-Gang Wen, and to Margaret O'Meara.

I am particularly grateful to Prof. Nuh Gedik for serving on my thesis committee, and also to my Fulbright and international student advisors and to the coordinators of the Fulbright program who awarded me this fellowship.

Finally, I dedicate this thesis to my loving parents and family for the wonderful support, attention, and sacrifice. Without their encouragement and guidance, and without supportive friends and relatives, I wouldn't have been here.

Contents

List of Figures

List of Tables

Chapter 1

Introduction

Resonant and light guiding phenomena play a primordial role in photonics both from a fundamental science perspective and from the stand point of technological applications. In fact, the advances in nanoparticles research [1], nonlinear optics [2], and photonic crystals [3], have generated an intense scientific interest in the exploration of novel photonics phenomena especially those involving resonances and light guiding. Moreover, advances in our understanding of the basic physics principles underlying these two classes of phenomena has paved the way for a wealth of important technological applications ranging from the design of devices for communication, computing, and for wireless energy transfer, to the design of efficient terahertz sources and detectors, and also for promising biomedical technologies.

In this thesis, we theoretically explore five novel photonics phenomena involving resonances and light guiding. Given the tremendous success of temporal coupled-mode theory (CMT)[4] in modeling systems involving weakly coupled well-defined resonances, a description of the resonant phenomena studied in this thesis in the framework of CMT is therefore very natural and effective. The light guiding phenomena will be investigated by using techniques more suitable for describing light propagation, such as the beam propagation method (BPM), the transfer matrix method (TMM) [5], and the Finite-Difference Time Domain (FDTD) [6] method.

The first resonance phenomenon concerns the free-space scattering of waves from resonant objects. We develop a general CMT-based approach useful for studying res-

onant scattering and absorption of waves in any linear wave system with well-defined resonances. In particular, we apply this approach to explore the resonant scattering and absorption of electromagnetic plane waves from arbitrary-sized spherically symmetrical resonant objects as well as from point-like resonators of arbitrary symmetry. We also illustrate how the well-known analytical descriptions of resonance fluorescence and Breit-Wigner neutron scattering can also be reproduced using this simple and intuitive approach. The proposed and derived analytical CMT results for the resonant scattering and absorption cross sections of light provide a more elaborate understanding of how the resonant cross sections are affected by the resonance parameters, and are also substantiated by exact numerical Mie calculations [7, 8] as well as by previously explored limiting cases [8, 9].

The second resonance phenomenon that we study concerns an (Electromagnetically Induced Transparency) EIT-like scheme for achieving a more efficient and weakly radiative wireless energy transfer between two identical resonant objects. The scheme is based on mediating the transfer through an intermediate resonant object having the same resonant frequency as that of the identical objects between which energy is transferred. In Chapter 3, we use CMT to analyze the problem and illustrate how it mirrors the EIT process [10] in which a complete adiabatic population transfer takes place between two quantum states; the EIT-like energy transfer scheme essentially makes use of the adiabatic evolution of an instantaneous (so called "dark") eigenstate of the coupled 3-object system, which is achieved by introducing a slow meticulously chosen time variation of the coupling rates. We illustrate this scheme in the special case when the resonant objects are inductively-coupled resonant loops. We also explore how the performance (efficiency and radiative losses) of this wireless energy transfer depends on the various relevant parameters of the system.

Third, we develop a CMT analytical model for the behavior of a polarization source embedded in a general photonic structure. The well-known Purcell effect [11] describes the emission from an oscillating point dipole at a fixed position in a structure. In Chapter 4, we generalize the Purcell effect to the case when the polarization source has arbitrary spatio-temporal dependence and when the photonic structure

itself involves any sort of nonlinearities, gain or loss. Based on this model, we investigate the criteria needed to achieve an enhancement in nonlinear effects in general, and then infer a special design for producing an efficient source of terahertz radiation by optical rectification in a nonlinear photonic crystal structure. We validate our analytical expression for the electric field induced by the polarization source against exact numerical FDTD results, and subsequently propose our analytical approach as a potential substitute for the more numerically intensive FDTD method, especially in problems involving frequencies that range over many orders of magnitude.

The fourth (light-guiding) phenomenon that we investigate concerns broadband super-collimation in photonic crystals. While the supercollimation phenomenon was originally described by Kosaka [12], and subsequently by several other groups [13, 14, 15, 16, 17, 18], the nondiffractive propagation in these studies is restricted to a very narrow frequency range, and its observation is therefore very much sensitive to variations in the frequency of the propagating monochromatic beam. In Chapter 5, we exploite relevant features such as the flatness of "tight-binding"-like bands in waveguide arrays and the discrete translational symmetry in 2D PhCs in order to design a hybrid PhC structure that supports supercollimation over a broad frequency range. We optimize this hybrid structure so as to maximize the frequency range over which supercollimation is sustained. We then illustrate the advantages of the supercollimation mechanism in this proposed hybrid structure compared to that in [16] and also in the waveguide array structure.

Finally, in Chapter 6, we describe a novel class of material systems that strongly discriminate light based on the angle of incidence, over a broad frequency range and irrespective of the polarization. This class of materials is very promising for solar energy applications as it can significantly boost the efficiency of solar-energy conversion [19, 20, 21, 22] by transmitting sunlight incident at a well-defined angle and reflecting outward thermal emission losses (in all other angles) back to the device. We use the transfer matrix method to explore how one could achieve this angular discrimination by using a properly designed 1D PhC with anisotropic layer materials.

Chapter 2

Coupled mode theory for general free-space resonant scattering of waves *

2.1 Introduction

Coupled mode theory (CMT)[4] has been tremendously successful in modeling a wide variety of systems that can entail any number of resonant objects weakly coupled to each other and/or to any number of incoming and outgoing ports. As long as the couplings are weak, and the resonances are well defined, CMT provides an extraordinarily simple and intuitive, yet very accurate analytical framework for modeling resonant behavior of complex systems whose more exact models can often be quite involved. Some examples of systems where CMT is being widely and successfully explored include: optical waveguides and cavities, electronic resonant circuits, and coupled mechanical resonances. In this chapter, it will be shown for the first time that the resonant scattering of freely propagating waves from resonant objects of 2D cylindrical or 3D spherical symmetry, can also be very accurately modeled using very simple CMT analytical expressions; the resonant objects can themselves entail more

*Rafif E. Hamam, Aristeidis Karalis, J. D. Joannopoulos, and Marin Soljačić, Phys. Rev. A **75**, 053801 (2007).

than one weakly coupled resonance. This technique can also often be used to analyze scattering from point-like objects (i.e. objects much smaller than the incident wavelength), even when their substructure does not strictly obey 2D cylindrical or 3D spherical symmetry. /the proposed approach can be applied to almost any free-space wave system; we illustrate it by modeling three well known resonant scattering systems: scattering of light from spherically symmetric resonant objects, scattering of light from atoms (resonance fluorescence), and for quantum mechanical scattering of neutrons off of nuclei.

2.2 Outline of CMT approach

Briefly, the general outline of our approach is as follows. First, one exploits the spherical (cylindrical) symmetry of the problem by placing the resonant scatterer at the origin, and decomposing the incoming wave into a discrete set of spherical (cylindrical) modes. Only a subset of these free-space modes will have the same angular symmetry as the dominant radiating modes of the scatterer, thus being able to couple with them. Second, we identify those free-space spherical (cylindrical) modes, which are capable of coupling to the scatterer, as the "ports" for the CMT framework: in practice, there will typically be only very few such modes. Next, the CMT coupling strength between the ports and the radiating modes of the scatterer is evaluated using the knowledge of the lifetimes of the resonances. Finally, the standard CMT framework is used to calculate powers that are dissipated, and/or scattered between the ports, from which various dissipation and/or scattering cross sections of interest can be trivially evaluated.

2.3 Light scattering from spherically symmetrical resonant objects

As a first illustrative example, we use the CMT formalism to analyze the specific case of an electromagnetic plane wave in air of wavelength $\lambda = \frac{2\pi c}{\omega}$ and intensity

I_0 incident on a spherically symmetric weakly absorbing resonant object of outermost radius b. The nature of the resonances in this system are long-lived whispering gallery electromagnetic modes of the scatterer. Theoretical attempts [7, 8] to understand quantitatively the scattering and absorption of light by small particles started almost a century ago with the Rayleigh approximation and the Mie theory. Rayleigh treatment is limited to non-resonant scattering; Mie solution to the problem is exact and applies to spheres of arbitrary size, but it is mainly a numerical solution that cannot be accomplished without resorting to a robust code. An empirical formula for the resonant light scattering from metal nanoparticles has been presented [23, 24] based on Mie calculations. In contrast, we present here an analytical CMT treatment of the resonant light scattering from any spherically symmetric resonant object.

First, the scatterer is placed at the origin, and is described by a dielectric permittivity function $\varepsilon(r)$ and a magnetic permeability $\mu(r)$, both spherically symmetric. The resonant modes of the scatterer: $\vec{M}_{o,n\ell m}$, $\vec{M}_{e,n\ell m}$, $\vec{N}_{o,n\ell m}$ and $\vec{N}_{e,n\ell m}$, are generated from the solutions $\phi_{o,n\ell m} = R_\ell\left(k_n r\right) P_\ell^m\left(\cos\theta\right)\sin\left(m\varphi\right)$ and $\phi_{e,n\ell m} = R_\ell\left(k_n r\right) P_\ell^m\left(\cos\theta\right)\cos\left(m\varphi\right)$ of the scalar wave equation in spherical coordinates, as follows: $\vec{M}_{n\ell m} = \vec{\nabla}\times\left(\vec{r}\phi_{n\ell m}\right)$ and $\vec{N}_{n\ell m} = \frac{\vec{\nabla}\times\vec{M}_{n\ell m}}{k_n}$, $P_\ell^m\left(\cos\theta\right)$ being the associated Legendre function of the first kind, and k_n being the wavevector of the resonant mode. In the limit $r >> b$, the radial part $R_\ell(k_n r)$ of the generating function $\phi_{n\ell m}$, behaves as the Hankel function of the first kind $h_\ell^{(1)}\left(k_n r\right)$. Next, we expand the incident plane wave in terms of the multipoles of radiation: [7] $\vec{E}_{inc} = \vec{E}_0 e^{i(kz-\omega t)} = E_0 e^{-i\omega t}\sum_{\ell'=1}^{\infty} i^{\ell'}\frac{2\ell'+1}{\ell'(\ell'+1)}\left[\vec{M}'_{o,\ell'1} - i\vec{N}'_{e,\ell'1}\right]$, where $\vec{M}'_{o,\ell'1}$ and $\vec{N}'_{e,\ell'1}$ are vector spherical harmonics obtained from the generating function $\phi'_{\substack{o\\e},\ell'1} = j_{\ell'}\left(kr\right) P_{\ell'}^1\left(\cos\theta\right)\left\{\begin{smallmatrix}\sin\varphi\\ \cos\varphi\end{smallmatrix}\right\}$. Note that the major difference between the generating function ϕ of the resonant modes, and the generating function ϕ' of the multipoles lies in that the radial part of the latter is the spherical Bessel function $j_{\ell'}\left(kr\right)$, whereas the radial part of the former is some function $R_\ell\left(k_n r\right)$ that depends on the specific composition of the scatterer, and behaves as $h_\ell^{(1)}\left(k_n r\right)$ far from the scatterer's outermost radius b. The intensity I_0 of the incident plane wave is related to its electric field amplitude by $I_0 = \frac{c\varepsilon_o}{2}\left|E_0\right|^2$ where ε_o is the permittivity of free space. The power $P^{(\ell')}$ incident onto the scatterer,

and carried by the ℓ' component of the plane wave, is obtained by integrating the Poynting vector corresponding to the incident part of that component ($\propto h_{\ell'}^{(2)}(kr)$) over any closed surface enclosing the spherically symmetric resonant object; it is easiest to evaluate the surface integral over a very large sphere centered at the origin. The result is:

$$P^{(\ell')} = \oint \vec{S} \cdot d\vec{a} = \frac{1}{4}\frac{\lambda^2}{2\pi} I_0(2\ell' + 1) \tag{2.1}$$

If the incident wave has angular frequency $\omega = ck$ which is close to the resonance frequency ω_{res} of the scatterer in the TE mode $\overrightarrow{M}_{o,n\ell 1}$, then this wave will excite the mode $\overrightarrow{M}_{o,n\ell 1}$ with an amplitude proportional to α_ℓ, say. The scattered power P_{scat} is precisely the leaky power of this mode; it can be obtained by integrating the Poynting vector of this mode over any large spherical surface enclosing the scatterer. This results in $P_{scat} \propto |\alpha_\ell|^2$. Only the component $\propto \overrightarrow{M'}_{o,\ell 1}$ in the plane wave, with $\ell' = \ell$, couples to the scatterer. Thus, we identify this mode with the $s_{+\ell}$ port of our CMT diagram shown in Fig. 2-1, and we associate the power $|s_{+\ell}|^2$ incident through this port, with $P^{(\ell)}$: $|s_{+\ell}|^2 \equiv P^{(\ell)}$.

Let a represent the scatterer's resonant mode amplitude, normalized such that $|a|^2$ is equal to the energy in the resonant object. Let $1/\tau_{rad}$ and $1/\tau_{abs}$ denote the decay rates due to radiation and absorption, respectively. The corresponding quality factors are

$$Q_{rad} = \frac{\omega_{res}\tau_{rad}}{2} = \frac{\omega_{res}|a|^2}{P_{scat}} \tag{2.2}$$

and

$$Q_{abs} = \frac{\omega_{res}\tau_{abs}}{2} = \frac{\omega_{res}|a|^2}{P_{abs}} \tag{2.3}$$

As long as Q_{rad} and Q_{abs} are sufficiently large, the CMT equation [4] satisfying energy conservation and time reversal symmetry is:

$$\frac{da}{dt} = -i\omega_{res}a - \left(\frac{1}{\tau_{rad}} + \frac{1}{\tau_{abs}}\right)a + \sqrt{\frac{2}{\tau_{rad}}}s_{+\ell} \tag{2.4}$$

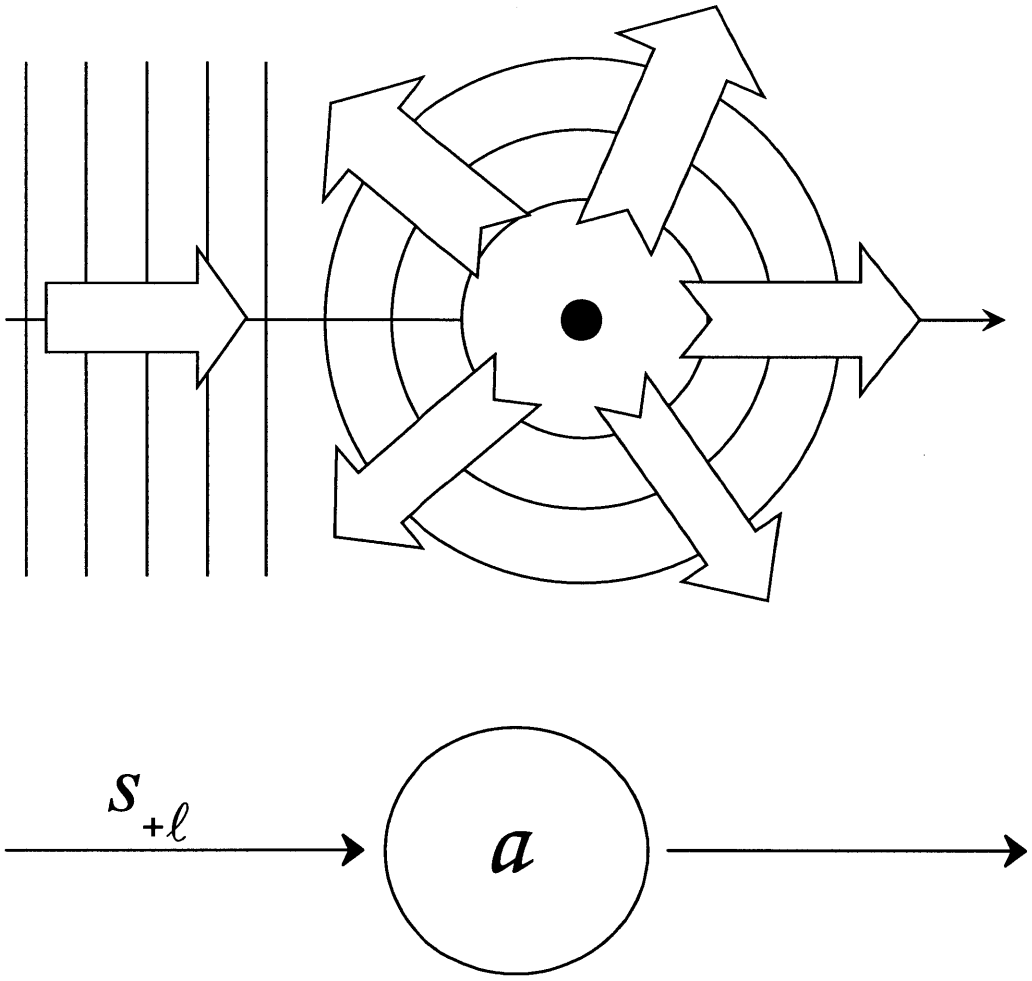

Figure 2-1: Resonant scattering of a plane wave from a spherically symmetric scatterer. The top panel shows a schematic, and the bottom panel shows a coupled mode theory diagram. The resonant mode amplitude is a, while $s_{+\ell}$ is the amplitude of the component of the incident wave that has the right symmetry to couple to the resonant mode of interest.

$$\Rightarrow |a|^2 = \frac{\frac{2}{\tau_{rad}}|s_{+\ell}|^2}{(\omega-\omega_{res})^2+(\frac{1}{\tau_{rad}}+\frac{1}{\tau_{abs}})^2} \tag{2.5}$$

But according to Eq. (2.2) and Eq. (2.3), $P_{scat} = \frac{2}{\tau_{rad}}|a|^2$ and $P_{abs} = \frac{2}{\tau_{abs}}|a|^2$, therefore, using Eq. (2.1), the scattering and dissipation cross sections are given by:

$$\sigma_{scat} \equiv \frac{P_{scat}}{I_0} = \frac{\left(\frac{1}{\tau_{rad}}\right)^2}{(\omega_{res}-\omega)^2+\left(\frac{1}{\tau_{rad}}+\frac{1}{\tau_{abs}}\right)^2}(2\ell+1)\frac{\lambda^2}{2\pi} \tag{2.6}$$

$$\sigma_{abs} \equiv \frac{P_{abs}}{I_0} = \frac{\left(\frac{1}{\tau_{rad}}\right)\left(\frac{1}{\tau_{abs}}\right)}{(\omega_{res}-\omega)^2+\left(\frac{1}{\tau_{rad}}+\frac{1}{\tau_{abs}}\right)^2}(2\ell+1)\frac{\lambda^2}{2\pi} \tag{2.7}$$

On resonance, the scattering and absorption cross sections are, respectively:

$$\sigma_{scat}^{res} = \frac{(1/\tau_{rad})^2}{(1/\tau_{rad}+1/\tau_{abs})^2}(2\ell+1)\frac{\lambda^2}{2\pi} \tag{2.8}$$

$$\sigma_{abs}^{res} = \frac{(1/\tau_{rad})(1/\tau_{abs})}{(1/\tau_{rad}+1/\tau_{abs})^2}(2\ell+1)\frac{\lambda^2}{2\pi} \tag{2.9}$$

The half width at half-maximum (HWHM) of σ_{scat} and σ_{abs} are equal, and are given by:

$$\Gamma_{scat}^{HWHM} = \Gamma_{abs}^{HWHM} = 1/\tau_{rad} = 1/\tau_{abs} \tag{2.10}$$

Note that σ_{abs} does not depend explicitly on the scatterer's outermost radius b; when $b \ll \lambda$, the geometrical cross section πb^2 of the spherical object is much smaller than σ_{abs} ($\sim \lambda^2$). This reproduces the known fact [9] that a small resonant object can absorb much more than the light incident on it: $\sigma_{abs} \gg \pi b^2$.

To test the validity of our analytical formalism, we compare our CMT predictions to numerical results, in the special case of a homogeneous nonpermeable dielectric sphere of radius b. In this case, the resonance frequency ω_{res} is given approximately by [24] $\frac{c}{b}\frac{z_\ell}{n_{real}}$ for $\vec{N}_{e,n\ell 1}$ modes, and by $\frac{c}{b}\frac{z_{\ell-1}}{n_{real}}$ for $\vec{M}_{o,n\ell 1}$ modes, z_ℓ being a zero of the Ricatti-Bessel function $u_\ell(z) \equiv z j_\ell(z)$. The quality factor for absorption is: [25] $Q_{abs} = \frac{Re[\varepsilon]}{\kappa Im[\varepsilon]} \simeq \frac{n_{real}}{2\kappa n_{im}} \gg 1$, assuming $n_{real} \gg n_{im}$, where ε is the dielectric

Table 2.1: Cross sections peak values and HWHM.

	$Q_{rad} = Q_{abs}$ ($n_{im} = 0.00142$)			$Q_{rad} = 2\,Q_{abs}$ ($n_{im} = 0.00284$)		
	MiePlot	CMT	Error	MiePlot	CMT	Error
$\sigma_{scat}^{res}/\pi b^2$	9.88	10.12	2.4%	4.6	4.5	2.2%
$\sigma_{diss}^{res}/\pi b^2$	10.03	10.12	0.9%	8.87	8.99	1.4%
$\Gamma_{scat}^{HWHM} b/c$	0.000153	0.000156	2.0%	0.000243	0.000233	4.0%
$\Gamma_{diss}^{HWHM} b/c$	0.000155	0.0001556	0.4%	0.000231	0.000233	0.9%

function of the sphere, κ is the fraction of modal energy inside it, and $n_{real,im}$ are respectively the sphere's real and imaginary indices of refraction. In the limit of small nonpermeable spheres and large refractive index, the quality factor Q_{rad} for radiation is given analytically in [24]. When $Q_{rad} \gg 1$ and $Q_{abs} \gg 1$, the CMT approximation is valid.

Indeed, for a nonabsorptive sphere ($1/\tau_{abs}$=0), our analytical formula Eq.(9) reproduces the result $\sigma_{scat}^{res} = (2\ell+1)\frac{\lambda^2}{2\pi}$ obtained numerically by van de Hulst [8] for homogeneous dielectric spheres in the case $\omega b/c \ll 1$. Furthermore, we checked our analytical expressions against exact numerical results obtained from MiePlot [26] for the case $n_{real} = 9$ and different ratios of $\frac{Q_{rad}}{Q_{abs}}$. As an illustration, the $n = 2$ TE mode with $\frac{\omega_{res} b}{c} = 0.4971$ has $Q_{rad} = 3193$ and $\kappa = 0.99$. The scattering cross sections are shown in Fig. 2-2 (a) for the two cases $Q_{rad}/Q_{abs} = 1$ and $Q_{rad}/Q_{abs} = 2$, whereas the dissipation cross sections are shown in Fig. 2-2 (b). In addition, a comparison between the analytical and numerical values of σ_{scat}^{res}, σ_{abs}^{res}, Γ_{scat}^{HWHM}, and Γ_{abs}^{HWHM} is presented in Table 2.1, together with the relative errors, which are indeed very small, thus justifying the validity of the CMT approach. Lastly, we also verified our analytical expressions for homogeneous dielectric spheres with radius b both equal to and larger than λ, and obtained good agreement. However, in these cases, the non-resonant background contribution ($\sim \pi b^2$) to the cross section dominates over the resonant part ($\sim \lambda^2/2\pi$); thus, the resonant phenomenon, although well-modeled, is not very pronounced.

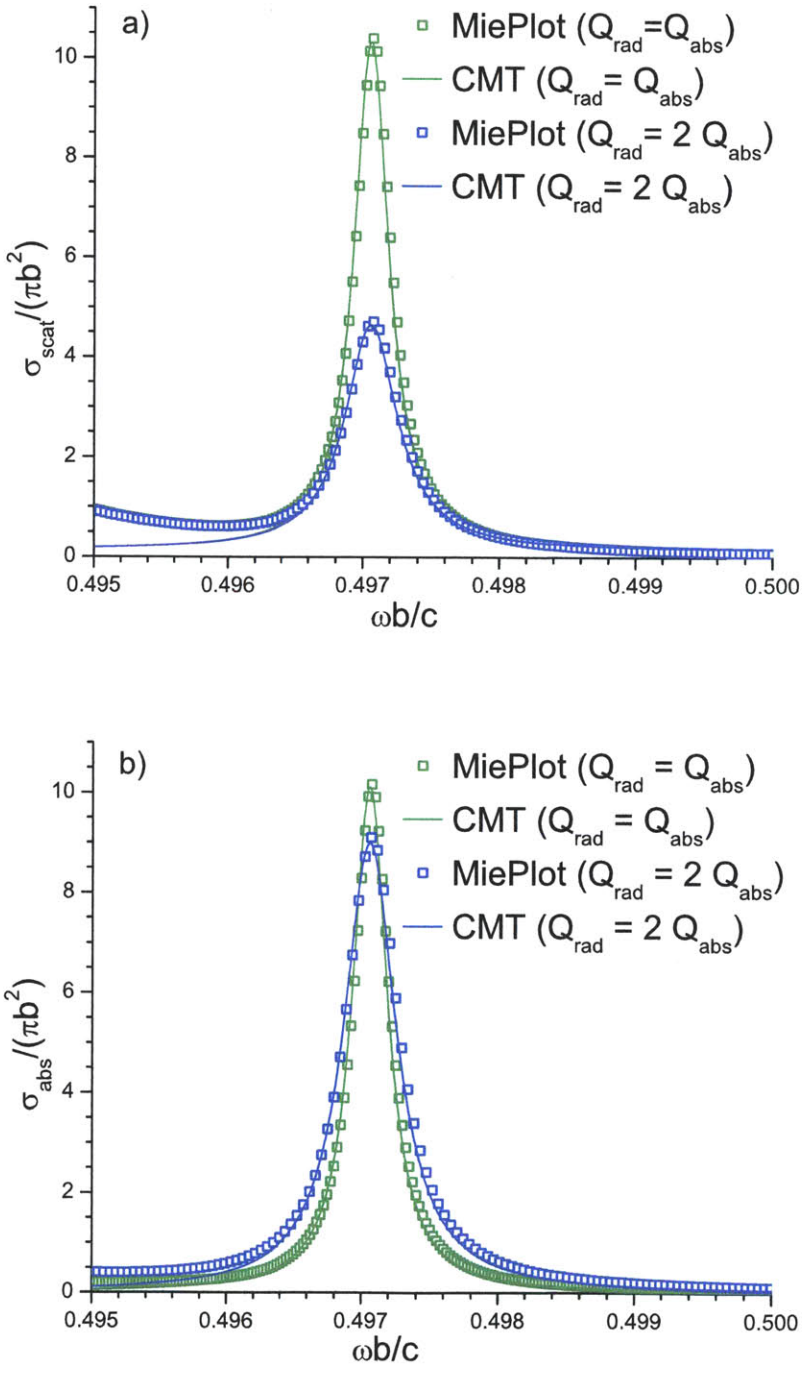

Figure 2-2: Comparison between MiePlot results and coupled mode theory predictions for a homogeneous nonpermeable dielectric sphere of radius b, in the cases $Q_{rad} = Q_{abs}$ and $Q_{rad} = 2\ Q_{abs}$.(a) Scattering cross section. (b) Absorption cross section.

2.4 Resonant light scattering from point-like objects of arbitrary symmetry

In the above treatment of scattering from a spherically symmetric resonant object, the angular symmetry of the scatterer's resonant modes was exactly the same as that of the electric and magnetic multipoles of radiation, irrespective of scatterer's size or radial composition. Hence, only one multipole component of the incident plane wave, was scattered at resonance. Now, if we consider an arbitrary resonant scatterer (not necessarily of spherical or cylindrical symmetry), such that its size is much smaller than the wavelength of light illuminating it, then the far field of the resonant mode can be expanded in terms of the electric and magnetic multipoles. However, given the small size of the resonant object, high-order multipoles contribute only a little to the far field, since those modes of large angular momentum are highly delocalized from the small region of space occupied by the object. Hence, the far field of the resonant mode can be well approximated in terms of the lowest few multipoles of radiation. Typically, for small enough objects, only one of these multipoles will be the dominant mode of radiation. Most often, this mode will be electric dipole; if that one turns out to be prohibited, the dominant mode will be magnetic dipole, or electric quadrupole, etc. In this case, our CMT formalism can also be applied, and the resonant scattering cross section derived above is still valid. If the dominant mode of radiation is electric or magnetic dipole, one uses Eq. (2.6) and Eq. (2.7) with $\ell = 1$. If the dominant mode of radiation is electric or magnetic quadrupole, one uses Eq. (2.6) and Eq. (2.7) with $\ell = 2$. Examples of such objects include: photonic micro-cavities, metallic nanoparticles, resonant radio antennas (whose size is much smaller than the wavelength of the radio wave they couple to), atoms, etc.

2.5 Light scattering from atoms

As an example of point-like systems, we now consider the resonant scattering of radiation from atomic electrons. In this case, the scattering cross section can be found

[27] phenomenologically from a simple classical model: the binding of an electron to its atom is represented by a spherically symmetric linear restoring force $-m_{electron}\omega_{res}^2\vec{r}$, where $\vec{r}$ is the displacement of the electron from its equilibrium position, and ω_{res} is the resonant frequency of electronic oscillation. For an incident plane wave $\vec{E}_{inc}$ of frequency ω, the electric force on the electron is $-e\vec{E}_{inc}$. Taking into account the small reactive effects of radiation, one can write an equation of motion for the electron (in the electric dipole approximation), and solve it for $\vec{r}$. A resistive term $m_{electron}\frac{2}{\tau_{abs}}\dot{\vec{r}}$ is added to the equation of motion in order to account for dissipation. The scattering cross section can then be deduced from the expression of the radiated electric field of the oscillating dipole. Following this approach, one obtains: [27]

$$\sigma_{scat} = \frac{3\lambda^2}{2\pi}\frac{\omega^4}{\omega_{res}^2}\frac{\left(2/\tau_{rad}\right)^2}{\left(\omega_{res}^2-\omega^2\right)^2+\omega^2\left(2/\tau_{rad}+2/\tau_{abs}\right)^2} \tag{2.11}$$

where $\frac{1}{\tau_{rad}} \equiv \frac{\omega_{res}^2\tau}{2}$ and $\tau \equiv \frac{2}{3}\frac{e^2}{m_{electron}c^3}$. For ω close to ω_{res}, this can be expanded to:

$$\sigma_{scat} \approx \frac{3\lambda^2}{2\pi}\frac{\left(1/\tau_{rad}\right)^2}{\left(\omega_{res}-\omega\right)^2+\left(1/\tau_{rad}+1/\tau_{abs}\right)^2} \tag{2.12}$$

In a similar fashion, one obtains:

$$\sigma_{abs} \approx \frac{3\lambda^2}{2\pi}\frac{\left(1/\tau_{rad}\right)\left(1/\tau_{abs}\right)}{\left(\omega_{res}-\omega\right)^2+\left(1/\tau_{rad}+1/\tau_{abs}\right)^2} \tag{2.13}$$

Exactly the same expressions for σ_{scat} and σ_{abs} can alternatively be obtained using our CMT approach, as a special case of Eq. (2.6) and Eq. (2.7) respectively, corresponding to $\ell = 1$. The CMT treatment is still valid in this case, because the scatterer's resonant modes have the same symmetry as before, and hence the coupling of the incident plane wave to them is the same. The reason that the approach outlined above, predicts only the $\ell = 1$ case of the more general CMT result, is that it represents the system by an oscillating electric dipole, and hence describes only the coupling of the electric dipole mode $\vec{N}_{e,n11}$ for which $\ell = 1$.

So far, classical models of atomic transitions succeeded in explaining only the elec-

tric dipole transition: magnetic dipole, electric quadrupole, and higher order atomic transitions, required a quantum mechanical analysis. In contrast, our phenomenological CMT formalism can be used to excellently reproduce quantum mechanical predictions for atomic transitions: electric or magnetic, dipole, quadrupole or any of the higher order ones.

2.6 Breit-Wigner scattering of neutrons from nuclei

Besides their applicability to resonance fluorescence, Eq. (2.6) and Eq. (2.7) are also reminiscent of the Breit-Wigner (BW) formula for resonant scattering of neutrons from nuclei in compound nucleus reactions. This is not unexpected since "CMT-like" equations emerge throughout the derivation of the Breit-Wigner formula [28, 29]. Using the CMT formalism, we present here an alternative derivation of BW as an example of quantum mechanical resonant scattering. The nucleus (scatterer) is placed at the origin, and creates a localized central potential U(r). The quasi-stationary states $\phi_{n\ell m}(= R_\ell(k_n r)P_\ell^m(cos\theta)e^{im\varphi})$ for a neutron in this potential have energies $E_{n\ell}$, with corresponding lifetimes $\tau_{n\ell}$. In the region outside the localized nucleus' potential, the radial part $R_\ell(k_n r)$ of the quasi-stationary states is given by the Hankel function of the first kind: $R_\ell(k_n r) \propto h_\ell^{(1)}(k_n r)$, since the potential is zero there. The incident neutron, of mass m_n, is assumed to be moving in the z direction, and is represented by a plane wavefunction: $\psi_{inc} = Ae^{i(kz-\omega t)}$, where A is determined by normalization. The neutron's wavefunction ψ_{inc} can be expanded in a basis consisting of the vacuum (U(r)=0) eigenstates in spherical coordinates, as follows: $\psi_{inc} = A\sum_{\ell'=0}^{\infty} i^{\ell'}\,(2\ell'+1)\,j_{\ell'}\,(kr)\,P_{\ell'}\,(\cos\theta)$. The probability current density associated with the ℓ' component, $\psi_{inc}^{(\ell')}$, of ψ_{inc} is: $\vec{J}^{(\ell')}\,(\vec{r},t) = \frac{\hbar}{m_n}\mathrm{Im}\left[\left(\psi_{inc}^{(\ell')}\right)^* \vec{\nabla}\psi_{inc}^{(\ell')}\right]$, and the corresponding probability per unit time is: $p^{(\ell')} = \oint \vec{J}^{(\ell')}\cdot d\vec{a} = (2\ell'+1)\,\frac{\pi\hbar}{m_n V}\frac{1}{k}$ where $V = 1/|A|^2$ is the volume of the system. If the incident neutron has energy $E(=\frac{\hbar^2k^2}{2m_n})$ very close to the energy $E_{n\ell}$ of the quasi-stationary state $\phi_{n\ell m}$ of a neutron

in the localized nuclear potential, then the only component of the incident neutron's wavefunction ψ_{inc} that couples to the nucleus is $\psi_{inc}^{(\ell)}$; this is because $\langle \phi_{n\ell m} \mid \psi_{inc} \rangle$ is nonzero only for $\ell = \ell'$ and $m = 0$. Therefore, the probability per unit time that the neutron interacts with the nucleus is $p^{(\ell)}$, and we identify $p^{(\ell)}$ with $|s_{+\ell}|^2$ in our CMT formalism: $p^{(\ell)} \equiv |s_{+\ell}|^2$. Once the neutron couples resonantly with the nucleus, its wavefunction is given by the quasi-stationary state $\phi_{n\ell 0}$, with amplitude $a_{n\ell}$ satisfying the following CMT equation:

$$\frac{da_{n\ell}}{dt} = -i\frac{E_{n\ell}}{\hbar}a_{n\ell} - \frac{1}{\tau}a_{n\ell} + \sqrt{\frac{2}{\tau_{n\ell}}}s_{+\ell} \tag{2.14}$$

where $\frac{1}{\tau} \equiv \frac{\Gamma}{\hbar} = \frac{\sum_j \Gamma_j}{\hbar}$ is the total rate of decay in all possible channels, and $\frac{1}{\tau_{n\ell}} \equiv \frac{\Gamma_i}{\hbar}$ is the decay rate in the same initial channel. In analogy with Eq. (2.5), we have: $|a_{n\ell}|^2 = \frac{2\hbar\Gamma_i}{(E-E_{n\ell})^2+\Gamma^2}|s_{+\ell}|^2$. The reaction rate at which the neutron's initial state $\psi_{inc}^{(\ell)}$ changes to $\psi_{inc}^{(f)}$ is: $\frac{2}{\tau_f}|a_{n\ell}|^2 = \frac{4\Gamma_i\Gamma_f}{(E-E_{n\ell})^2+\Gamma^2}|s_{+\ell}|^2$. This is also equal to the product of the flux $\frac{1}{V}\frac{\hbar k}{m_n}$ of incident neutrons and the cross section $\sigma(\psi_{inc}^{(\ell)} \rightarrow channel f)$ for decay into channel f. Therefore:

$$\sigma\left(i \rightarrow f\right) = \frac{4\pi}{k^2}\left(2\ell+1\right)\frac{\Gamma_i\Gamma_f}{\left(E-E_{n\ell}\right)^2+\Gamma^2} \tag{2.15}$$

This result reproduces the well-known Breit-Wigner formula [30] obtained as a solution to a resonant scattering problem in quantum mechanics.

2.7 Conclusion

In conclusion, we have shown in this chapter how to apply CMT to model the resonant scattering/absorption of free-space waves from resonant objects, and we illustrated this approach by applying it to three particular physical systems. In general, this approach could be useful for almost any free-space wave system, as long as the scatterer's resonances are well defined, and the scatterer is either sufficiently smaller than the wavelength or else has 2D cylindrical or 3D spherical symmetry. In the next chapter,

we will use CMT again to study the mechanism of wireless energy transfer through resonant near-field coupling between two high-Q resonant objects having the same resonant frequency. We will develop and analyze an adiabatic energy transfer scheme that improves on the performance of the previously studied resonant wireless energy transfer schemes, both in terms of increasing the transfer efficiency and reducing the amount of undesirable radiation.

Chapter 3

Efficient weakly-radiative wireless energy transfer: An EIT-like approach*

3.1 Introduction

The decade has witnessed a considerable interest in energy issues, such as safe generation of renewable energy, energy storage and management, etc... In particular, there is a substantial recent interest [31, 32, 33, 34, 35] in enabling efficient and safe wireless energy transfer, motivated by the increased involvement of autonomous electronic devices (e.g. laptops, cell phones, household robots) in almost all aspects of our everyday lives, and the need to charge those devices repeatedly. In this respect, wireless nonradiative energy transfer schemes have been recently proposed [36, 37] based on strong coupling between electromagnetic resonances. In this chapter, we explore a somewhat different scheme of efficient energy transfer between resonant objects coupled in some general way. Instead of transferring energy directly between the two resonant objects, an intermediate resonant object will be used to mediate the transfer. The intermediate object is chosen such as to couple very strongly to

*Rafif E. Hamam, Aristeidis Karalis, J. D. Joannopoulos, and Marin Soljačić, Annals of Physics **324**, 1783, (2009).

each of the objects involved in the energy transfer (i.e. much more strongly than the other two objects couple to each other). In practice, enabling such strong coupling will usually come with a price; in typical situations, the mediating object will often be substantially radiative. Yet, surprisingly enough, the proposed "indirect" energy transfer scheme will be shown to be efficient and weakly-radiative by merely introducing a meticulously chosen time variation of the coupling rates. The inspiration as to why the particular time variation had to work so well comes from a quantum interference phenomenon, known in the atomic physics community as Electromagnetically Induced Transparency (EIT) [38]. In EIT, 3 atomic states participate. Two of them (which are non-lossy) are coupled to one that has substantial losses. However, by meticulously controlling the mutual couplings between the states, one can establish a coupled system which is overall non-lossy. This manifests itself in that a medium that is originally highly opaque to some laser pulse (called "probe" laser), can be made transparent by sending through it another laser pulse (called "Stokes" laser), provided that the temporal overlap between the two pulses is properly chosen. A closely related phenomenon known as Stimulated Raman Adiabatic Passage (STIRAP) [10, 39, 40] takes place in a similar system; namely, the probe and Stokes laser can be used to achieve a complete coherent population transfer between two molecular states of the medium. Hence, we refer to the currently proposed scheme as the "EIT-like" energy transfer scheme.

To set the stage for our proposed indirect energy transfer scheme, we will first consider (in section 3.2) one concrete example of wireless energy transfer between two resonant capacitively-loaded conducting-wire loops [36], and show how the indirect EIT-like scheme can be made more efficient and less-radiative in this particular system than the direct scheme, by including proper time variations in the coupling rates. In section 3.3, we analyze the underlying physical mechanism which turns out to be applicable not just to "wireless" energy transfer, but more generally to any sort of energy transfer between resonant objects. The analysis will be based on temporal coupled mode theory (CMT) [4], which is a valid description for well-defined resonances with large quality factors. In section 3.4, we study the general case of EIT-like

energy transfer, how the transferred and lost energies vary with the rates of coupling and loss, both with and without time variation of the coupling rates; we also investigate the range of relevant parameters in which the radiated energy is substantially reduced by using the EIT-like scheme.

3.2 An illustrative example of an EIT-like system

We start with a concrete case of wireless energy transfer between two identical resonant conducting loops, labelled by L_1 and L_3. The loops are capacitively-loaded and couple inductively via their mutual inductance. Let r_A denote the loops' radii, N_A their numbers of turns, and b_A the radii of the wires making the loops. We also denote by D_{13} the center-to-center separation between the loops. Resonant objects of this type have two main loss mechanisms: ohmic absorption, and far-field radiation. Using the same theoretical method from [36], we find that for $r_A = 7$cm, $b_A = 6$mm, and $N_A = 15$ turns, the quality factors for absorption and radiation are respectively, $Q_{abs}^{(A)} \equiv 2\pi f/\Gamma_{abs}^{(A)} = 3.19 \times 10^4$ and $Q_{rad}^{(A)} \equiv 2\pi f/\Gamma_{rad}^{(A)} = 2.6 \times 10^5$ at a resonant frequency $f = 1.8 \times 10^7$Hz (remember that L_1 and L_3 are identical and have the same properties). $\Gamma_{abs}^{(A)}$, $\Gamma_{rad}^{(A)}$ are respectively the rates of absorptive and radiative loss of L_1 and L_3, and the rate of coupling between L_1 and L_3 is denoted by κ_{13}. When the loops are in fixed distinct parallel planes separated by $D_{13} = 1.4$m and have their centers on an axis (C) perpendicular to their planes, as shown in Fig. 3-1 (a) (Left), the quality factor for inductive coupling is $Q_\kappa \equiv 2\pi f/\kappa_{13} = 1.3 \times 10^4$, independent of time. This configuration of parallel loops corresponds to the largest possible coupling rate κ_{13} at the particular separation D_{13}. We denote the amplitude of the electric field of the resonant mode of L_1 by a_1, and that of L_3 by a_3. As long as all the quality factors involved are large enough, the time evolution of the mode amplitudes a_1 and a_3 can be modelled according to the following temporal CMT equations [4]:

$$\frac{da_1}{dt} = -(i\omega + \Gamma_A)\, a_1 + i\kappa_{13} a_3 \tag{3.1}$$

$$\frac{da_3}{dt} = -(i\omega + \Gamma_A)\, a_3 + i\kappa_{13} a_1 \tag{3.2}$$

where $\omega = 2\pi f$ is the angular resonance frequency, and $\Gamma_A = \Gamma_{rad}^{(A)} + \Gamma_{abs}^{(A)}$. The mode amplitudes $a_1(t)$ and $a_3(t)$ are normalized such that $|a_1(t)|^2$ and $|a_3(t)|^2$ represent, respectively, the energies in L_1 and L_3 at time t: $E_1(t) \equiv |a_1(t)|^2$ and $E_3(t) \equiv |a_3(t)|^2$. Starting with 100% of the total energy being initially in L_1 (i.e. $|a_3(t=0)|^2 = 0$), we find that the energy transferred to L_3 is maximum at time $t_a = 4774.6(1/f)$, and constitutes 29% of the initial total energy, as shown in Fig. 3-1 (a) (Right). The energies radiated $E_{rad}(t_a)$ and absorbed $E_{abs}(t_a)$ up to time t_a constitute respectively 7.2% and 58.1% of the initial total energy, with 5.8% of the energy remaining in L_1. The CMT expressions used for $E_{rad}(t_a)$ and $E_{abs}(t_a)$ are given by:

$$E_{rad}(t_a) = \int_0^{t_a} \left(2\,\Gamma_{rad}^{(A)}|a_1(t)|^2 + 2\,\Gamma_{rad}^{(A)}|a_3(t)|^2\right)dt \tag{3.3}$$

$$E_{abs}(t_a) = \int_0^{t_a} \left(2\,\Gamma_{abs}^{(A)}|a_1(t)|^2 + 2\,\Gamma_{abs}^{(A)}|a_3(t)|^2\right)dt \tag{3.4}$$

In order to improve the efficiency of the energy transfer from the current $\simeq 30\%$, we now consider different ways to boost the energy transferred from L_1 to L_3 while keeping the distance D_{13} separating them fixed. Since the relative orientations of the two loops are already chosen to yield the maximum κ_{13}, we no longer have much flexibility in improving the efficiency of transfer between these given resonant objects at the same separation D_{13}. So, we introduce an intermediate resonant object that couples strongly to both L_1 and L_3, while having the same resonant frequency as both of them. For the sake of illustration in the particular concrete system under consideration, we also take that mediator to be a capacitively-loaded conducting-wire loop, and we label it by L_2. We place L_2 at equal distance ($D_{12} = D_{23} = D_{13}/2 = 0.7$m) from L_1 and L_3 such that its axis also lies on the same axis (C), and we orient it such that its plane is parallel to the planes of L_1 and L_3. In order for L_2 to couple strongly to L_1 and L_3, its size needs to be substantially larger than the size of L_1 and L_3. However this increase in the size of L_2 has a considerable drawback in the sense that it is also accompanied by a significant increase in the undesired radiated

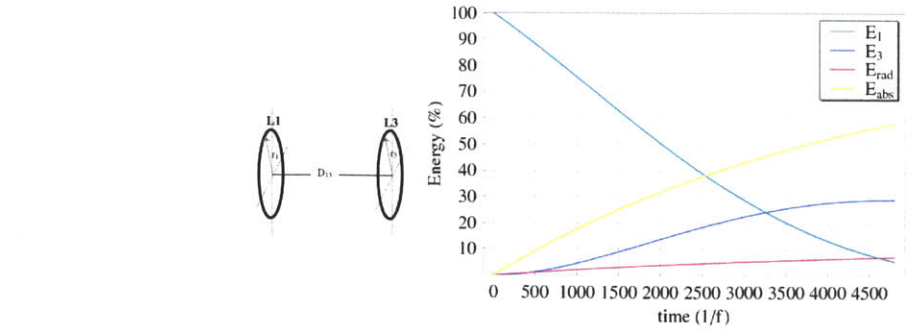

(a)

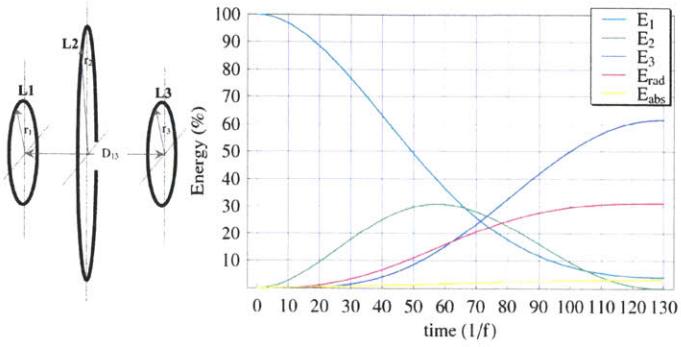

(b)

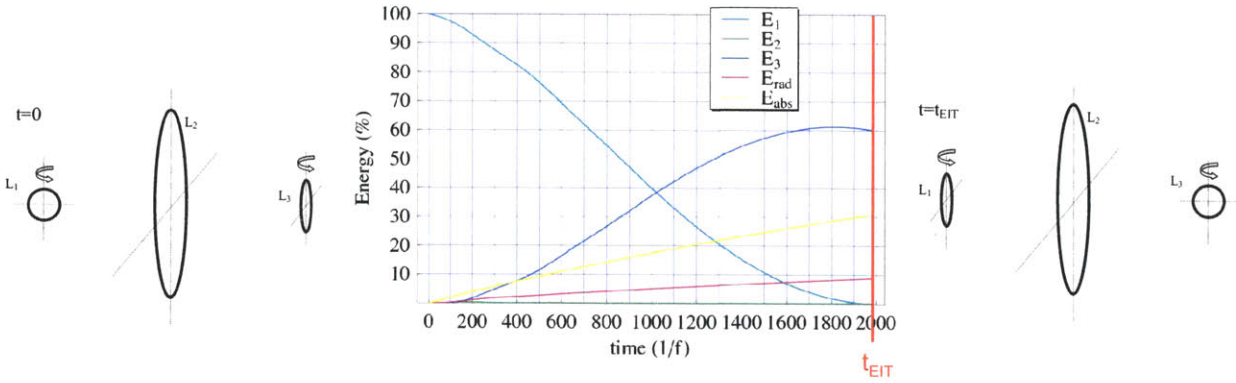

(c)

Figure 3-1: Wireless energy transfer in an exemplary system: (a) (Left) Schematic of loops configuration in 2-object direct transfer. (Right) Time evolution of energies in the 2-object direct energy transfer case. (b) (Left) Schematic of 3-loops configuration in the constant-κ case. (Right) Dynamics of energy transfer for the configuration in (b) (Left). Note that the total energy transferred E_3 is two times larger than in (a) (Right), but at the price of the total energy radiated being four times larger. (c) (Left) Loop configuration at t=0 in the EIT-like scheme. (Center) Dynamics of energy transfer with EIT-like rotating loops. (Right) Loop configuration at $t = t_{EIT}$. Note that E_3 is comparable to (b) (Right), but the radiated energy is now much smaller: In fact, it is comparable to (a) (Right).

energy. This feature is quite generic for the resonant systems of this type: stronger coupling can often be enabled by increasing the objects' size, but it implies stronger radiation from the object in question. Large radiation is often undesirable because it could lead to far-field interference with other RF systems, and in some systems also because of safety concerns. For $r_B = 70\text{cm}$, $b_B = 1.5\text{cm}$, and $N_B = 1$ turn, we get $Q_{abs}^{(B)} \equiv 2\pi f/\Gamma_{abs}^{(B)} = 7706$, $Q_{rad}^{(B)} \equiv 2\pi f/\Gamma_{rad}^{(B)} = 400$, and $Q_{\kappa_{12}} \equiv 2\pi f/\kappa_{12} = Q_{\kappa_{23}} = 180$ at $f = 1.8 \times 10^7\text{Hz}$. A schematic diagram of the 3-loops configuration is depicted in Fig. 3-1 (b) (Left). If we denote the amplitude of the E-field of the resonance mode in L_2 by a_2, then the CMT equations can be written as:

$$\frac{da_1}{dt} = -(i\omega + \Gamma_A)a_1 + i\kappa_{12}a_2 \tag{3.5}$$

$$\frac{da_2}{dt} = -(i\omega + \Gamma_B)a_2 + i\kappa_{12}a_1 + i\kappa_{23}a_3 \tag{3.6}$$

$$\frac{da_3}{dt} = -(i\omega + \Gamma_A)a_3 + i\kappa_{23}a_2 \tag{3.7}$$

Note that since the coupling rates κ_{12} and κ_{23} are $\simeq 70$ times larger than κ_{13}, we can ignore the direct coupling between L_1 and L_3, and focus only on the indirect energy transfer through the intermediate loop L_2. If initially all the energy is placed in L_1, i.e. if $E_2(t=0) \equiv |a_2(t=0)|^2 = 0$ and $E_3(t=0) \equiv |a_3(t=0)|^2 = 0$, then the optimum in energy transferred to L_3 occurs at a time $t_b = 129.2(1/f)$, and is equal to $E_3(t_b) = 61.50\%$. The energy radiated up to t_b is $E_{rad}(t_b) = 31.1\%$, while the energy absorbed is $E_{abs}(t_b) = 3.3\%$, and 4.1% of the initial energy is left in L_1. Thus while the energy transferred, now indirectly, from L_1 to L_3 has increased by a factor of 2 relative to the 2-loops direct transfer case, the energy radiated has undesirably increased by a significant factor of 4. Also note that the transfer time in the 3-loops case is now $\simeq 35$ times shorter than in the 2-loops direct transfer because of the stronger coupling rate. The dynamics of the energy transfer in the 3-loops case is shown in Fig. 3-1 (b) (Right), where the expressions used for $E_{rad}(t_b)$ and $E_{abs}(t_b)$

are given by:

$$E_{rad}(t_b) = \int_0^{t_b} \left(2\Gamma^A_{rad}|a_1(t)|^2 + 2\Gamma^B_{rad}|a_2(t)|^2 + 2\Gamma^A_{rad}|a_3(t)|^2\right)dt \tag{3.8}$$

$$E_{abs}(t_b) = \int_0^{t_b} \left(2\Gamma^A_{abs}|a_1(t)|^2 + 2\Gamma^B_{abs}|a_2(t)|^2 + 2\Gamma^A_{abs}|a_3(t)|^2\right)dt \tag{3.9}$$

Thus the switch from 2-loops direct transfer to 3-loops indirect transfer had an expected significant improvement in efficiency, but it came with the undesirable effect of increased radiated energy. Let us now consider some modifications to the 3-loops indirect transfer scheme, aiming to reduce the total radiated energy back to its reasonable value in the 2-loops direct transfer case, while maintaining the total energy transfer at a level comparable to Fig. 3-1 (b). As shown in Fig. 3-1 (c) (Left and Right), we will keep the orientation of L_2 fixed, and start initially (t=0) with L_1 perpendicular to L_2 and L_3 parallel to L_2, then uniformly rotate L_1 and L_3, at the same rates, until finally, at $(t = t_{EIT})$, L_1 becomes parallel to L_2 and L_3 perpendicular to it, where we stop the transfer process. This process can be modeled by the following time variation in the coupling rates:

$$\kappa_{12}(t) = \kappa \sin\left(\pi t/2t_{EIT}\right) \tag{3.10}$$

$$\kappa_{23}(t) = \kappa \cos\left(\pi t/2t_{EIT}\right) \tag{3.11}$$

for $0 < t < t_{EIT}$, and $Q_\kappa = 180.1$ as before. By using the same CMT analysis as in Eq. (3.5-7), we find, in Fig. 3-1 (c) (Center), that for $t_{EIT} = 1989.4(1/f)$, an optimum transfer of 61.2% can be achieved at $t_c = 1,798.5(1/f)$, with only 8.2% of the initial energy being radiated, 28.6% absorbed, and 2% left in L_1. This is quite remarkable: by simply rotating the loops during the transfer, the energy radiated has dropped by a factor of 4, while keeping the same 61% level of the energy transferred, although the instantaneous coupling rates are now smaller than κ. This considerable decrease in radiation is on first sight quite counterintuitive, because the intermediate resonator L_2, which mediates all the energy transfer, is highly radiative ($\simeq$ 650 times more

radiative than L_1 and L_3), and there is much more time to radiate, since the whole process lasts 14 times longer than in Fig. 3-1 (b).

A clue to the physical mechanism behind this surprising result can be obtained by observing the differences between the green curves in Fig. 3-1 (b) and Fig. 3-1 (c). Unlike the case of constant coupling rates, depicted in Fig. 3-1 (b), where the amount of energy ultimately transferred to L_3 goes first through the intermediate loop L_2, in the case of time-varying coupling rates, shown in Fig. 3-1 (c), there is almost little or no energy in L_2 at all times during the transfer. In other words, the energy is transferred quite efficiently from L_1 to L_3, mediated by L_2 without ever being in the highly radiative intermediate loop L_2. (Note that direct transfer from L_1 to L_3 is identically zero here since L_1 is always perpendicular to L_3, so all the energy transfer is indeed mediated through L_2). This surprising phenomenon is actually quite similar to the well-known electromagnetically induced transparency [38] (EIT), which enables complete population transfer between two quantum states through a third lossy state, coupled to each of the other two states.

3.3 Physical mechanism behind EIT-like energy transfer scheme

We note that the mechanism explored in the previous section is not restricted to wireless energy transfer between inductively coupled loops, but its scope extends beyond, to the general case of energy transfer between resonant objects (henceforth denoted by R_i) coupled in some general way. So, all the rest of this chapter falls in this general context, and the only constraints for the EIT-like scheme are that the three resonant objects have the same resonance angular frequency, which we denote by ω_o, that all quality factors be large enough for CMT to be valid, and that the initial and final resonant objects have the same loss rate Γ_A. R_1 and R_3 will be assumed to have negligible mutual interactions with each other, while each of them can be strongly coupled to R_2. However, as is often the case in practice of wireless power transfer

[36], R_2's strong coupling with other objects will be assumed to be accompanied with its inferior loss properties compared to R_1 and R_3, usually in terms of substantially larger radiation losses. To analyze the problem in detail, we start by rewriting the CMT Eq. (3.5-7) in matrix form, and then diagonalizing the resulting time evolution operator $\hat{C}(t)$.

$$\frac{d}{dt}\begin{pmatrix} a_1 \\ a_2 \\ a_3 \end{pmatrix} = \begin{pmatrix} -(i\omega_o + \Gamma_A) & i\kappa_{12} & 0 \\ i\kappa_{12} & -(i\omega_o + \Gamma_B) & i\kappa_{23} \\ 0 & i\kappa_{23} & -(i\omega_o + \Gamma_A) \end{pmatrix}\begin{pmatrix} a_1 \\ a_2 \\ a_3 \end{pmatrix} \equiv \hat{C}(t)\begin{pmatrix} a_1 \\ a_2 \\ a_3 \end{pmatrix} \tag{3.12}$$

In the special case where the coupling rates κ_{12} and κ_{23} are constant and equal, Eq. (12) admits a simple analytical solution, presented in the appendix. In the more general case of time dependent and unequal coupling rates $\kappa_{12}(t)$ and $\kappa_{23}(t)$, the CMT operator $\hat{C}(t)$ has an interesting feature which results from the fact that one of its eigenstates, $\vec{V}_1$, with complex eigenvalue $\lambda_1 = -(i\omega_o + \Gamma_A)$, has the form

$$\vec{V}_1 = e^{-i\omega_o t - \Gamma_A t}\begin{pmatrix} \frac{-\kappa_{23}}{\sqrt{(\kappa_{12})^2+(\kappa_{23})^2}} \\ 0 \\ \frac{\kappa_{12}}{\sqrt{(\kappa_{12})^2+(\kappa_{23})^2}} \end{pmatrix} \tag{3.13}$$

This eigenstate $\vec{V}_1$ is the most essential building block of our proposed efficient weakly-radiative energy transfer scheme, because it has no energy at all in the intermediate (lossy) resonator R_2, i. e. $a_2(t) = 0\ \forall\ t$ whenever the 3-object system is in state $\vec{V}_1$. In fact if $\Gamma_A \rightarrow 0$, then the EIT-like energy transfer scheme can be made completely nonradiative, no matter how large is the radiative rate Γ^B_{rad}, as shown in Fig. 3-2. Moreover, if the 3-object system is in state $\vec{V}_1$, then $\kappa_{12} = 0$ corresponds to all the system's energy being in R_1, while $\kappa_{23} = 0$ corresponds to all the system's energy being in R_3. So, the important considerations necessary to achieve efficient weakly radiative energy transfer, consist of preparing the system initially in state $\vec{V}_1$. Thus, if at $t = 0$ all the energy is in R_1, then one should have $\kappa_{12}(t = 0) = 0$ and $\kappa_{23}(t = 0) \neq 0$. In the loops' case where coupling is performed through induction, these values for κ_{12} and

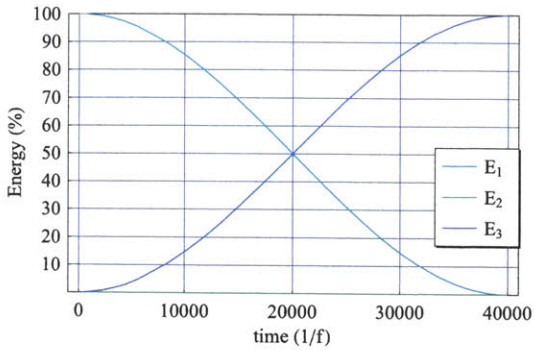

Figure 3-2: Energy transfer with time-varying coupling rates, for $\Gamma_A = 0$, $\kappa/\Gamma_B = 10, \kappa_{12} = \kappa \sin(\pi t/(2t_{EIT}))$, and $\kappa_{23} = \kappa \cos(\pi t/(2t_{EIT}))$.

κ_{23} correspond to exactly the same configuration that we had considered in Fig. 3-1 (c), namely starting with $L_1 \perp L_2$ and $L_3 \parallel L_2$. In order for the total energy of the system to end up in R_3, we should have $\kappa_{12}(t = t_{EIT}) \neq 0$ and $\kappa_{23}(t = t_{EIT}) = 0$. This ensures that the initial and final states of the 3-object system are parallel to $\vec{V}_1$. However, a second important consideration is to keep the 3-object system at all times in $\vec{V}_1(t)$, even as $\kappa_{12}(t)$ and $\kappa_{23}(t)$ are varied in time. This is crucial in order to prevent the system's energy from getting into the intermediate object R_2, which may be highly radiative as in the example of Fig. 3-1, and requires changing $\kappa_{12}(t)$ and $\kappa_{23}(t)$ slowly enough so as to make the entire 3-object system adiabatically follow the time evolution of $\vec{V}_1(t)$. The criterion for adiabatic following can be expressed, in analogy to the population transfer case [10], as

$$\left| \left\langle \vec{V}_{2,3} \left| \frac{d\vec{V}_1}{dt} \right\rangle \right| << |\lambda_{2,3} - \lambda_1| \tag{3.14}$$

where $\vec{V}_2$ and $\vec{V}_3$ are the remaining two eigenstates of $\hat{C}(t)$, with corresponding eigenvalues λ_2 and λ_3. In principle, one would think of making the transfer time t_{EIT} as long as possible to ensure adiabaticity. However there is a limitation on how slow the transfer process can optimally be, imposed by the losses in R_1 and R_3. Such a limitation may not be a strong concern in a typical atomic EIT case, because the initial and final states there can be chosen to be non-lossy ground states. However, in our case, losses in R_1 and R_3 are not avoidable, and can be detrimental to the

energy transfer process whenever the transfer time t_{EIT} is not less than $1/\Gamma_A$. This is because, even if the 3-object system is carefully kept in $\vec{V}_1$ at all times, the total energy of the system will decrease from its initial value as a consequence of losses in R_1 and R_3. Thus the duration of the transfer should be a compromise between these two limits: the desire to keep t_{EIT} long enough to ensure near-adiabaticity, but short enough not to suffer from losses in R_1 and R_3.

We can now also see in the EIT framework why is it that we got a considerable amount of radiated energy when the inductive coupling rates of the loops were kept constant in time, i.e. in constant-κ case, like in Fig. 3-1 (b). The reason is that, when $\kappa_{12} = \kappa_{23}$ =const, the energies in R_1 and R_3 will always be equal to each other if the 3-object system is to stay in $\vec{V}_1$. So one cannot transfer energy from R_1 to R_3 by keeping the system purely in state $\vec{V}_1$; note that even the initial state of the system, in which all the energy is in R_1, is not in $\vec{V}_1$, and has nonzero components along the eigenstates $\vec{V}_2$ and $\vec{V}_3$ which implies a finite energy in R_2, and consequently result in an increased radiation, especially if $\Gamma^B_{rad} \gg \Gamma^A_{rad}$ as in our concrete example.

Although the analysis presented above, in terms of the adiabatic following of the eigenstate $\vec{V}_1$, clarifies why the EIT-like transfer scheme is weakly radiative, this explanation still seems to be puzzling and somewhat paradoxical. The origin of the paradox stems from the fact that, in the EIT-like approach, there is no energy at all in the mediator R_2. That is to say, energy is efficiently transferred through the intermediate resonator R_2 without ever being in it. This apparent contradiction can be resolved by looking at the detailed contributions to the time-rate of change of the energy E_2 in R_2. As we show it in more details in appendix A, the EIT-like approach ensures that the energy leaves R_2 (to R_3) as soon as it reaches R_2 (from R_1).

3.4 Under which conditions is EIT-like approach beneficial?

In the abstract case of energy transfer from R_1 to R_3, where no constraints are imposed on the relative magnitude of κ, Γ^A_{rad}, Γ^B_{rad}, Γ^A_{abs} and Γ^B_{abs}, there is no reason to think that the EIT-like transfer is always better than the constant-κ one, in terms of the transferred and radiated energies. In fact, there could exist some range of the parameters (κ, Γ^A_{rad}, Γ^B_{rad}, Γ^A_{abs}, Γ^B_{abs}), for which the energy radiated in the constant-κ transfer case is less than that radiated in the EIT-like case. For this reason, we investigate both the EIT-like and constant-κ transfer schemes, as we vary all the crucial parameters of the system. The percentage of energies transferred and lost (radiated+absorbed) depends only on the relative values of κ, Γ_A and Γ_B. Here, $\Gamma_A = \Gamma^A_{rad} + \Gamma^A_{abs}$, and $\Gamma_B = \Gamma^B_{rad} + \Gamma^B_{abs}$. Hence we first calculate and visualize the dependence of these energies on the relevant parameters κ/Γ_B and Γ_B/Γ_A, in the contour plots shown in Fig. 3-3.

The way the contour plots are calculated is as follows. For each value of $(\kappa/\Gamma_B, \Gamma_B/\Gamma_A)$ in the adiabatic case, where $\kappa_{12}(t)$ and $\kappa_{23}(t)$ are given by Eq. (3.10)-(11), one tries a range of values of t_{EIT}. For each t_{EIT}, the maximum energy transferred $E_3(\%)$ over $0 < t < t_{EIT}$, denoted by $max(E_3, t_{EIT})$, is calculated together with the total energy lost at that maximum transfer. Next the maximum of $max(E_3, t_{EIT})$ over all values of t_{EIT} is selected and plotted as a single point on the contour plot in Fig. 3-3 (a). We refer to this point as the optimum energy transfer (%) in the EIT-like case for the particular $(\kappa/\Gamma_B, \Gamma_B/\Gamma_A)$ under consideration. We also plot in Fig. 3-3 (d) the corresponding value of the total energy lost (%) at the optimum of E_3. We repeat these calculations for all pairs $(\kappa/\Gamma_B, \Gamma_B/\Gamma_A)$ shown in the contour plots. In the constant-κ transfer case, for each $(\kappa/\Gamma_B, \Gamma_B/\Gamma_A)$, the time evolution of $E_3(\%)$ and E_{lost} are calculated for $0 < t < 2/\kappa$, and optimum transfer, shown in Fig. 3-3 (b), refers to the maximum of $E_3(t)$ over $0 < t < 2/\kappa$. The corresponding total energy lost at optimum constant-κ transfer is shown in Fig. 3-3 (e). Now that we calculated the energies of interest as functions of $(\kappa/\Gamma_B, \Gamma_B/\Gamma_A)$, we look for ranges of the relevant parameters

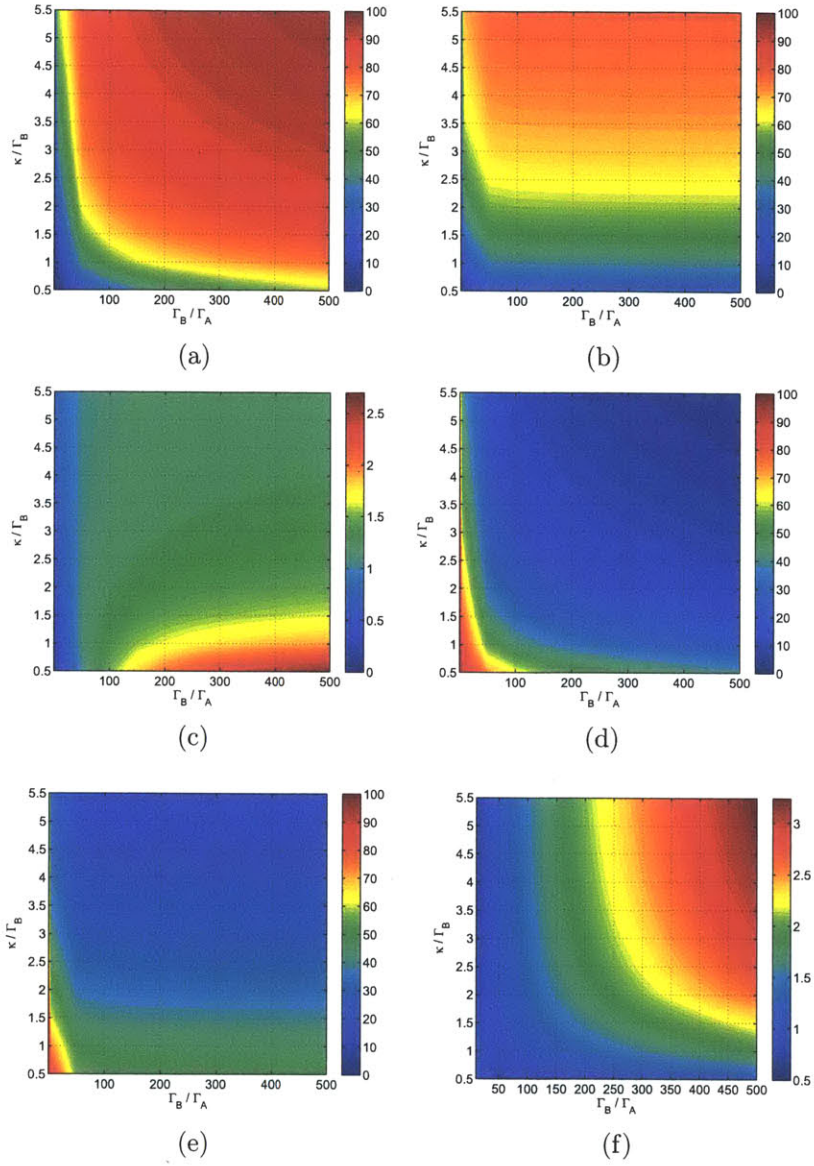

Figure 3-3: Comparison between the EIT-like and constant-κ energy transfer schemes, in the general case: (a) Optimum E_3 (%) in EIT-like transfer, (b) Optimum E_3 (%) in constant-κ transfer, (c) $(E_3)_{EIT-like}\,/(E_3)_{constant-\kappa}$, (d) Energy lost (%) at optimum EIT-like transfer, (e) Energy lost (%) at optimum constant-κ transfer, (f) $(E_{lost})_{constant-\kappa}\,/(E_{lost})_{EIT-like}$.

in which the EIT-like transfer has advantages over the constant-κ one. So, we plot the ratio of $(E_3)_{EIT-like}/(E_3)_{constant-\kappa}$ in Fig. 3-3 (c), and $(E_{lost})_{constant-\kappa}/(E_{lost})_{EIT-like}$ in Fig. 3-3 (f). We find that, for $\Gamma_B/\Gamma_A > 50$, the optimum energy transferred in the adiabatic case exceeds that in the $constant-\kappa$ case, and the improvement factor can be larger than 2. From Fig. 3-3 (f), one sees that the EIT-like scheme can reduce the total energy lost by a factor of 3 compared to the constant-κ scheme, also in the range $\Gamma_B/\Gamma_A > 50$.

Although one is usually interested in reducing the total energy lost (radiated + absorbed) as much as possible in order to make the transfer more efficient, the undersirable nature of the radiated energy makes it often important to consider reducing the energy radiated, instead of only considering the total energy lost. For this purpose, we calculate the energy radiated at optimum transfer in both the EIT-like and constant-κ schemes, and compare them. The relevant parameters in this case are κ/Γ_B, Γ_B/Γ_A, Γ^A_{rad}/Γ_A, and Γ^B_{rad}/Γ_B. The problem is more complex because the parameter space is now 4-dimensional. So we focus on those particular cross sections that can best reveal the most important differences between the two schemes. From Fig. 3-3 (c) and (f), one can guess that the best improvement in both E_3 and E_{lost} occurs for $\Gamma_B/\Gamma_A \geq 500$. Moreover, knowing that it is the intermediate object R_2 that makes the main difference between the EIT-like and constant-κ schemes, being "energy-empty" in the EIT-like case and "energy-full" in the constant-κ one, we first look at the special situation where $\Gamma^A_{rad} = 0$. In Fig. 3-4 (a) and (b), we show contour plots of the energy radiated at optimum transfer, in the constant-κ and EIT-like schemes respectively, for the particular cross section having $\Gamma_B/\Gamma_A = 500$ and $\Gamma^A_{rad} = 0$. Comparing these two figures, one can see that, by using the EIT-like scheme, one can reduce the energy radiated by a factor of 6.3 or more.

To get a quantitative estimate of the radiation reduction factor in the general case where $\Gamma^A_{rad} \neq 0$, we calculate the ratio of energies radiated at optimum transfers in

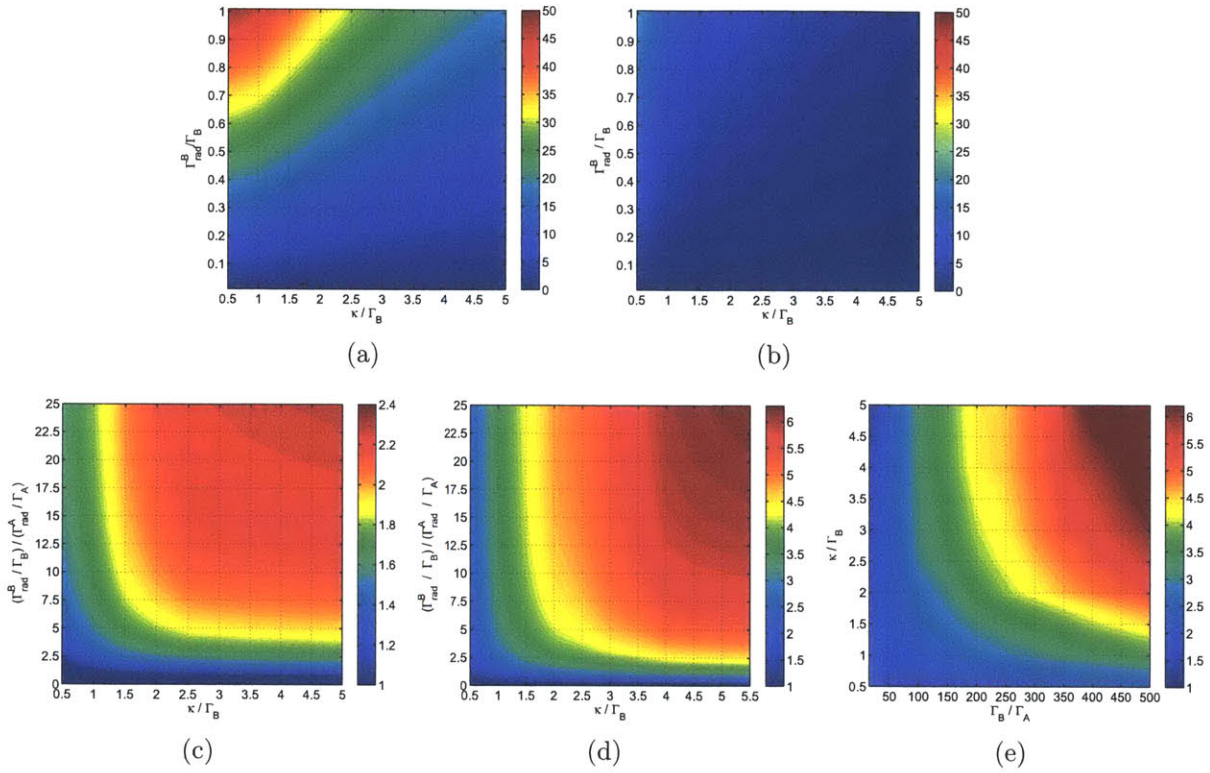

Figure 3-4: Comparison between radiated energies in the EIT-like and constant-κ energy transfer schemes: (a) $E_{rad}(\%)$ in the constant-κ scheme for $\Gamma_B/\Gamma_A = 500$ and $\Gamma^A_{rad} = 0$, (b) $E_{rad}(\%)$ in the EIT-like scheme for $\Gamma_B/\Gamma_A = 500$ and $\Gamma^A_{rad} = 0$, (c) $(E_{rad})_{constant-\kappa}\ /(E_{rad})_{EIT-like}$ for $\Gamma_B/\Gamma_A = 50$, (d) $(E_{rad})_{constant-\kappa}\ /(E_{rad})_{EIT-like}$ for $\Gamma_B/\Gamma_A = 500$, (e) $[(E_{rad})_{constant-\kappa}\ /(E_{rad})_{EIT-like}]$ as a function of κ/Γ_B and Γ_B/Γ_A, for $\Gamma^A_{rad} = 0$.

both schemes, namely,

$$\frac{(E_{rad})_{constant-\kappa}}{(E_{rad})_{EIT-like}} = \frac{\int_0^{t_{opt}^{constant-\kappa}} \left\{ \frac{\Gamma_{rad}^B}{\Gamma_{rad}^A} |a_2^{constant-\kappa}(t)|^2 + \left(|a_1^{constant-\kappa}(t)|^2 + |a_3^{constant-\kappa}(t)|^2 \right) \right\} dt}{\int_0^{t_{opt}^{EIT-like}} \left\{ \frac{\Gamma_{rad}^B}{\Gamma_{rad}^A} |a_2^{EIT-like}(t)|^2 + \left(|a^{EIT-like}(t)|^2 + |a_3^{EIT-like}(t)|^2 \right) \right\} dt} \tag{3.15}$$

which depends only on $\Gamma_{rad}^B/\Gamma_{rad}^A$, the time-dependent mode amplitudes, and the optimum transfer times in both schemes. The latter two quantities are completely determined by κ/Γ_B, and Γ_B/Γ_A. Hence the only parameters relevant to the calculations of the ratio of radiated energies are $\Gamma_{rad}^B/\Gamma_{rad}^A$, κ/Γ_B, and Γ_B/Γ_A, thus reducing the dimensionality of the investigated parameter space from 4 down to 3. For convenience, we multiply the first relevant parameter $\Gamma_{rad}^B/\Gamma_{rad}^A$ by Γ_A/Γ_B, which becomes $\left(\Gamma_{rad}^B/\Gamma_B\right)/\left(\Gamma_{rad}^A/\Gamma_A\right)$, i.e. the ratio of quantities that specify what percentage of each object's loss is radiated. Next, we calculate the ratio of energies radiated as a function of $\left(\Gamma_{rad}^B/\Gamma_B\right)/\left(\Gamma_{rad}^A/\Gamma_A\right)$ and κ/Γ_B, in the two special cases $\Gamma_B/\Gamma_A = 50$, and $\Gamma_B/\Gamma_A = 500$, and we plot them in Fig. 3-4 (c) and (d) respectively. We also show, in Fig. 3-4 (e), the dependence of $(E_{rad})_{constant-\kappa}/(E_{rad})_{EIT-like}$ on κ/Γ_B and Γ_B/Γ_A, for the special case $\Gamma_{rad}^A = 0$. As can be seen from Fig. 3-4 (c)-(d), the EIT-like scheme is less radiative than the constant-κ scheme whenever $(\Gamma_{rad}^B/\Gamma_B)$ is larger than $(\Gamma_{rad}^A/\Gamma_A)$, and the radiation reduction ratio increases as Γ_B/Γ_A and κ/Γ_B are increased (see Fig. 3-4 (e)).

3.5 Conclusion

In this chapter, an efficient weakly radiative energy transfer scheme between two identical resonant objects was proposed based on an EIT-like transfer of the energy through a mediating resonant object with the same resonant frequency. The problem was analyzed using CMT illustrating how the fundamental principle underlying the proposed energy transfer scheme is similar to the known EIT process [10] in which there is complete population transfer between two quantum states. The EIT-like

scheme was then compared to the constant-κ one, as the relevant parameters of the system are varied. All this was motivated initially by specializing to the problem of witricity-like wireless energy transfer between inductively-coupled metallic loops. However, the proposed scheme, not being restricted to the special type of resonant inductive coupling, is not bound only to wireless energy transfer, and could potentially find applications in various other unexplored types of coupling between general resonant objects. In fact, in this context, the work presented here generalizes the concept of EIT, previously known as a quantum mechanical phenomenon that exists in microscopic systems, to a more general energy transfer phenomenon, between arbitrary classical resonant objects. The focus was on the particular example of electromagnetic resonators, but the nature of the resonators and their coupling mechanisms could as well be quite different, e.g. acoustic, mechanical, etc... In the next chapter, we will develop a CMT model and investigate the electromagnetic coupling between an arbitrary polarization source and the modes of the photonic structure in which it is embedded. In particular, we will derive an analytical expression for the electric field generated by the polarization source in the most general case when the polarization source has arbitrary spatiotemporal dependence and when the photonic structure itself isn't necessarily a photonic crystal and possibly involves nonlinearities, gain, loss, etc...

Chapter 4

Purcell effect in nonlinear photonic structures: A coupled mode theory analysis *

4.1 Introduction

Since the emergence of nonlinear optics [2] in 1961, and the major breakthroughs [41, 42, 43, 44, 45, 46] that subsequently marked its growth, the field of nonlinear optics has been producing continuous scientific excitement: Numerous nonlinear optical phenomena have been discovered, and have significantly impacted scientific progress in many respects [47, 48, 49, 50, 51]. In particular, the generation of terahertz radiation via nonlinear optical techniques, such as optical rectification, difference frequency generation and parametric generation, presents unique features [52, 53] that are also proving to be very useful tools for biomedical imaging, sensing, spectroscopy, sample characterization, etc. This wealth of applications, made possible by nonlinear phenomena, has necessitated the perpetual quest for improving the efficiency of nonlinear optical processes. In addition to phase matching considerations, the Purcell effect [11], well known for its ability to control spontaneous emission rates, provides a

*Rafif E. Hamam, Mihai Ibanescu, Evan J. Reed, Peter Bermel, Steven G. Johnson, Erich Ippen, J. D. Joannopoulos, and Marin Soljačić, Optics Express **16**, 12523, (2008).

hint on how to boost nonlinear conversion efficiencies, by modifying (increasing) the local density of photonic states (LDOS) at the location of the nonlinear polarization source. A light source embedded in a photonic structure is known to emit faster when the LDOS at the source frequency is larger, and this applies for light sources originating from nonlinear polarization as well. Photonic crystals constitute a versatile tool for tailoring LDOS, and hence they offer extraordinary opportunities to enhance nonlinear effects [54], also by exploiting the Purcell effect.

So far, a few proposals have been made to exploit the Purcell effect in order to improve the nonlinear optical response of photonic crystals. For instance, the effective medium approach has been used to investigate how the density of states affects the conversion efficiency for second harmonic generation in a one dimensional photonic band gap (PBG) structure [55]. The finite-difference time-domain (FDTD) method [56] could also be used to solve the problem numerically [57, 54, 58]. However, a better comprehension of the problem requires a more elaborate treatment, that elucidates the implications of the Purcell effect on efficient nonlinear conversion. A method using Green's function has been developed [59, 60] to calculate the nonlinear optical response of a photonic crystal to an external polarization source. In this respect, temporal coupled mode theory [4] (CMT) seems to be of great promise, since it provides a physically intuitive framework that easily addresses the problem, where the photonic structure can also exhibit any sort of loss or gain.

In this chapter, we use CMT to study the response of a general photonic structure to a traveling polarization source of arbitrary extent. As long as CMT is still valid (i.e. as long as the quality factors are large enough), absorptive and/or radiative losses, as well as gain, can be modeled. Given the current challenge of making high-power terahertz sources, we illustrate our general approach, by proposing, for the first time, a method for efficient generation of terahertz waves by optical rectification in a two-dimensional (2D) photonic crystal. For this purpose, we theoretically investigate sending an optical beam into an appropriately designed 2D nonlinear photonic crystal, and we use our CMT-based result to calculate the total energy radiated at terahertz frequencies. Next, we repeat the same calculation for the terahertz gen-

erated energy, but now using the exact FDTD method instead. The obtained close agreement between the CMT and FDTD results, not only validates our CMT approach, but it also suggests that our CMT treatment could serve as a substantially less numerically intensive alternative to the FDTD method, for certain systems of interest. For instance, in problems involving frequencies and wavelengths that range over many orders of magnitude, FDTD calculations are very difficult to perform. However, it is far less intricate to solve such problems by using our CMT-based formalism. A specific example of such cases is the generation of terahertz radiation by optical rectification, where a proper FDTD calculation should involve simultaneously wavelengths in both the optical and terahertz regimes, resulting in a computational burden that could go beyond the capabilities of currently available computers. Such complications, however, are not present if one uses our CMT formalism, instead.

The structure of the chapter is as follows: In section 4.2, we develop the CMT model and calculate the generated electric field in the most general case. Then, in section 4.3, we discuss how the Purcell effect follows from our general result, by calculating the power emitted by a point dipole source. Finally, in section 4.4, we apply our work to the specific problem of THz generation and compare our results with FDTD results.

4.2 Coupled-mode-theory model

To start with, we suppose that there exists a polarization source $\vec{P}(\vec{r},t)$ inside a photonic structure. Let $(\vec{E}_\nu, \vec{H}_\nu)$ label a mode of the source-free solutions to Maxwell's equations obtained by using linear real indices of refraction of the photonic structure; while calculating the modes $(\vec{E}_\nu, \vec{H}_\nu)$, we assume that the photonic structure does not involve any loss, gain or nonlinearities. The effects of loss/gain will be addressed perturbatively below through the use of CMT. Nonlinear effects that are of interest for THz generation are included in the sense that the polarization source itself is generated through nonlinear effects, starting from some external electric fields of different frequencies; this polarization source, in turn excites the modes of the struc-

ture. $\{\vec{D}_\nu(\vec{r})/\sqrt{\varepsilon(\vec{r})}\}$, where $\vec{D}_\nu(\vec{r}) = \varepsilon(\vec{r})\vec{E}_\nu(\vec{r})$, form a complete set [3], since they are eigenmodes of the hermitian operator $\frac{1}{\sqrt{\varepsilon(\vec{r})}}\vec{\nabla} \times \left(\vec{\nabla} \times \frac{1}{\sqrt{\varepsilon(\vec{r})}}\right)$. The polarization source $\vec{P}(\vec{r},t)$ induces in the structure electromagnetic fields $\vec{E}(\vec{r},t)$ and $\vec{H}(\vec{r},t)$. If we denote the electric displacement vector by $\vec{D}(\vec{r},t)$, then $\vec{D}(\vec{r},t)/\sqrt{\varepsilon(\vec{r})} = \sqrt{\varepsilon(\vec{r})}\vec{E}(\vec{r},t)$ can be expressed as a linear superposition [3] of $\vec{D}_\nu(\vec{r})/\sqrt{\varepsilon(\vec{r})} = \sqrt{\varepsilon(\vec{r})}\vec{E}_\nu(\vec{r})$. Hence, we can write

$$\vec{E}(\vec{r},t) = \sum_\nu a_\nu(t) \frac{\vec{E}_\nu(\vec{r})}{\sqrt{\int d^3\vec{r} \frac{\varepsilon(\vec{r})}{2} \left|\vec{E}_\nu(\vec{r})\right|^2}} \tag{4.1}$$

where a_ν is the amplitude of the mode labeled by ν, normalized such that $|a_\nu|^2$ is the total energy in that particular mode.

A note about the mode labeling is in place. For a uniform medium, the modes are labeled by the wavevector $\vec{k}$ and polarization σ, hence ν is to be identified with $(\vec{k},\sigma)$ in this case. For a photonic crystal, it is most convenient to label the modes by a band index n, a polarization σ, and a Bloch wavevector $\vec{k}$ that lies in the first Brillouin zone. Therefore, we identify $\nu \equiv (n,\vec{k},\sigma)$ for photonic crystals. For a finite photonic crystal structure, the allowed values of $\vec{k}$ consistent with boundary conditions, are discrete. However, for infinite photonic crystal structures, there is a continuum of allowed values of $\vec{k}$, and the sum in Eq. (4.1) transforms into a discrete sum over n and an integral over $\vec{k}$.

Treating each mode as a CMT port, the CMT equation for the mode amplitude a_ν becomes [4]

$$\frac{da_\nu}{dt} = -i\omega_\nu a_\nu - (\Gamma^\nu_{rad} + \Gamma^\nu_{abs} - \Gamma^\nu_g)a_\nu + \kappa_\nu s^\nu_+ \tag{4.2}$$

where ω_ν is the frequency of the mode labeled by ν, Γ^ν_{rad} and Γ^ν_{abs} are the rates of radiative (out of the structure) and absorptive decay, respectively, and Γ^ν_g is the rate of gain. $\kappa_\nu s^\nu_+$ is the square root per unit time of the portion of the polarization source's energy, that couples to the photonic structure; i.e. this term models the excitation of the mode of the structure by the polarization source. From Poynting's

theorem, $\kappa_\nu s_+^\nu$ is given by

$$\kappa_\nu s_+^\nu = \frac{\int d^3\vec{r}\prime \vec{J}(\vec{r}\prime,t)\cdot\vec{E}_\nu^*(\vec{r}\prime)}{\sqrt{\int d^3\vec{r}\frac{\varepsilon(\vec{r})}{2}\left|\vec{E}_\nu(\vec{r})\right|^2}} \tag{4.3}$$

where the current density source $\vec{J}(r,t)$ is related to the polarization $\vec{P}(\vec{r},t)$ by $\vec{J}(r,t) \equiv \partial\vec{P}(\vec{r},t)\Big/\partial t$. The general solution to Eq. (4.2) can be easily obtained by multiplying both sides by an integrating factor $\Xi(t) = e^{\int^t (i\omega_\nu+\Gamma_{rad}^\nu+\Gamma_{abs}^\nu-\Gamma_g^\nu)dt'}$, to get

$$\frac{d}{dt}(a_\nu(t)\Xi(t)) = \Xi(t)\kappa_\nu s_+^\nu \tag{4.4}$$

Hence

$$a_\nu(t) = a_\nu(t_o)e^{-i\omega_\nu(t-t_o)}e^{-\left(\Gamma_{rad}^\nu+\Gamma_{abs}^\nu-\Gamma_g^\nu\right)(t-t_o)}$$

$$+\int_{t_o}^{t} dt' \frac{\int_{\text{all space}} d^3\vec{r}\prime\, \vec{J}(\vec{r}\prime,t')\cdot\vec{E}_\nu^*(\vec{r}\prime)}{\sqrt{\int d^3\vec{r}\frac{\varepsilon(\vec{r})}{2}\left|\vec{E}_\nu(\vec{r})\right|^2}} e^{-i\omega_\nu(t-t')}e^{-\left(\Gamma_{rad}^\nu+\Gamma_{abs}^\nu-\Gamma_g^\nu\right)(t-t')} \tag{4.5}$$

where t_o is any reference time preceding the turn-on of the polarization source, and $t > t_o$.

Plugging this into Eq. (4.1), the electric field induced in the photonic structure becomes

$$\vec{E}(\vec{r},t) = \sum_\nu \frac{\vec{E}_\nu(\vec{r})}{\sqrt{\int d^3\vec{r}\frac{\varepsilon(\vec{r})}{2}\left|\vec{E}_\nu(\vec{r})\right|^2}} a_\nu(t_o)e^{-i\omega_\nu(t-t_o)}e^{-\left(\Gamma_{rad}^\nu+\Gamma_{abs}^\nu-\Gamma_g^\nu\right)(t-t_o)} +$$
$$\sum_\nu \frac{\vec{E}_\nu(\vec{r})}{\int d^3\vec{r}\frac{\varepsilon(\vec{r})}{2}\left|\vec{E}_\nu(\vec{r})\right|^2} \int_{t_o}^{t} dt' \int_{\text{all space}} d^3\vec{r}\prime\, \vec{J}(\vec{r}\prime,t').\vec{E}_\nu^*(\vec{r}\prime)e^{-i\omega_\nu(t-t')}e^{-\left(\Gamma_{rad}^\nu+\Gamma_{abs}^\nu-\Gamma_g^\nu\right)(t-t')} \tag{4.6}$$

The total power radiated out of the photonic structure, at time t, is $\sum_\nu 2\Gamma_{rad}^\nu|a_\nu(t)|^2$,

and the flux through a surface A at time t is

$$\int_A \vec{S} \cdot d\vec{a} = \int_A \left\{ \text{Real}\left[\vec{E}(\vec{r},t)\right] \times \text{Real}\left[\vec{H}(\vec{r},t)\right] \right\} \cdot d\vec{a} \tag{4.7}$$

where $\vec{E}(\vec{r},t)$ is given by Eq. (4.6), and $\vec{H}(\vec{r},t)$ can be obtained from Faraday's law: $\vec{\nabla} \times \vec{E}(\vec{r},t) = -\partial[\mu_0 \vec{H}(\vec{r},t)] \Big/ \partial t$, μ_0 being the magnetic permeability.

4.3 Connection with Purcell effect

To get more intuition on the above result, let us consider an oscillating point dipole of moment $\vec{p}$, embedded at position $\vec{r}_o$ in the structure. If we denote the dipole's angular frequency by ω_s, then the polarization is $\vec{P}(\vec{r},t) = \vec{p}\delta^{(3)}(\vec{r}-\vec{r}_o)e^{-i\omega_s t}$. Let us further assume that $\Gamma_g^\nu = 0 \; \forall \; \nu$ (no gain). In this case, the resulting mode amplitude a_ν becomes

$$a_\nu = \frac{-i\omega_s \vec{p} \cdot \vec{E}_\nu^*(\vec{r}_o)}{i\left(\omega_\nu - \omega_s\right) + \left(\Gamma_{rad}^\nu + \Gamma_{abs}^\nu\right)} \frac{e^{-i\omega_s t}}{\sqrt{\int d^3\vec{r} \frac{\varepsilon(\vec{r})}{2} \left|\vec{E}_\nu(\vec{r})\right|^2}} \tag{4.8}$$

Denoting $\Gamma^\nu = \Gamma_{rad}^\nu + \Gamma_{abs}^\nu$, the total radiated power $\mathcal{P} = \sum_\nu 2\Gamma_{rad}^\nu |a_\nu|^2$ is

$$\mathcal{P} = \sum_\nu \frac{\Gamma_{rad}^\nu}{\left(\omega_\nu - \omega_s\right)^2 + \left(\Gamma^\nu\right)^2} \frac{2(\omega_s)^2 \left|\vec{p} \cdot \vec{E}_\nu^*(\vec{r}_o)\right|^2}{\int d^3\vec{r} \frac{\varepsilon(\vec{r})}{2} \left|\vec{E}_\nu(\vec{r})\right|^2} \tag{4.9}$$

In the limit of zero loss ($\Gamma^\nu \to 0$), we have $\Gamma^\nu \Big/ \left\{\left(\omega_\nu - \omega_s\right)^2 + \left(\Gamma^\nu\right)^2\right\} \to \pi\delta\left(\omega_\nu - \omega_s\right)$. Hence

$$\mathcal{P} = \frac{4\pi(\omega_s)^2 |\vec{p}|^2}{\varepsilon(\vec{r}_o)} \sum_\nu \frac{\varepsilon(\vec{r}_o) \left|\hat{p} \cdot \vec{E}_\nu^*(\vec{r}_o)\right|^2 \delta\left(\omega_\nu - \omega_s\right)}{\int d^3\vec{r}\varepsilon(\vec{r}) \left|\vec{E}_\nu(\vec{r})\right|^2} \tag{4.10}$$

If we further assume that there is perfect polarization match between the source and all the modes ν, then $\left|\hat{p} \cdot \vec{E}_\nu^*(\vec{r}_o)\right|^2 = \left|\vec{E}_\nu(\vec{r}_o)\right|^2 \; \forall \; \nu$, and

$$\mathcal{P} = \frac{4\pi(\omega_s)^2 |\vec{p}|^2}{\varepsilon(\vec{r}_o)} g(\omega_s, \vec{r}_o) \tag{4.11}$$

where

$$g(\omega_s, \vec{r}_o) = \sum_\nu \frac{\varepsilon(\vec{r}_o)\left|\vec{E}_\nu(\vec{r}_o)\right|^2 \delta(\omega_\nu - \omega_s)}{\int d^3\vec{r}\varepsilon(\vec{r})\left|\vec{E}_\nu(\vec{r})\right|^2} \tag{4.12}$$

is the local density of photonic states at $\vec{r}_o$. Therefore, the total radiated power (even from a nonlinear source) is proportional to the local density of states, as expected from the Purcell effect. It also increases quadratically with the dipole moment of the polarization source.

4.4 Connection with Doppler radiation in a PhC crystal

To verify further the validity if our approach, we apply our general result (Eq. (4.6)) to another well-known special case: the radiation emitted by an oscillating dipole moving with a fixed velocity $\vec{v}$ in a PhC [61]. In this case, the current density can be simply expressed as

$$\vec{J}(\vec{r}, t) = \vec{j}_o e^{-i\omega_s t}\delta(\vec{r} - \vec{v}t) \tag{4.13}$$

Plugging this into Eq. (4.6), and assuming that $\Gamma^\nu = 0 \; \forall \; \nu$, we obtain

$$\vec{E}(\vec{r}, t) = \sum_\nu \frac{\vec{E}_\nu(\vec{r})}{\int d^3\vec{r}\frac{\varepsilon(\vec{r})}{2}\left|\vec{E}_\nu(\vec{r})\right|^2} \int_{-\infty}^{t} dt' e^{-i\omega_s t'} \vec{j}_o.\vec{E}^*_\nu(\vec{v}t')e^{-i\omega_\nu(t-t')} \tag{4.14}$$

As we mentioned before, the modes of a PhC are labeled by $\nu \equiv (n, \vec{k}, \sigma)$, and from Bloch theorem $\vec{E}_{n\vec{k}}(\vec{r}) = e^{i\vec{k}.\vec{r}}\vec{u}_{n\vec{k}}(\vec{r})$, where $\vec{u}_{n\vec{k}}(\vec{r})$ has the periodicity of the PhC, and hence only reciprocal lattice vectors $\vec{G}$ appear in its Fourier expansion $\vec{u}_{n\vec{k}}(\vec{r}) = \sum_{\vec{G}} \vec{e}_{n\vec{k},\vec{G}} e^{i\vec{G}.\vec{r}}$. Hence Eq. (4.14) becomes

$$\vec{E}(\vec{r}, t) = \sum_{n\vec{k}\sigma} \frac{\vec{E}_{n\vec{k}\sigma}(\vec{r})}{\int d^3\vec{r}\frac{\varepsilon(\vec{r})}{2}\left|\vec{E}_{n\vec{k}\sigma}(\vec{r})\right|^2} \sum_{\vec{G}} \vec{j}_o.\vec{e}^*_{n\vec{k},\vec{G}} \int_{-\infty}^{t} dt' e^{-i\omega_s t'} e^{-i(\vec{k}+\vec{G}).\vec{v}t'} e^{-i\omega_{n\vec{k}\sigma}(t-t')} \tag{4.15}$$

which simply evaluates to

$$\vec{E}(\vec{r},t)=\sum_{n\vec{k}\sigma}\frac{\vec{E}_{n\vec{k}\sigma}(\vec{r})}{\int d^3\vec{r}\frac{\varepsilon(\vec{r})}{2}\left|\vec{E}_{n\vec{k}\sigma}(\vec{r})\right|^2}\sum_{\vec{G}}\frac{-i[\vec{j}_o.(\vec{e}_{n\vec{k},\vec{G}})^*]}{\omega_{n\vec{k}\sigma}-[\omega_s+(\vec{k}+\vec{G}).\vec{v}]}e^{-i[\omega_s+(\vec{k}+\vec{G}).\vec{v}]t} \tag{4.16}$$

which is consistent with Eq.(1) in [61] in the limit $\omega_{n\vec{k}\sigma}\simeq\omega_s+(\vec{k}+\vec{G}).\vec{v}$.

Thus, while our formalism properly reproduces the well-known predictions of the Purcell effect (Eq. (4.11)) and of Doppler radiation in PhCs (Eq. (4.16)), its scope extends further, because it analyzes in a systematic and quantitative way the behavior of an arbitrary polarization in any photonic structure. Note that the polarization source can have complicated spatiotemporal variations, and is not restricted to static collections of point dipoles.

A glance at Eq. (4.6) enables us to recognize the various possibilities for boosting the magnitude of the electric electric field $\vec{E}(\vec{r},t)$ induced in the structure by a given external polarization source. Clearly, we need to have the largest possible density of modes that yield a significant value of the summand on the right hand side of Eq. (4.6). To achieve such large values of the summand, the phase-matched modes ought to have their resonance frequency ω_ν close enough to the frequency ω_s of the source. Their polarization should also be matched to the source's polarization, and their spatial overlap with the source's extent should be considerable. This latter requirement suggests that the modes should be highly concentrated at the position of the source. And of course, we should attempt to reduce losses to the lowest possible level.

4.5 Numerical validation and terahertz generation

4.5.1 Optimizing the structure

Having identified the essential features required to enhance the response of a photonic structure to an external polarization source, and motivated by the existing need for

efficient high-power terahertz sources, we apply our formalism to the specific problem of terahertz generation by optical rectification. To this end, we select a nonlinear photonic crystal (PhC) structure that features a $\chi^{(2)}$ nonlinearity, and that satisfies as many as possible of the criteria stated in section 4.2. Before getting into the details of the structure, let's outline briefly the fundamental principles. We propose to excite our PhC structure with a beam centered around an optical frequency; we denote the optical electric field by $\vec{E}_{opt}$. By optical rectification, this optical beam generates a polarization $\mathcal{P}^{THz} \sim \chi^{(2)} E_{opt} E^*_{opt}$ in the terahertz frequency range [62]. According to our formalism, the rate at which this polarization $\mathcal{P}^{THz}$ excites terahertz waves depends on several considerations pertaining to the PhC structure. First, one of course strives to use a material with $\chi^{(2)}$ as large as possible. Next, another option is to increase the magnitude of $\vec{E}_{opt}$ as much as possible; ultimately there is a limit to which one can pursue this approach, imposed by the optical breakdown threshold. Finally one can adjust the properties of the PhC structure at terahertz frequencies, to achieve high density of states and good spatial overlap between the terahertz modes and the source $\mathcal{P}^{THz}$.

A promising PhC structure, in this respect, has been proposed by some of the current authors [63]. Here we consider a very similar structure consisting of a two-dimensional (2D) square lattice of rods in air. The spacing between the rods is denoted by a, the nonlinear susceptibility by $\chi^{(2)}$, and the linear refractive index at terahertz frequencies by n_r. The rods of radius r are connected along the x-direction by thin waveguides, each of thickness t and consisting of the same material as the rods. These waveguides are needed, in order to provide guiding for the optical light. A unit cell of the 2D periodic PhC structure is depicted in Fig. 4-1 (a) as a color contour plot of the linear dielectric function $\epsilon(x, y)$. A similar contour plot is presented in Fig. 4-1 (b), showing 5 units of the structure in each direction, together with the optical beam.

If we choose $r = 0.13a$, $t = 0.04a$ and $n_r = 3.5$ (close to the refractive index of GaP [64, 65], commonly used for terahertz generation by optical rectification), the second band ($n = 2$) of the transverse magnetic (σ =TM) modes is characterized by a saddle point where the band is ultraflat, and consequently the density of states is

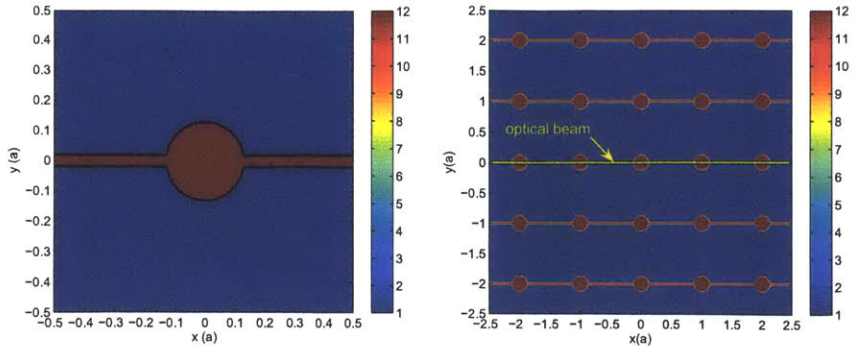

(a) (b)

Figure 4-1: Color contour plot of the dielectric function $\epsilon(x, y)$ of the 2D PhC srtucture: (a) $1a \times 1a$ cell, and (b) $5a \times 5a$ cell, showing the optical beam through the central waveguide.

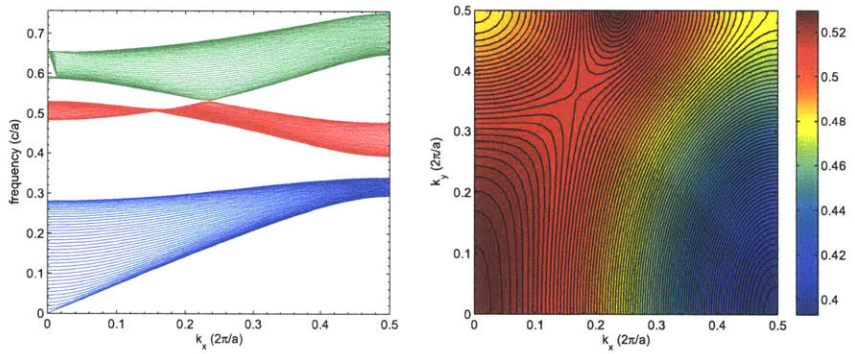

(a) (b)

Figure 4-2: (a) Projected band diagram of the first three bands. (b) Color contour plot of the second band, showing the saddle point where the band is narrowest.

enhanced. The band structure was computed by preconditioned conjugate-gradient minimization of the block Rayleigh quotient in a planewave basis, using a freely available software package [66]. The projected band diagram for σ =TM, shown in Fig. 4-2 along with a color contour plot of the second band, indicates that the second TM band is narrowest at $k_x = 0.1559(2\pi/a)$, where it has a width of only 1.27% around the central frequency $f = 0.509(c/a)$; thereby if the targeted frequency is e.g. $f = 1$ THz, one needs to choose $a = 152.7\mu$m.

So, the PhC structure we have chosen indeed has a considerable number of modes polarized along z (parallel to the rods), with $k_x = 0.1559(2\pi/a)$, and by choosing a appropriately, we can tune the structure to be optimized for any frequeny in the THz regime. Since we are interested in the very small frequency range around the

saddle point of the second band, we consider a narrow-bandwidth excitation. To this end, we assume that the optical beam is sent through the waveguide centered at the origin, and is particularly chosen such that the current density $\vec{J}^{THz}$ associated with the polarization source $\mathcal{P}^{THz}$, has the form:

$$\vec{J}^{THz}(x,y;t) = \hat{z}e^{ik_x^s x - \frac{y^2}{2\zeta^2}} e^{-i\omega_s t - \frac{(t-500a/c)^2}{2\tau^2}} \tag{4.17}$$

where $k_x^s = 0.1559(2\pi/a)$ to ensure phase matching with the modes at the ultraflat portion of the second band. The angular frequency of the terahertz polarization source is $\omega_s = 0.509(2\pi c/a)$, and the values of the remaining parameters are: $\zeta = 0.02a$ and $\tau = 100(a/c)$. The time t is expressed in units of a/c. Since $\vec{J}^{THz}$ points along $\hat{z}$, all the TM modes have their polarization perfectly matched to that of the source. For convenience in subsequent calculations, and because $\vec{J}^{THz}(x,y;t)$ is separable in space and time, we write it as

$$\vec{J}^{THz}(x,y;t) = \vec{J}^{THz}_{space}(x,y) \cdot \mathcal{F}(t) \tag{4.18}$$

where

$$\vec{J}^{THz}_{space}(x,y) = \hat{z}e^{ik_x^s x - \frac{y^2}{2\zeta^2}} \tag{4.19}$$

and

$$\mathcal{F}(t) = e^{-i\omega_s t - \frac{(t-500a/c)^2}{2\tau^2}} \tag{4.20}$$

We also set $\vec{J}^{THz}(x,y;t) = 0$ for $t < 0$ and $t \geq 1000a/c$.

Up to this point most of the criteria for efficient THz generation have been met, and we are left with the issue of the spatial overlap between the modes ($n = 2$; $k_x = 0.1559(2\pi/a), k_y$; σ =TM) and the terahertz polarization source. The degree of localization of the modes $\vec{E}_{n=2;(k_{x=0.1559(2\pi/a)},k_y;\sigma=TM)}(\vec{r})$ at the source's extent can be checked by looking at the color contour plot of

$$w_{k_y}(x,y) \equiv \varepsilon(x,y) \left| \vec{E}_{n=2;(k_{x=0.1559(2\pi/a)},k_y;\sigma=TM)}(x,y) \right|^2 \tag{4.21}$$

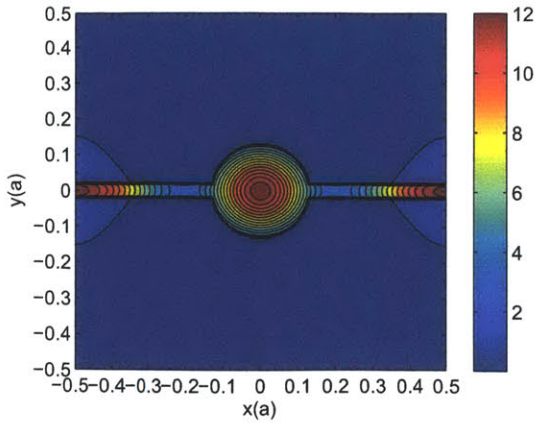

Figure 4-3: Color contour plot of $w_{k_y=0}(x, y)$.

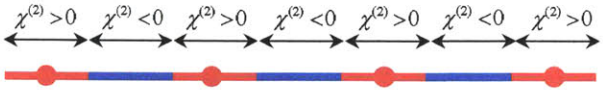

Figure 4-4: Periodically poled PhC structure. The red portions correspond to the original orientation of the nonlinear crystal when $\chi^{(2)}$ is positive, while in the blue portions, the crystal's orientation is flipped resulting in a negative $\chi^{(2)}$.

for several k_y values. We computed the fields $\vec{E}_{n=2;(k_{x=0.1559(2\pi/a)},k_y;\sigma=TM)}(\vec{r})$ by using the same software package [66], and calculated $w_{k_y}(x, y)$ for different k_y values. A representative plot is shown in Fig. 4-3 for $k_y = 0$. Despite the good localization of the modes of interest close to the source's extent, this does not guarantee an optimum for the overlap integral

$$\mathcal{O}_{n\vec{k}} \equiv \int_{\text{all space}} d^3\vec{r}\, \vec{J}^{THz}_{space}(\vec{r}) \cdot \vec{E}^{*}_{n\vec{k}}(\vec{r}) \tag{4.22}$$

for $n = 2$. Indeed, for most of the different possible k_y in the first brillouin zone, the integrand of the overlap integral $\mathcal{O}_{n=2;(k_x=k_x^s,k_y)}$ oscillates along $\hat{x}$, and hence integrates to a negligible value. That is, for $n = 2$ and for many k_y, the integrand is observed to flip the sign at $x \simeq \pm 0.25a$. One way to circumvent this problem is to periodically pole the structure every half period. More specifically, we propose to flip the sign of $\chi^{(2)}$ at $x = \pm(0.25a + \ell\ 0.5a)$ where ℓ is a zero or positive integer, as illustrated in Fig. 4-4. Mathematically, this corresponds to multiplying the integrand in Eq. (4.22) by a factor $q(x')$, which is $+1$ in regions where $\chi^{(2)}$ is positive, and -1 where $\chi^{(2)}$ is

negative. In this way, the integrand of the overlap integral $\mathcal{O}_{n=2;\vec{k}}$ preserves the same sign for most of x, and therefore the integral evaluates to a substantially higher value than without any poling. Although this looks similar to quasi-phase matching [67], one should keep in mind that our motivation behind poling was to prevent the overlap integral of the 'second' band from vanishing. For the first band, the integrand of the overlap integral $\mathcal{O}_{n=1;\vec{k}}$ does not change sign along $\hat{x}$, and so we wouldn't have to pole the structure if we were interested in modes of the first band. Similarly, if we were interested in modes of the third band, we would have to use a poling configuration different from that used in the second band. Also note that although periodic poling leads to much more efficient coupling between the nonlinear polarization source and the second-band modes of the PhC structure, all the linear properties on which the numerical calculations are based, remain intact.

4.5.2 Calculation of generated energy

Let us now calculate the total emitted energy at THz frequencies. First, we need to calculate the electric field $\vec{E}(\vec{r},t)$ induced by the THz current source (Eq. (4.17)) in the periodically poled PhC structure, using Eq. (4.6). We consider a time of $t = 1010(a/c)$ (which is $10a/c$ later than source turn-off), and we assume that $a_{n\vec{k}} = 0 \; \forall \; (n,\vec{k})$ prior to source turn-on at $t = 0$; this corresponds to the case where none of the modes of the PhC were excited before $t = 0$. We use only modes with $k_x = 0.1559(2\pi/a) = k_x^s$, and we further assume $\Gamma_g^{n\vec{k}} = \Gamma_{abs}^{n\vec{k}} = 0$. From Eq. (4.6), it is evident that we cannot proceed before computing the following two functions of k_y

$$\mathcal{O}^{poled}_{all\ space}(k_y) \equiv \int\limits_{\text{all space}} d^3\vec{r}' q(x') \vec{J}^{THz}_{space}(\vec{r}') \cdot \vec{E}^*_{n=2;(k_x^s,k_y)}(\vec{r}')$$

$$= \int\limits_{\text{all space}} d^3\vec{r}' q(x') e^{ik_x^s x' - \frac{y'^2}{2\zeta^2}} \hat{z} \cdot \vec{E}^*_{n=2;(k_x^s,k_y)}(\vec{r}') \qquad (4.23)$$

and

$$\mathcal{T}_t(k_y) \equiv e^{-i\omega_{(n=2;k_x^s,k_y)}t} \int\limits_0^t dt' \mathcal{F}(t') e^{i\omega_{(n=2;k_x^s,k_y)}t'}$$

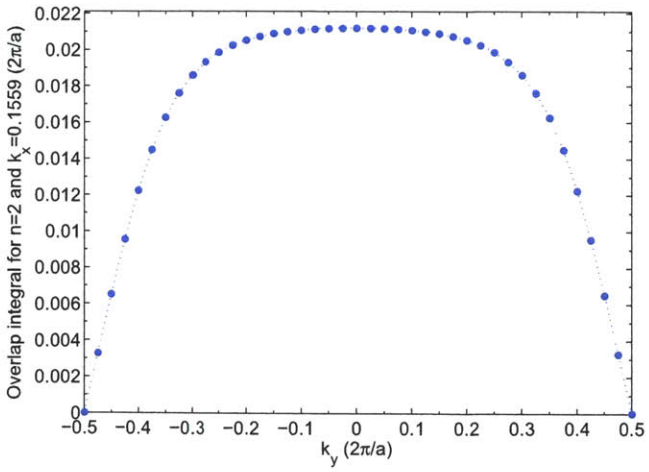

Figure 4-5: Overlap integral $\mathcal{O}^{poled}_{one\ period}$ as a function of k_y for modes at the narrowest portion ($k_x = 0.1559(2\pi/a)$) of the second band.

$$= e^{-i\omega_{(n=2;k_x^s,k_y)}t} \int_0^t dt' e^{-i(\omega_s - \omega_{(n=2;k_x^s,k_y)})t' - \frac{(t'-500a/c)^2}{2\tau^2}} \tag{4.24}$$

The integral in Eq. (4.23) can be simplified by noting that in a PhC, the electric fields can be written as

$$\vec{E}_{n\vec{k}}(\vec{r}) = e^{i\vec{k}.\vec{r}}\vec{u}_{n\vec{k}}(\vec{r}) \tag{4.25}$$

where $\vec{u}_{n\vec{k}}(\vec{r})$ has the same periodicity as the PhC. Consequently, $\mathcal{O}^{poled}_{all\ space}(k_y)$ becomes

$$\mathcal{O}^{poled}_{all\ space}(k_y) = \int_{\text{all space}} d^3\vec{r}\prime q(x') e^{-ik_y y' - \frac{y'^2}{2\zeta^2}} \hat{z} \cdot \vec{u}^*_{n=2;(k_x^s,k_y)}(\vec{r}\prime) \tag{4.26}$$

The integrand of this equation is periodic function of x'. Hence the integral over all x' simplifies to the number $\mathcal{N}_x$ of periods in the x-direction times the integral over a single period, with x' ranging from $-a/2$ to $a/2$. The integration over y' can also be taken to range between $-a/2$ and $a/2$, because the optical beam is sent through the central waveguide only, and thus $\vec{J}^{THz}_{space}$ is zero for y' outside the interval $[-a/2, a/2]$. Therefore

$$\mathcal{O}^{poled}_{all\ space}(k_y) = \mathcal{N}_x \cdot \mathcal{O}^{poled}_{one\ period}(k_y) \tag{4.27}$$

$$\mathcal{O}^{poled}_{one\ period}(k_y) = \int_{-a/2}^{a/2} dx' \int_{-a/2}^{a/2} dy' q(x') e^{-ik_y y' - \frac{y'^2}{2\zeta^2}} \hat{z} \cdot \vec{u}^*_{n=2;(k_x^s,k_y)}(\vec{r}\prime) \tag{4.28}$$

To evaluate this integral, we discretize space with a resolution of 256 gridpoints/a, and calculate the TM fields $\vec{u}_{n=2;(k_x^s,k_y)}(\vec{r})$ based on the TM modes $\vec{E}_{n=2;(k_x^s,k_y)}(\vec{r})$ computed by using the software package [66]. Note that the TE modes have their electric field polarized in the xy plane, and hence they don't get excited by the polarization source. So, in all what follows, when we refer to PhC modes, we consider only the TM modes, and we omit the notation $\sigma = TM$. While computing the modes, we make sure that all of them have their phases fixed relative to each other, and that they are all normalized in the same way, e.g. such that $\int\limits_{one\ cell} d^3\vec{r}\varepsilon(\vec{r}) \left|\vec{E}_{n,\vec{k}}(\vec{r})\right|^2 = 1$. A plot of the overlap integral $\mathcal{O}^{poled}_{one\ period}(k_y)$, as a function of k_y, is shown in Fig. 4-5 (after poling is performed). Clearly, the integral takes values close to maximum for most of the k_y's. The reason for which it vanishes as $k_y \to \pm 0.5(2\pi/a)$ is that those modes have an extended node over the whole source, and consequently the integrand in Eq. (4.28) vanishes almost everywhere, either because the source is zero or because the electric field of the modes is zero. So whether the structure is poled or not, the overlap integral vanishes for modes with $k_y = \pm 0.5(2\pi/a)$.

Next, we calculate $\mathcal{T}_t(k_y)$ at $t = 1010(a/c)$, using the previously calculated band structure. Eq. (4.6) becomes

$$\vec{E}(\vec{r},t) = \sum_{k_y} \frac{\vec{E}_{n=2;(k_x^s,k_y)}(\vec{r})}{\mathcal{N}_x\mathcal{N}_y/2}\mathcal{N}_x \cdot \mathcal{O}^{poled}_{one\ period}(k_y)\mathcal{T}_t(k_y) \tag{4.29}$$

Since the PhC is of infinite extent in the x and y directions, the k_y values consistent with periodic boundary conditions, become dense enough that to a good approximation, the discrete sum over k_y can be converted into an integral

$$\vec{E}(\vec{r},t) = \frac{a\mathcal{N}_y}{2\pi} \int\limits_{-0.5(2\pi/a)}^{0.5(2\pi/a)} dk_y \frac{\vec{E}_{n=2;(k_x^s,k_y)}(\vec{r})}{\mathcal{N}_x\mathcal{N}_y/2}\mathcal{N}_x \cdot \mathcal{O}^{poled}_{one\ period}(k_y)\mathcal{T}_t(k_y) \tag{4.30}$$

$$= \frac{a}{\pi} \cdot \int\limits_{-\pi/a}^{\pi/a} dk_y \vec{E}_{n=2;(k_x^s,k_y)}(\vec{r})\mathcal{O}^{poled}_{one\ period}(k_y)\mathcal{T}_t(k_y) \tag{4.31}$$

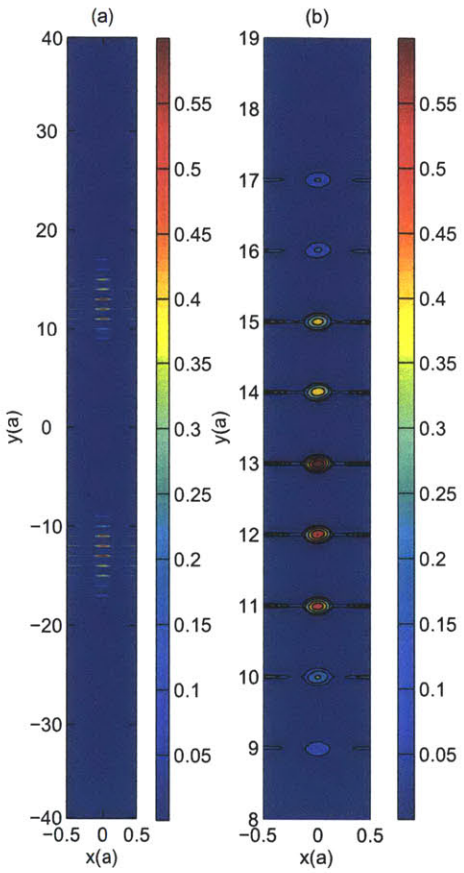

Figure 4-6: CMT calculations: (a) Color contour plot of the unnormalized terahertz energy density $\epsilon(x,y)|E(x,y,t)|^2$ at $t = 1010(a/c)$, in a 2D box of size $1a \times 80a$. (b) A zoom-in version of the plot in (a), showing more details of the interval $y \in \pm\,[8a, 19a]$. Note that the optical beam was originally sent through the waveguide at $y = 0$.

To calculate the total emitted energy, we consider calculating the electric field $\vec{E}(\vec{r},t)$ at time $t = 1010(a/c)$, over a region of space large enough in the y direction, hoping that no energy would have left it by $t = 1010(a/c)$. So, we take our computational domain to be a 2D box of size $1a$ along x and $80a$ along y. To save on computational memory, we use a spatial resolution of 64 gridpoints/a only, and calculate the TM fields $\vec{E}_{n=2;(k_x^s,k_y)}$ for 201 equally spaced values of k_y ranging between $-\pi/a$ and π/a, again using the software package [66]. Next we multiply each field labeled with k_y, by $\mathcal{O}^{poled}_{one\ period}(k_y) \cdot \mathcal{T}_{1010(a/c)}(k_y)$, and sum the resulting fields over all values of k_y. Finally, we multiply the result by a/π and obtain the THz electric field induced by the optical beam in the PhC at time $t = 1010(a/c)$. Note that we attempted to use a denser grid of k_y values (334 equidistant k_y points), without change in the final result. The electric energy density profile $\epsilon(x,y)|E(x,y,t)|^2$, at $t = 1010(a/c)$, can now be simply calculated over the computational domain, and is presented in Fig. 4-6.

As we intended, all the emitted energy is still confined inside our large computational domain; more specifically, the energy density is non-vanishing only in the regions $y \in \pm[8a, 19a]$. Thus, to calculate the total emitted energy, it is sufficient to integrate the energy density at $t = 1010(a/c)$ over a 2D box of size $1a$ along x, and large enough in the y direction to enclose the regions $y \in \pm[8a, 19a]$. Setting $a = 1$, we obtain a value of 0.7108 for the total THz energy emitted in the PBG. To enable comparison with the FDTD results, we normalize the total emitted energy and express it in dimensionless units; that is, we divide the above-mentioned integral of the energy density in the poled PhC case, by the same quantity (0.1839) similarly calculated in an unpoled bulk of the same nonlinear material as that used in the PhC structure. We obtain a dimensionless value of 3.86.

To confirm the validity of our analytical model in general, and of the result for the total emitted energy in the specific example of terahertz generation, we repeat exactly the same calculation for the terahertz emitted energy, but now instead of using our analytical formalism, we employ the finite-difference time-domain (FDTD) method [56], using a freely available software package with subpixel smoothing for increased

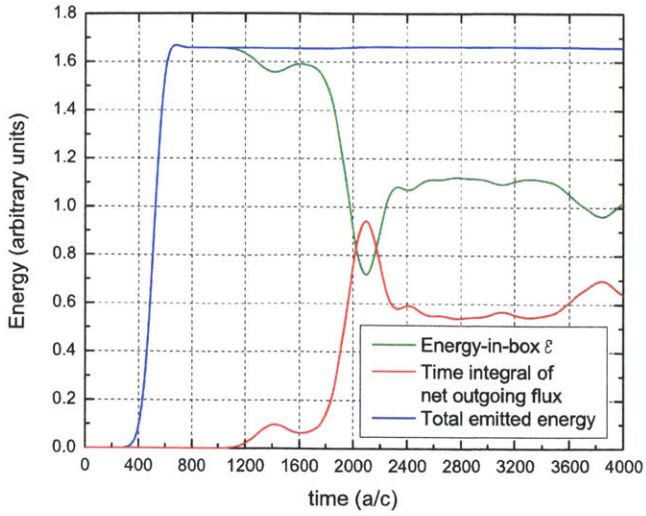

Figure 4-7: FDTD calculation for the terahertz emitted energy in the PhC structure (not normalized to the bulk).

accuracy [6]. We consider a computational cell (centered at the origin) of size $1a$ along x, and $90a$ along y, and we discretize the structure with a resolution of 128 pixels/a. We send the same source described before through the waveguide centered at $y = 0$, and we impose Bloch-periodic boundary conditions along x, with a wavevector $k_x = 0.1559(2\pi/a)$. At the boundaries in the y direction, we set up perfectly matched layers (PML), each of thickness $3a$. We simulate the effect of periodic poling by explicitely reversing the sign of the polarization source at $x = \pm 0.25a$. To compute the total emitted energy at terahertz, we record the time evolution of the energy $\mathcal{E}$ in a box of size $1a$ (along x)$\times 80a$ (along y), centered at the origin. We also place flux calculation planes at $y = \pm 40a$, and compute the flux that leaves through each of the flux planes as a function of time. The total emitted energy at a particular time t is then given by the sum of the integral up to time t of the net flux through the flux planes, and the energy remaining in the box surrounded by the flux planes, at time t.

The time development of the energy $\mathcal{E}$, and of the time integral of the net flux, is shown in Fig. 4-7, together with the total emitted energy, which is given by their sum. Again, we normalize the total energy emitted in the poled PhC to that emitted in the corresponding unpoled bulk, and we get a value of 3.94 in dimensionless units. Thus, our result for the normalized emitted energy at terahertz, differs only by $\simeq$

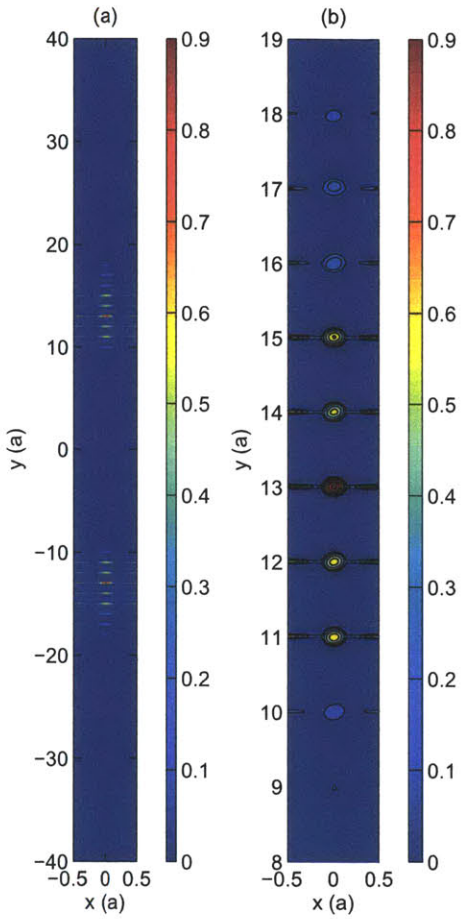

Figure 4-8: FDTD calculations: (a) Color contour plot of the terahertz energy density $\epsilon(x,y)|E(x,y,t)|^2$ at $t = 1010(a/c)$, in a 2D box of size $1a \times 80a$. (b) A zoom-in version of the plot in (a), showing more details of the interval $y \in \pm[8a, 19a]$. Note that the optical beam was originally sent through the waveguide at $y = 0$.

2% from the exact result computed by FDTD. To gain even more confidence in the validity of our analytical result, we perform FDTD calculations of the energy density profile in the poled PhC, at $t = 1010(a/c)$, and we show the result as a color contour plot in Fig. 4-8. The agreement between Fig. 4-6 and Fig. 4-8 is indeed remarkable; not only do we get a coincidence of the intervals $y \in \pm[8a, 19a]$ in which the energy density is nonvanishing, but also the waveguides at which the energy density is maximum occur at exactly the same position, namely $y = \pm 13a$, according to both methods (FDTD and CMT-based analytics). In addition to validating our analytical CMT-based formalism, the agreement of the results obtained from our analytical model with the exact FDTD results, suggests that our approach would work as a simpler alternative to the numerically intensive FDTD method. Our procedure has the advantage of being far less demanding than the brute-force FDTD technique, in terms of the computational time and resources, especially in problems involving frequencies that range over many orders of magnitude, such as terahertz generation by optical rectification. To get a concrete estimate, we mention that, although we assumed the terahertz polarization source to be given from the beginning, and dealt with terahertz frequencies only, the calculation of energy density profile shown in Fig. 4-6 took around 15 minutes on a single processor, while the FDTD calculations resulting in Fig. 4-7 took around 10 hours using 360 processors on a supercomputer. Finally, the FDTD calculations of Fig. 4-8 took $\simeq$ 10 minutes using 32 processors on a supercomputer when a spatial resolution of 64 gridpoints/a was used, and $\simeq$ 2 hours using 360 processors when the spatial resolution was 128 gridpoints/a. Note that the only assumption on which our analytical formalism is based is that CMT be valid, meaning that the rates Γ^ν be much smaller than the frequency ω_ν for each mode ν of the photonic structure [4].

4.6 Conclusion

In conclusion, an analytical model for calculating the electric field produced by an external polarization source in a photonic structure was developed in this chapter.

This formalism can provide an insight on enhancing the efficiency of nonlinear effects. The procedure was illustrated by applying it to the specific case of terahertz generation by optical rectification in a 2D nonlinear photonic crystal, and the results were checked against exact calculations based on the FDTD method. The good agreement between the results and the FDTD calculations validates the proposed analytical approach, and suggests that this technique can be used as a potentially simpler alternative to FDTD, as long as CMT is applicable. The scope of the presented formalism extends far beyond that of the well-known Purcell effect in the sense that the polarization source doesn't have to be a point dipole source located at some fixed position, rather it can be extended and can propagate in the photonic structure according to some arbitrary spatiotemporal dependence. In the next chapter, we will be studying diffraction-less propogation of beams in properly designed photonic crystal structures. Namely, we will be proposing a hybrid photonic crystal structure that supports broadband diffraction-less propogation over long distances.

Chapter 5

Broadband super-collimation in a hybrid photonic crystal structure *

5.1 Introduction

The ability of photonic crystals (PhCs) to "mold the flow of light" [3] has resulted in a remarkable variety of fascinating optical phenomena, such as omnidirectional reflection [68, 69, 70], low loss bends [71], high-Q cavities [71], efficient spontaneous emission [72, 73], negative refraction [74, 75], enhancement of nonlinear effects [76], ultrafast all-optical switching [77], and thermal emission design [78]. Super-collimation, or diffractionless light propagation, represents an additional important property made possible by the powerful versatility of PhCs. It was first described by Kosaka et. al [12], and subsequently by several other groups [13, 14, 15, 16, 17, 18]. In all these demonstrations of super-collimation, the nondiffractive propagation is achieved by having a flat constant-frequency contour (CFC) in the dispersion relation of the PhC. When a beam, having the same frequency as the flat CFC, propagates in the PhC normal to the direction of the flat CFC, the Fourier components of the beam propagate with group velocities pointing in almost the same direction, and hence the beam does not spread much. However, in all the earlier observations of super-

*Rafif E. Hamam, Mihai Ibanescu, Steven G. Johnson, J. D. Joannopoulos, and Marin Soljačić, Optics Express **17**, 8109, (2009).

collimation in PhCs, the flat feature is usually confined to a not very broad frequency range around the frequency of the flat CFC, thus limiting the bandwidth over which super-collimation can be observed, and making super-collimation sensitive to variations in the frequency of the propagating monochromatic beam. For example, super-collimation has been observed along the diagonal directions of a PhC consisting of a 2D square lattice of circular holes in a dielectric [16], a schematic of which is shown in Fig. 5-1 (a). The super-collimation property in such a structure manifests itself only in a narrow frequency interval, within which the CFC's curvature flips sign. This is depicted in Fig. 5-1 (b), where we show a typical color contour plot of the first TE (electric field in the plane of periodicity) band for the structure of Fig. 5-1 (a). The change in the sign of the CFC's curvature implies the existence of a CFC with zero curvature, thus leading to super-collimation at the frequency of that particular CFC, and in a narrow frequency range around it. This stimulates the interest to search for PhC structures that support super-collimation over a larger frequency range. The band diagram of these PhCs would consist of extended frequency ranges over which the CFCs are flat enough to substantially suppress diffraction. A hint as to how to achieve this feature can be inferred from the flatness of tight-binding bands for electrons in solids [79]. The fact that tight-binding bands arise from the weak overlap between atomic orbitals inspires us to consider the simple, well-known waveguide array structure depicted in Fig. 5-1 (c). We show a typical projected band diagram for the first TM (electric field perpendicular to the plane) band for such a structure in Fig. 5-1 (d), together with a color contour plot of the first TM band in Fig. 5-1 (e). Although this structure is not commonly used for super-collimation purposes, its CFCs (in a given band) get flatter as the frequency increases. However, the curvature of these contours doesn't change sign, and hence it doesn't go through zero, which would be a conventional criterion for super-collimation. Therefore, to obtain a PhC that supports super-collimation over an extended frequency range, we consider a hybrid PhC structure that combines features from both of the above-mentioned PhC types. Namely, we propose inserting into the waveguide array structure a square lattice of circular rods having the same refractive index as the

waveguides, such that the rods are placed halfway between neighboring waveguides, with a lattice constant equal to the nearest-neighbor waveguide spacing. A schematic of this 2D hybrid structure is shown in Fig. 5-2 (a). In this chapter, we investigate the phenomenon of super-collimation in this 2D hybrid PhC structure [80, 81], and show how it simultaneously inherits useful properties from both of the structures in Fig. 5-1 (a) and Fig. 5-1 (c): the sign flip of the CFCs' concavity (due to the discrete translational symmetry) from the 2D holes-in-dielectric structure, and the extended frequency range (over 4 times the frequency range of a traditional square lattice of holes) of the flat CFCs (due to the weakly coupled waveguides), from the waveguide array structure. More specifically, in our proposed 2D PhC structure, the photonic modes of higher-order-bands have their energy mostly concentrated in the waveguides, and neighboring waveguides couple weakly, thus giving rise to tight-binding-like flat bands. So, one might be tempted to think that the rods don't play any role, and consequently that the performance of our proposed 2D structure is not very promising, given the known fact that, in linear waveguide arrays, a beam initially localized in one of the waveguides is observed to hop quickly to the other waveguides in what is known as discrete diffraction [82]. However, as we will see later in this chapter, the rods play an important role; in fact, by breaking the continuous translational symmetry along the waveguides' direction, the rods place our proposed structure at an advantage over the waveguide array, since they enable the existence of a CFC with zero concavity. On a separate note, considerations concerning the coupling of light into and out of our proposed structure are very similar to those in PhC structures previously used for supercollimation, such as the holes-in-dielectric structure studied in [16].

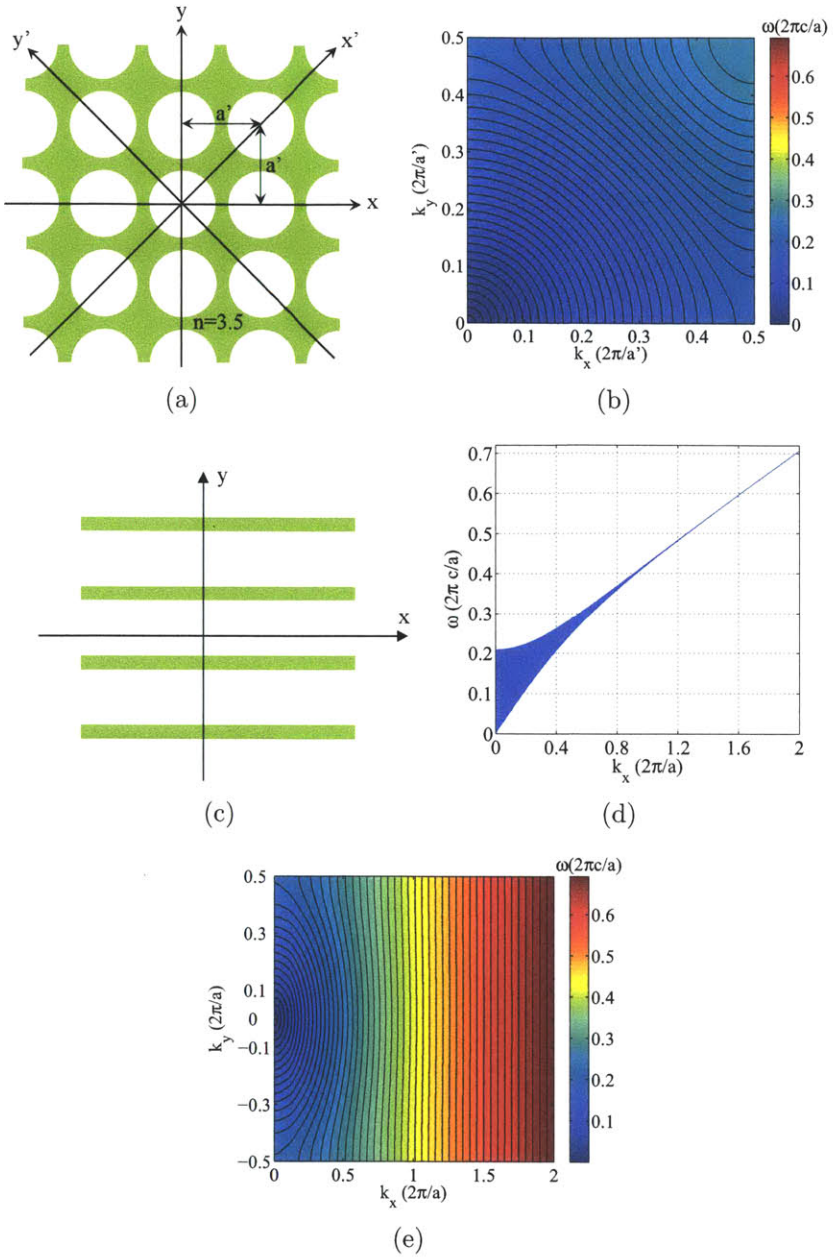

Figure 5-1: Two "often-used" low-diffraction structures. (a) Profile of the refractive index of a 2D holes-in-dielectric structure, with the dielectric having $n = 3.5$, and the holes having radius $r = 0.421a'$, where a' is the nearest-neighbor center-to-center separation between holes (the square lattice spacing). Note that the holes form a square lattice. (b) Color contour plot of the frequency of the first TE band for the structure shown in (a). (c) Profile of the refractive index for a waveguide array structure, with the waveguide having refractive index $n = 3.5$. (d) Projected band diagram of the first TM band for the waveguide array with $t = 0.2a$. (e) Color contour plot of the frequency of the first TM band for the waveguide array with $t = 0.2a$.

5.2 Super-collimation mechanism in our proposed structure

We begin the study of super-collimation in our proposed structure by considering the fourth transverse magnetic (TM) band. Our choice to operate in the fourth TM band is based on the fact that it is the lowest band having flat contours over its entire frequency range. Because of time-reversal symmetry, the dispersion relation is an even function of k_y, the y-component of the Bloch wavevector. For small values of k_y, the angular frequency is described by an expansion in terms of even powers of k_y, namely

$$\omega_4^{TM}(k_x, k_y) = \omega_4^{TM}(k_x, 0) + \alpha_4^{TM}(k_x) \cdot (k_y)^2 + \beta_4^{TM}(k_x) \cdot (k_y)^4 + ... \qquad (5.1)$$

where ω_4^{TM} denotes the angular frequency of the fourth TM band. Since we aim at the optimum super-collimation performance of our proposed structure, and since small $\alpha_4^{TM}(k_x)$ is necessary to achieve super-collimation, we search for the particular rods' radius r and waveguide thickness t that minimize the absolute value of $\alpha_4^{TM}(k_x)$, while we set the refractive index of both rods and waveguides to $n = 3.5$. We carried out such optimization calculations by using the MIT Photonic Bands (MPB [66, 83]) software. The values of r and t that give rise to flat CFCs over the largest frequency range in the fourth TM band of the proposed structure, are those that minimize the maximum (over k_x) of $|\alpha_4^{TM}(k_x)|$. The result of this optimization calculation for $\min_{r,t} \max_{k_x} |\alpha_4^{\mathrm{TM}}|$ corresponds to $r = 0.16a$ and $t = 0.2a$, where a is the lattice constant. We calculated the TM bands of this optimum structure, by using MPB, with a spatial resolution of 128 pixels/a , and we show in Fig. 5-2 (b) the projected band diagram of the lowest four TM bands. We also present in Fig. 5-2 (c) a color contour plot of the fourth TM band, as a function of k_x and k_y. Because of periodicity, k-points in the first brillouin zone are confined to the ranges $-\pi/a \leq k_x \leq \pi/a$ and $-\pi/a \leq k_y \leq \pi/a$. We show the bands only in the interval where k_x is positive,

because we are interested in propagation in the $+x$-direction for modes of the fourth band. We observe from Fig. 5-2 (b)-(c) that the flat CFCs of the fourth TM band extend almost over the entire frequency range of the fourth band, thus enabling supercollimation over a significant frequency range. Moreover, except near the edges of the fourth band, the CFCs are flat for all the values of k_y and not just in the vicinity of $k_y = 0$. This last feature indicates that our proposed structure can support supercollimation of spatially narrow beams. Note that the flattest CFC for the structure with $r = 0.16a$ and $t = 0.2a$, has angular frequency $\omega = 0.495(2\pi c/a)$.

Having found the optimum parameters for our proposed structure, we study the propagation of a beam with Gaussian envelope and angular frequency $0.495(2\pi c/a)$, along the x-direction, in one of the waveguides of our optimum structure. We represent the z-component of the electric field of such a beam as

$$E_z(x,y;t) = e^{-i\omega t} \int_{\substack{k_y \text{ values on} \\ \text{CFC of freq. } \omega}} dk_y \, e^{-(k_y)^2/2(\sigma_{k_y})^2} E^{n=4}_{(k_x,k_y)}(x,y) \equiv e^{-i\omega t} A(x,y) \qquad (5.2)$$

where $E^{n=4}_{(k_x,k_y)}(x,y)$ is the E-field of the TM Bloch modes on the CFC with $\omega = 0.495(2\pi c/a)$. We define the diffraction length L_{diff} as the distance in the x-direction that the beam propagates before the full-width at half-maximum (FWHM) of $|A(x,y)|^2$ spreads by a factor of $\sqrt{2}$ from its initial value at $x = 0$. For $\sigma_{k_y} = 0.12(2\pi/a)$, the beam is localized mostly in 3 waveguides only, as shown in Fig. 5-3 (a), and the diffraction length is $L_{\text{diff}} = 500a$. To obtain an estimate of the operational frequency width over which the CFCs are flat enough to support supercollimation, we define the frequency bandwidth B_{k_x} at a particular k_x by the expression $B_{k_x} = \max_{k_y}[(\omega_4(k_x,k_y)] - \min_{k_y}[(\omega_4(k_x,k_y)]$. A small value of B_{k_x} for a certain k_x means that the ω_4's for all values of k_y (for the particular k_x in question) are of a similar value; B_{k_x} is hence a measure of the "band flatness" at a given k_x value. The k_x-value that minimizes $|\alpha_4^{TM}(k_x)|$ is $0.25(2\pi/a)$, and the frequency bandwidth there is $B_{k_x} = 0.0008(2\pi c/a)$; the CFC associated with the minimum of $|\alpha_4^{TM}|$ has $\omega = 0.495(2\pi c/a)$. Next, we ask over which frequency range does B_{k_x} not change

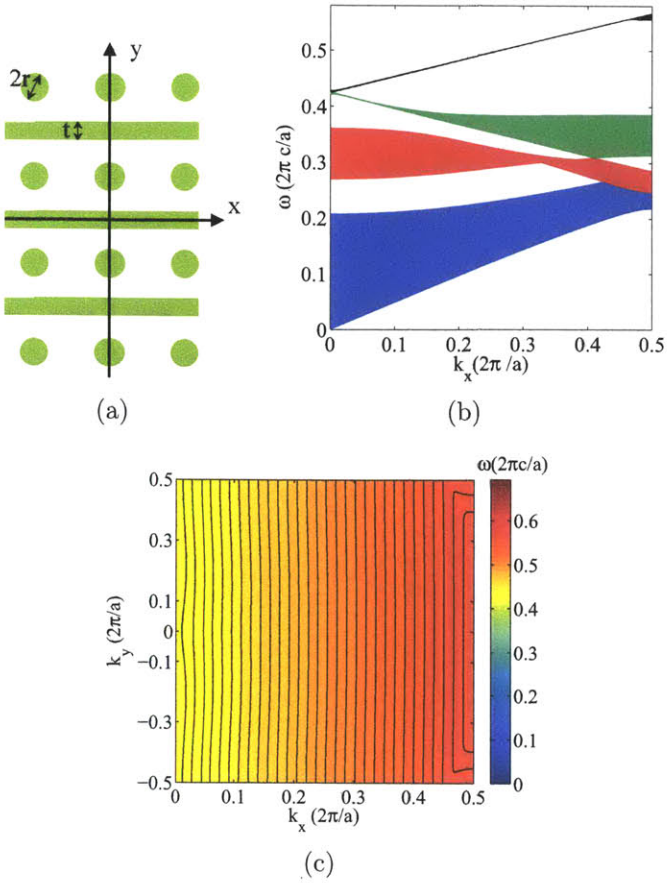

Figure 5-2: Proposed 2D PhC structure (a) Schematic of the refractive index: the rods, of radius r, and waveguides, of thickness t, (shown in green) both have $n = 3.5$, and are surrounded by air ($n = 1$). The rods form a square lattice, with lattice constant a, and the waveguides are halfway (on the y-axis) between the rods. (b) Projected band diagram of lowest four TM bands for $r = 0.16a$ and $t = 0.2a$. (c) Color contour plot of the frequency of the fourth TM band.

appreciably, to obtain a measure of the frequency range over which our structure supports super-collimation. B_{k_x} remains below $0.0008\sqrt{2}(2\pi c/a)$ in a frequency range from $0.493(2\pi c/a)$ to $0.558(2\pi c/a)$. Hence, the relative frequency range over which our optimum structure supports super-collimation is $(0.558 - 0.493)/0.495 = 0.13$, or 13%.

5.3 Super-collimation mechanism in other structures

5.3.1 Holes-in-dielectric structure

Having explored super-collimation in our structure proposed in Fig. 5-2 (a), we now study super-collimation in the two other previously-mentioned structures. We first start with the 2D holes-in-dielectric structure shown in Fig. 5-1 (a) and take the refractive index of the dielectric to be $n = 3.5$. Super-collimation was demonstrated in this structure [16], for a beam propagating along the x'-direction (diagonal), at the frequency of the flattest CFC of the first TE band. Because of the structure's mirror symmetry with respect to the plane $y' = 0$, we expand the angular frequency close to the super-collimation frequency in even powers of $k_{y'}$

$$\omega_1^{TE}(k_{x'}, k_{y'}) = \omega_1^{TE}(k_{x'}, 0) + \alpha_1^{TE}(k_{x'}) \cdot (k_{y'})^2 + \beta_1^{TE}(k_{x'}) \cdot (k_{y'})^4 + ... \qquad (5.3)$$

Since the frequency range in which we have super-collimation is known to be small in this structure, we consider maximizing the propagation length at the super-collimation frequency, instead of maximizing the frequency bandwidth around it (as we did for the structure proposed in Fig. 5-2). In order for this structure to support super-collimation over the longest propagation length, the holes' radius r' needs to be chosen such that $\omega_1^{TE}(k_{x'}, k_{y'})$ depends very little on $k_{y'}$. It is known from [16] that there always exists a value of $k_{x'}$ at which α_1^{TE} is zero since it changes sign from negative to positive. We denote this value by $k_{x'}^o$, so that we have $\alpha(k_{x'}^o) = 0$. Therefore, to minimize the dependence of $\omega_1^{TE}(k_{x'}, k_{y'})$ on $k_{y'}$, we searched for the radius r' that minimizes $|\beta(k_{x'}^o)|$, and found that $r' = 0.421a'$ where a' is the lattice constant of the holes' structure, along the x and y directions. A color contour plot of the first TE band for this optimum hole radius was obtained by using MPB, and is shown in Fig. 5-1 (b). Because of periodicity, k-points in the first brillouin zone are confined to the ranges $-\pi/a' \leq k_x \leq \pi/a'$ and $-\pi/a' \leq k_y \leq \pi/a'$. We show the bands only in the interval where k_x and k_y are positive, because we are interested in propagation

in the $+x'$-direction for modes of the first TE band. The minimum frequency bandwidth occurs at the value of $k_{x'}$ corresponding to $\omega(k_{x'}, k_{y'} = 0) = 0.1966(2\pi c/a')$, and has a value of $B_{min} = 0.0034(2\pi c/a')$. It spreads by a factor of $\sqrt{2}$ at $k_{x'}$-values with maximum frequencies equal to $0.1945(2\pi c/a')$ and $0.2004(2\pi c/a')$. Hence, the relative frequency range over which the optimum 2D holes structure supports super-collimation is 0.03 (or 3%), which is smaller than that of our proposed structure by a factor of 4.3. The minimum value (over $k^o_{x'}$) of $|\beta_1^{TE}(k^o_{x'})|$ for the optimum 2D holes structure having $r' = 0.421a'$, occurs at $k^o_{x'} = 0.457(2\pi/a')$, where we have $\omega_1^{TE}(k^o_{x'}, k_{y'} = 0) = 0.2124(2\pi c/a')$. Thus, we calculate the diffraction length of a beam with gaussian envelope and angular frequency $0.2124(2\pi c/a')$ propagating along the x' direction in the optimum 2D holes-in-dielectric structure. If we set the physical frequency of this beam to be the same as that for the optimum structure in Fig. 5-2, then the lattice constant a' in the holes' structure is related to that in Fig. 5-2 by $a' = (0.2124/0.495)a$. In this case, sending a beam of the same physical width as before corresponds to using $\sigma_{k_{y'}} = 0.12\times(0.2124/0.495)(2\pi/a')$, and yields a diffraction length of $707a' = 303.4a$. So the collimation length in this optimum 2D holes-in-dielectric structure is shorter than that in our proposed structure by a factor of 1.65, when we use beams of the same physical frequency and same physical width. We show in Fig. 5-3 (b) how such a beam spreads after it propagates, along the diagonal of the optimum 2D holes structure, a physical distance equal to the collimation length ($500a$) of our proposed structure.

5.3.2 Waveguide arrays

Now we explore how the super-collimation mechanism in our proposed structure compares to that in the waveguide array structure, shown in Fig. 5-1 (c). Again, we set the refractive index of the waveguides to $n = 3.5$, and we consider the first TM band. The reason for which we deal with the first TM band in this case, is that the physical k-point of interest (with angular frequency $\sim 0.4952\pi c/a$) now lies in the first TM band. We first study the waveguide array structure having waveguide thickness $t = 0.2a$. This structure is the same as our proposed structure, but with the rods

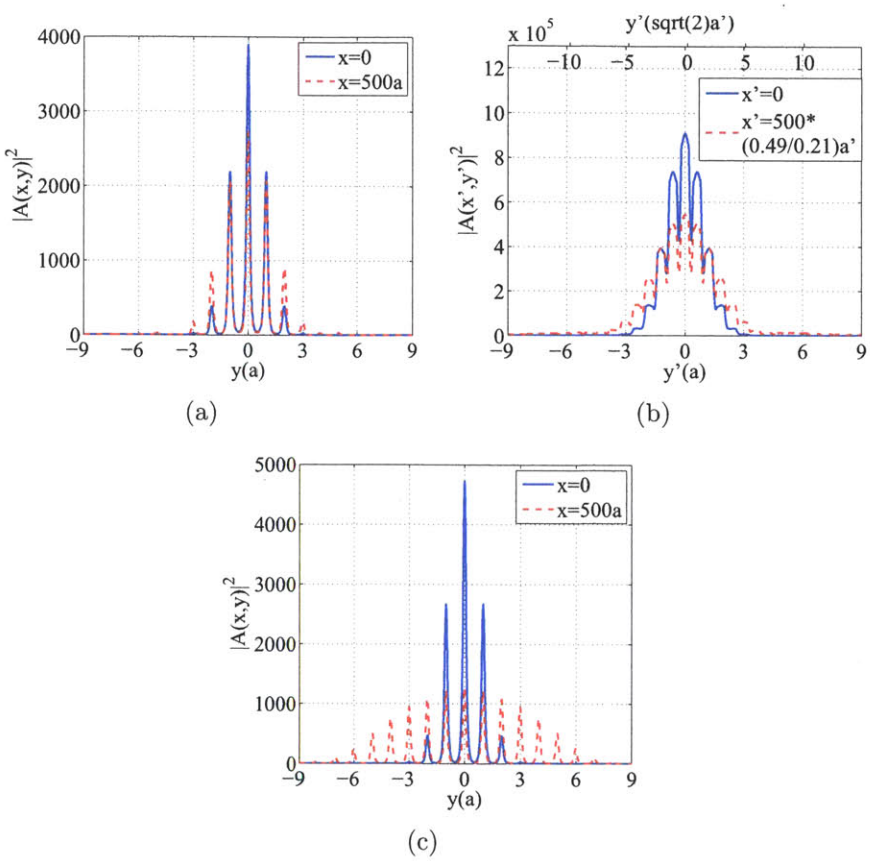

Figure 5-3: Intensity profile of the propagating beam (of angular frequency $0.495(2\pi c/a)$, and physical width corresponding to $\sigma_{k_y} = 0.12(2\pi/a)$) as a function of $y(a)$, at $x = 0$ (in blue) and at $x = 500a$ (in red), in (a) Our proposed PhC structure shown in Fig. 5-2, (b) The 2D holes structure shown in Fig. 5-1 (a), but with lattice constant $a' = (0.2124/0.495)a$, where a is the lattice constant in our proposed structure and in the waveguide array structures, (c) The waveguide array structure with $t = 0.2a$. Note that the spikes in (a) and (c) correspond to the positions of the "waveguide" strips.

removed. In Fig. 5-1 (d), we show a projected band diagram of the first TM band, and in Fig. 5-1 (e) we show a color contour plot of the first TM band. We note from these last two figures that the CFCs get flatter as the frequency increases (i.e. as k_x increases). This is a consequence of the fact that, as the frequency is increased, the modes tend to be more concentrated into the waveguides, and hence the overlaps between neighboring waveguides modes become weaker and result in narrower frequency bandwidths B_{k_x}. Note that because of the continuous translational symmetry along x, the value of k_x ranges from 0 to ∞, whereas the values of k_y range only between $-0.5(2\pi/a)$ and $0.5(2\pi/a)$ due to the discrete translational symmetry in the y-direction. In Figs. 5-1 (d) and (e), we show only $k-$points with values of k_x ranging between 0 and $2(2\pi/a)$, because modes with the frequency of interest ($f = 0.495(c/a)$) fall inside this interval; (they have $k_x \sim 1.25(2\pi/a)$). Sending a beam of the same physical angular frequency $0.495(2\pi c/a)$ and same physical width $\sigma_{k_y} = 0.12(2\pi/a)$ as in the structure of Fig. 5-2, we get a collimation length of $160a$, which is shorter than that of our proposed structure by a factor of 3.125. In Fig. 5-3 (c), we show how significantly this beam spreads after it has propagated a distance of $500a$, i.e. after it has propagated by a distance equal to the collimation length in Fig. 5-2.

One might argue that the sole role that the rods were playing in our structure was to merely increase the effective index of refraction, and therefore to push the flat CFCs to lower frequencies. To show that this is not the case, we considered a waveguide array structure having the same effective index as our proposed structure in Fig. 5-2, namely we chose the waveguide thickness to be $t' = t+\pi r^2 = [0.2+\pi(0.16)^2]a = 0.28a$. We then launched a beam of the same physical frequency $0.495(2\pi c/a)$ and the same physical width as before, and we obtained a collimation length of $275a$, which is shorter than the collimation length of Fig. 5-2, by a factor of 1.8. So the rods play a more important role in our proposed structure than just increasing the effective index. In fact, the rods break the continuous translational symmetry along the waveguide direction, and as in the holes-in-dielectric structure [16], the discrete translational symmetry along x results in a change of sign of the concavity somewhere in the

interior of the flat band. Due to this change in the sign of the concavity, there exists a value of k_x where the concavity is zero and the associated CFC is superflat. However, in the waveguide array case, the concavity never changes sign because of the continuous translational symmetry along x. And therefore, the leading deviation of $\omega(k_x, k_y)$ from $\omega(k_x, 0)$, in the waveguide array case is expected to be larger than that in our proposed structure. This accounts for the longer collimation length in our proposed structure, for beams of the same physical frequency and same physical width.

5.4 Conclusion

In conclusion, a PhC structure that exhibits long-scale super-collimation over a large frequency range was proposed in this chapter. The super-collimation phenomenon exhibited by the proposed structure was compared to that in two other often used related structures. Due to the different translational symmetries involved in each structure type, the proposed structure supports super-collimation over longer propagation lengths than waveguide arrays and 2D holes-in-dielectric PhCs. Moreover, the operational frequency range over which the proposed structure exhibits super-collimation is 4 times larger than in the 2D holes case. These two features make our proposed structure of importance in the design of super-collimation-based devices. In particular, the large operational frequency range of the proposed structure suggests the possibility of achieving super-collimation of polychromatic beams. In addition to super-collimation, the proposed structure exhibits negative refraction [74], since the group velocities of modes in the second and third TM bands, point opposite to the phase velocities. Moreover, beam steering [84] is possible in this structure as well, due to the sharp corners in the CFCs of the second and third bands. In the next chapter, we will investigate a novel class of material systems that control (reflect or transmit) light according to the incidence angle. This feature is also supported over a broad frequency range, and irrespective of the light's polarization.

Chapter 6

Angular Photonic Band Gap

6.1 Introduction

Materials and structures that strongly discriminate electromagnetic radiation based on one, or more of its properties (e.g. polarization, frequency) play an enabling role for a wide range of physical phenomena. For example, polarizers can discriminate (transmit vs. reflect) light based on its polarization[85], irrespective of the angle of incidence, over a wide range of frequencies; photonic crystals[86] (PhCs) can reflect light of certain frequencies irrespective of the angle of incidence, and irrespective of the polarization. A material-system that could transmit light based on the angle of incidence might also enable a variety of novel physical phenomena. Ideally, light incident at a particular angle (or a range of angles) would be nearly perfectly transmitted, while other angles of incidence would be nearly perfectly reflected, independent of the incoming polarization, and for as wide a range of frequencies as possible. An example where such materials could be important is solar energy applications, enabling the perfect green-house effect. Sun light has a well defined angle of incidence. A portion of sun light is reflected from solar-energy conversion devices, while a portion is re-radiated (either because of radiative recombination, or in solar-thermal systems because of thermal emission); this represents losses, which can often be substantial. If one could place a material system that would allow light at one particular angle (the one coming from the sun) to get through, while light emerging from the device

(most of which propagates at different angles) would be reflected back to the device, the efficiency of the solar-energy conversion could be improved[19, 20, 21, 22]. While material-systems that discriminate based on the polarization, or the frequency exist, we currently do not have suitable material-systems for angular discrimination. In this chapter, we present a metamaterial-system that opens precisely such desired angular gaps. For example, using realistic constituent material parameters, we present numerical calculations demonstrating a system in which light close to normal incidence is nearly perfectly transmitted for a wide range of frequencies, independent of the polarization. In contrast light of angles further from the normal (e.g. [22.5°-90°]) can be nearly perfectly reflected over $> 100\%$ fractional frequency bandgap. The crucial enabling feature of these novel meta-material systems is exploring photonic crystals whose constituents have anisotropic dielectric and/or magnetic response.

6.2 An illustrative example for angular discrimination of TM light

The metamaterial system that we propose in order to open an angular photonic gap consists of a one-dimensional (1D) periodic photonic crystal whose constituents possess anisotropic properties. To demonstrate the fundamental physics principle at work here, we first show in Fig. 6-1 a specific example of such a metamaterial that opens an angular gap for the TM (electric field is in the plane of incidence) polarization only. Later in the text we will show how to generalize our approach to both polarizations and wide frequency ranges. The anisotropy in the dielectric function of one of the layers, say layer A, represents the key factor enabling the angular discrimination of TM light. In this first example, we take layer A to have an anisotropic effective function $\epsilon_A = (1.23, 1.23, 2.43)$ whereas layer B has isotropic $\epsilon_B = 1.23$. To accomplish the required anisotropy, one could either use naturally existing anisotropic materials such as TiO_2 ($\epsilon_{TiO_2} = (2.6^2, 2.6^2, 2.9^2)$ at 590nm)[87], or explore metamaterial approach. An example of a metamaterial system that in

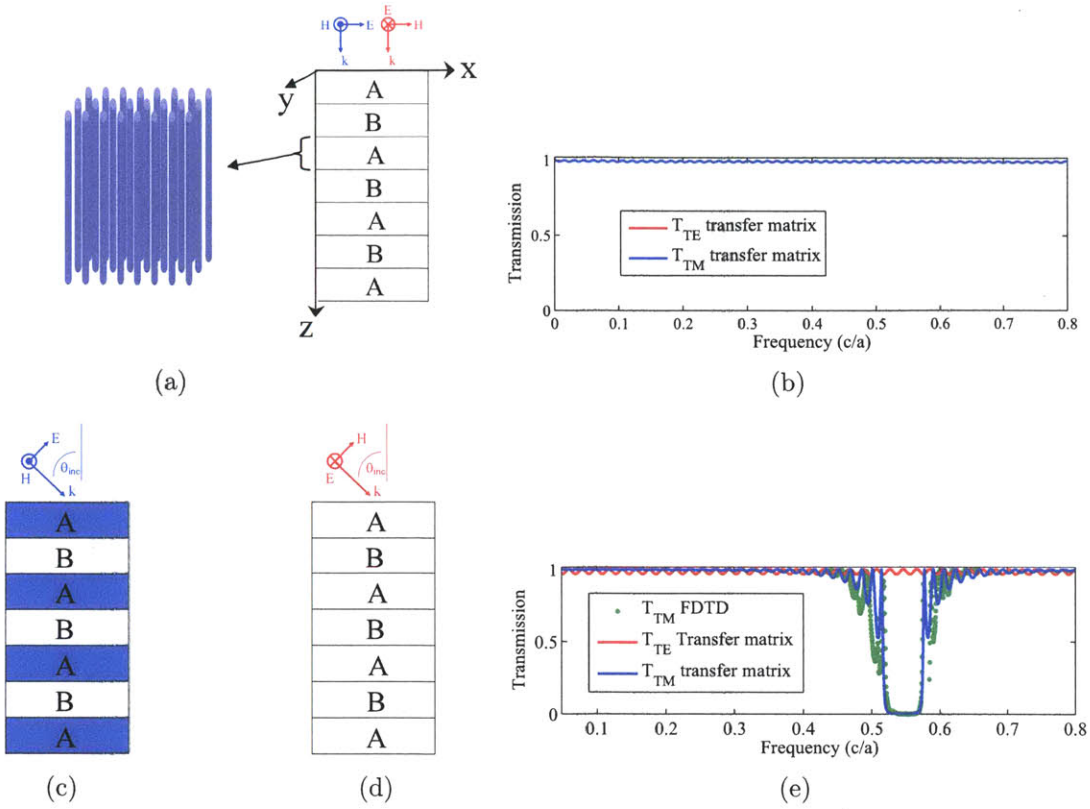

Figure 6-1: (Color online) (a) Left: Schematic diagram showing a 2D periodic square lattice of rods having an anisotropic effective $\epsilon = (1.23, 1.23, 2.43)$, in the long wavelength limit. Right: Schematic diagram showing TM (in blue) and TE (in red) polarized light incident normally from air on an anisotropic multilayer structure of period a with $\epsilon_A = (1.23, 1.23, 2.43)$ and ϵ_B=1.23. Both polarizations experience $n_A = n_B = \sqrt{1.23}$ (no index contrast). (b) Transmission spectra (obtained from the transfer matrix method (TMM)[90]) for TE- (red) and TM- (blue) polarized light normally incident from air on 30 bilayers of the structure in (a). (c)-(d) Schematic diagrams showing TM- (in (c)) and TE- (in (d)) polarized light incident at nonzero angle from air ($n_{inc} = 1$) on the structure in (a). In this case, TM light has $E_z \neq 0$ and hence experiences an index contrast between layers A and B, while TE light does not. (e) Red and blue curves: Transmission spectra (obtained from TMM) for TE- (red) and TM- (blue) polarized light incident at 45^o from air on 30 bilayers of the structure in (a). Because of the index contrast in the TM case, a TM photonic bandgap opens. Green curve: Transmission spectrum (obtained from the FDTD[6] method) for TM-polarized light incident at 45^o from air on 30 bilayers of the structure in (a), in the case when anisotropic layer A is not made from a homogeneous material, but is a metamaterial implemented from a square lattice of dielectric rods. A TM photonic bandgap opens and closely overlaps with the TM gap obtained from TMM for the uniform dielectric case.

the long wavelength limit possesses an effective epsilon of (1.23,1.23,2.43) is shown to the left of Fig. 6-1 (a), and consists of a two dimensional (2D) periodic square lattice of dielectric rods having radius $r = 0.2d$ where d (the in-plane period) equals $d = 0.1a$ (a is the thickness of each bilayer[88]), and made out of an isotropic material with[89] ϵ_{rods}=12.25. To the right of Fig. 6-1 (a), we show a schematic diagram of normally incident TM- (in blue) and TE- (in red) polarized light incident on the above-described multilayer. Since $\vec{E}$ lies in the xy-plane, both polarizations experience $n_A = n_B = \sqrt{1.23}$, so because of the absence of any contrast in the refractive index, there is no photonic bandgap and normally incident light of all frequencies and both polarizations gets transmitted through this metamaterial structure, apart for the small reflections at boundaries between the structure and air. As seen in Fig. 6-1 (b), the situation changes however when incident light makes an angle $\theta_{inc} \neq 0$ with the normal. As illustrated in the schematic of Fig. 6-1 (c), TM-polarized light incident at $\theta_{inc} \neq 0$ now has $E_z \neq 0$ and thus experiences an index contrast ($n_A^{TM} \neq n_B^{TM} = \sqrt{1.23}$); therefore, we expect a photonic bandgap (of a certain frequency width) and hence strong reflections for TM light in this bandgap. In contrast, a TE-polarized light incident at an angle $\theta_{inc} \neq 0$ still has $E_z = 0$ and thus experiences no index contrast as shown in Fig. 6-1 (d) ($n_A = n_B = \sqrt{1.23}$); therefore, it gets transmitted for all frequencies. Thereby, normally incident TM light is transmitted, while TM light incident at nonzero angles is reflected in a certain frequency range (9.3% in the case of Fig. 6-1 (e)), and this explains the physical mechanism based on which our proposed structures discriminate light with respect to the angle of incidence in that particular frequency range.

Before we discuss numerical results for transmission of various angles, polarizations, and frequencies from this multilayer structure, we provide analytical expressions for the refractive index n_A of the anisotropic layer. A simple calculation along the lines in ref.[5] starting from Maxwell's equations yields the following refractive indices ($n = c/v_{phase}$) experienced by TE and TM light respectively in the anisotropic layer A:

$$n_A^{TE} = \frac{1}{\sqrt{\frac{\cos^2\theta_A^{TE}}{\mu_{xx}^A\varepsilon_{yy}^A/\mu_o\varepsilon_o} + \frac{\sin^2\theta_A^{TE}}{\mu_{zz}^A\varepsilon_{yy}^A/\mu_o\varepsilon_o}}} \tag{6.1}$$

$$n_A^{TM} = \frac{1}{\sqrt{\frac{\cos^2\theta_A^{TM}}{\mu_{yy}^A\varepsilon_{xx}^A/\mu_o\varepsilon_o} + \frac{\sin^2\theta_A^{TM}}{\mu_{yy}^A\varepsilon_{zz}^A/\mu_o\varepsilon_o}}} \tag{6.2}$$

where θ_A^{TE} and θ_A^{TM} are the angles that TE and TM light make with respect to the normal as they propagate in layer A. These angles can be obtained from Snell's law which still holds in this anisotropic case

$$n_A^{TE}\sin\theta_A^{TE} = n_{air}\sin\theta_{inc} \tag{6.3}$$

$$n_A^{TM}\sin\theta_A^{TM} = n_{air}\sin\theta_{inc} \tag{6.4}$$

From the expressions for n_A^{TE} and n_A^{TM} we see that TE light is affected only by ε_{yy}^A, μ_{xx}^A, and μ_{zz}^A, while TM light is affected only by μ_{yy}^A, ε_{xx}^A, and ε_{zz}^A. In particular, TM light is affected by ε_{zz}^A, while TE is not, as we argued before. We can also observe that for angles θ_A close to the normal, $\sin\theta_A \simeq 0$, so Eq. (6.1) and Eq. (6.2) tell us that n_A increases only slightly with increasing anisotropy. However, for incidence angles not close to the normal, n_A increases more rapidly with increasing anisotropy, and therefore higher anisotropy in ε or μ results in higher index contrast and wider frequency gaps at those angles in our structures.

6.3 Angular discrimination irrespective of light polarization

The multilayer structure that we discussed in Fig. 6-1 discriminates angles only for TM light. Now we generalize this structure and design a different multilayer structure which is capable of discriminating angles of incidence irrespective of the polarization of light. The multilayer structure that we propose involves anisotropy in both the

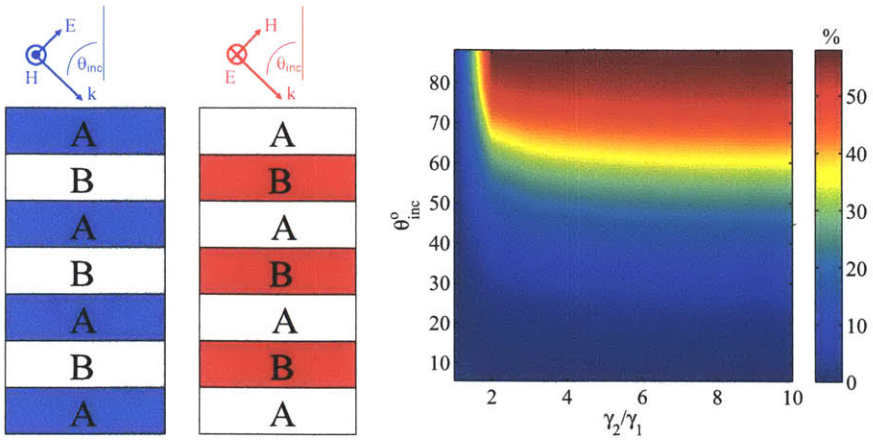

(a) (b) (c)

Figure 6-2: (Color online) (a)-(b) Schematic diagrams showing TM- (in (a)) and TE- (in (b)) polarized light incident at nonzero angle from $\epsilon_{inc} = \mu_{inc} = \gamma_1$ on an anisotropic multilayer with $\epsilon_A = \mu_B = (\gamma_1, \gamma_1, \gamma_2)$, $\epsilon_B = \mu_A = \gamma_1$. Here $\gamma_2 \neq \gamma_1$. In both of these cases, light experiences index contrasts and hence photonic bandgaps. (c) Color contour plot showing how the relative size of the TE (which equals in magnitude TM) gap changes with θ_{inc} and γ_2/γ_1 for light incident from $\epsilon_{inc} = \mu_{inc} = \gamma_1$ on the anisotropic multilayer structure of (a). The thicknesses of layers A and B were chosen to be equal ($h_A = h_B = 0.5a$) here.

dielectric function and in the magnetic permeability. More specifically, the proposed structure has $\varepsilon_B = \mu_A = \gamma_1$ while $\varepsilon_A = \mu_B = (\gamma_1, \gamma_1, \gamma_2)$[91]. For simplicity, we consider the case $\varepsilon_{inc} = \mu_{inc} = \gamma_1$ here. As shown in the schematic of Fig. 6-2 (a), TM light incident from air at nonzero angle on this structure experiences a photonic bandgap, because according to Eq. (6.2), $n_B^{TM} = \sqrt{\gamma_1}$ while $n_A^{TM} \neq \sqrt{\gamma_1}$. On the other hand, TE light incident (from air) at the same nonzero angle also experiences an index contrast because according to Eq. (6.1), $n_A^{TE} = \sqrt{\gamma_1}$ while $n_B^{TE} \neq \sqrt{\gamma_1}$. In Fig. 6-1 (c), we present a color contour plot showing how the relative size of the TE (and also TM) gap changes with θ_{inc} and with the degree of anisotropy γ_2/γ_1. This result was obtained from the TMM[90], and the thickness of layers A and B were chosen to be equal ($h_A = h_B = 0.5a$) so that the structure discriminates different angles over the same frequency interval and for both polarizations simultaneously[92]. From the contour plot, we observe that the size of the fractional gap increases only slightly with increasing anisotropy γ_2/γ_1 beyond $\gamma_2/\gamma_1 \approx 2$, which can also be seen by inspection of Eq. (6.1) and Eq. (6.2), and noticing that the achievable index contrast "saturates"

for large γ_2/γ_1 anisotropy values. Thereby, materials swith very large anisotropy do not necessarily lead to much larger bandgap in these structures. This is somewhat contrary to conventional photonic crystals where substantially large index contrast typically lead to substantially larger bandgaps. Note also that the size of the fractional frequency gap also increases with θ_{inc}.

6.4 Angular discrimination over a broad frequency range (irrespective of light polarization)

Having proposed a design structure that opens an angular gap for both polarizations over a certain frequency range, we now discuss how one can enlarge the frequency range over which this angular discrimination is exhibited. Since we are concerned with the largest fractional frequency gap that occurs simultaneously for both polarizations, we operate at quarter-wave condition (the structure obeying the quarter-wave condition at 45^o is used in the calculations of Fig. 6-3 (a), while the structure obeying the quarter-wave condition at 22.5^o is used in Fig. 6-3 (b) and Fig. 6-3 (c)). We use anisotropic $\varepsilon_A = \mu_A$ (as opposed to the previously considered case when we had anisotropic $\varepsilon_A = \mu_B$). We start with a single stack consisting of 30 homogeneous bilayers with $\varepsilon_A = \mu_A = (1.23, 1.23, 2.43)$ and $\varepsilon_B = \mu_B = 1.23$. The size of each bilayer in this stack is a. Light incident at 45^o (from air) on this stack experiences a simultaneous TE and TM photonic bandgap having a fractional frequency width of 6.94% (at quarter-wave condition). To widen this fractional frequency range, we consider a multilayer consisting of 17 such stacks, each stack being made out of 30 bilayers, however the period of each stack is chosen so that frequency gaps of different stacks are contiguous and merge together, resulting in a much larger frequency gap ($\simeq$ 17 times the size of the gap in the single gap case). More specifically, we choose the period a_i of the i^{th} stack ($i = 1, 2, .., 17$) to be $a_i = 1.0694^{(i-1)}a$, where a is the period of the first stack facing the incident light. We also choose the thickness h_A^i of layer A in the i^{th} stack to be $0.473a_i$ so that the quarter-wave condition (which

maximizes the relative size of the frequency gap) is satisfied. In Fig. 6-3 (a), we show TMM results for the transmission spectrum at 45^o incidence on the 17-stack multilayer: there is a reflection window of relative frequency size of $\simeq 104\%$ for both TE and TM polarizations simultaneously.

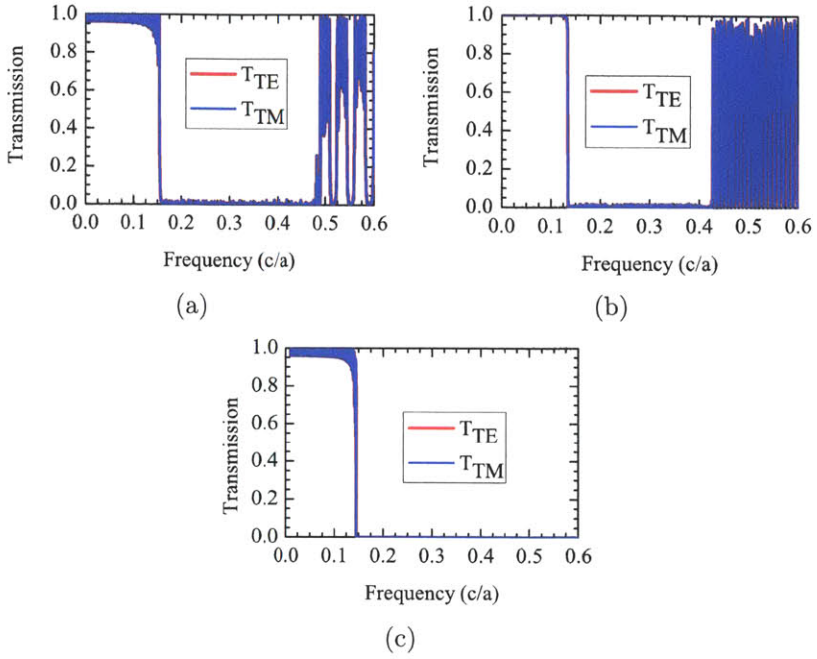

Figure 6-3: (Color online) (a) Transmission spectra, obtained using TMM, for light incident from air, at 45^o from the normal, on 17 stacks each consisting of 30 bilayers having $\epsilon_A = \mu_A = (1.23, 1.23, 2.43)$, $\epsilon_B = \mu_B = 1.23$. The period a_i of the i^{th} stack (i=1,2,..17) was chosen to be $a_i = 1.0694^{(i-1)}$, where a is the period of the first stack facing the incident light. The reflection window in this case is 103.6% wide for both TE and TM polarizations. The thickness h_A^i of layer A is $0.473a_i$ (at quarter-wave condition). (b) Transmission spectra, obtained using TMM, for light incident from air, at 22.5^o from the normal, on 71 stacks each consisting of 130 bilayers having $\epsilon_A = \mu_A = (1.23, 1.23, 2.43)$, $\epsilon_B = \mu_B = 1.23$. The period a_i of the i^{th} stack (i=1,2,..71) was chosen to be $a_i = 1.0164^{(i-1)}a$. The TE and TM reflection windows in this case are 107% wide. The thickness h_A^i of layer A is $0.494a_i$ (at quarter-wave condition). (c) Transmission spectra, obtained using TMM, for light incident from air, at 45^o from the normal, on the structure of (b). The TM reflection window in this case extends over a frequency range far wider than at 22.5^o incidence.

In Fig. 6-3 (b), we follow the same procedure and show TMM results for transmission through a multilayer designed to have a 107% wide frequency gap for both TE and TM light incident at 22.5^o from the normal, irrespective of its polarization. This structure is made of 71 stacks each consisting of 130 bilayers each having $\varepsilon_A = \mu_A = (1.23, 1.23, 2.43)$, $\varepsilon_B = \mu_B = 1.23$, and $a_i = 1.0164^{(i-1)}a$. The thickness

h_A^i of layer A was $0.494a_i$ in this case (this satisfies the quarter-wave condition). In Fig. 6-3 (c), we show TMM results for light incident at 45^o on this same structure: in this case that there is reflection at all frequencies that fall inside the reflection window shown in Fig. 6-3 (b) for 22.5^o incidence. That is, the structure that we designed to reflect 22.5^o-incident light in the frequency range ($0.13c/a \rightarrow 0.43c/a$) irrespective of its polarization, is also capable of reflecting light incident at all angles $> 22.5^o$ in this same frequency range and irrespective of the polarization; after all, bandgap of each stack is larger for 45^o incidence than for 22.5^o incidence. Light incident close-to-normal on this same structure is transmitted irrespective of its polarization. In fact, this proposed structure exhibits an angular gap (for θ_{inc} between 22.5^o and 90^o) for both polarizations simultaneously over a 107% wide frequency range.

Range of applicability of the concept we propose will depend on the availability of anisotropic materials in the frequency range of interest. As we have seen in Fig. 6-1, dielectric metamaterial approaches could be quite promising for TM polarized light. As far as TE polarization goes (where anisotropic μ is needed), one option is to explore metallo-dielectric metamaterials[93]. Another option is to split incoming light according to polarization before it enters the structure, rotate TE polarization into TM polarization, and only then allow it to continue onto our structure[94].

Structures that are capable of discriminating light based on polarization and frequency are well known and widely used. Here, we presented a novel class of structures, capable of discriminating light based on the angle of incidence. We expect that these structures could find uses in applications where it is desirable to "trap" the light of a known incidence angle. An important example of such an application is solar energy conversion; in many commercial solar farms incident angle of the sun is controlled for: solar→electrical conversion panels track the motion of the sun. Examples of such systems include solar→thermal→electrical and concentrated solar photovoltaic systems. A portion of the incident solar energy is typically reflected or reemitted from the device: this presents losses, which are often substantial. Since the angle of outgoing light is typically substantially different than the angle of the incoming light, the structures of the type we propose could be used to "trap" the outgoing energy,

and redirect it back towards the device.

Chapter 7

Conclusion

In this thesis, we have studied theoretically five novel resonant and light guiding phenomena in photonics. Wherever possible, we developed analytical models that provide a deeper and more intuitive understanding of the systems under study. We also performed detailed numerical calculations that validate the proposed analytical approaches.

We first developed a coupled mode theory model of the resonant scattering of free-space waves from resonant objects, and illustrated how it can be applied to study the resonant scattering and absorption of electromagnetic waves from spherically symmetrical scatterers and from point-like objects of any symmetry including atoms. The results provided a more intuitive understanding of many aspects of the resonant scattering and absorption phenomena, such as how small particles can absorb much more than the light incident on them. They are also of great relevance to various applications, ranging from particle sensing to meteorological optics and more importantly to the biomedical realm where they enable proper design of nanoparticles used in hyperthermic treatment of tumors among other relevant applications. Many more interesting problems in this arena can be explored using the developed model, such as the resonant scattering/absorption of plane waves from nonlinear spheres or from multi-level molecules with nonradiative coupling between the levels. Also, incident wavepackets which are localized in time and space can be modeled, by decomposing them into their plane-wave components.

Then we moved on from this far-field electromagnetic coupling of a wave to a single resonant object, to explore the near-field coupling between two high-Q resonators of the same resonant frequency. Inspired by the phenomenon of Electromagnetically Induced Transparency (EIT) which enables a complete population transfer between two quantum states coupled indirectly through an intermediate lossy one, we proposed an efficient weakly radiative energy transfer scheme between two identical resonant objects through a mediating resonant object with the same resonant frequency. We analyzed the problem using CMT, and pointed out how the fundamental principle underlying this proposed energy transfer scheme mirrors the known EIT process. In fact, in this context, the work presented here generalizes the concept of EIT, previously known as a quantum mechanical phenomenon that exists in microscopic systems, to a more general energy transfer phenomenon, between arbitrary classical resonant objects. We focused on the particular example of electromagnetic resonators, but the nature of the resonators and their coupling mechanisms could as well be quite different, e.g. acoustic, mechanical, etc... Thus, the proposed scheme could potentially find applications in various other unexplored types of coupling between general resonant objects.

We next analyzed the problem of a polarization source of arbitrary spatio-temporal dependence embedded in a general photonic structure (not necessarily a PhC) involving any sort of nonlinearities, gain or loss. We developed an analytical model based on CMT, and calculated the electric field generated by the source in the photonic structure. Then, we investigated how the implications of this formalism can provide an insight on enhancing the efficiency of nonlinear effects, and illustrated the procedure in the specific case of terahertz generation by optical rectification in a 2D nonlinear photonic crystal. We validated the approach by considering limiting cases such as the Purcell effect and Cerenkov radiation in PhCs, and also by checking the results against exact calculations based on the FDTD method. Then, we proposed the developed procedure as a potentially simpler and less-demanding alternative to the brute-force FDTD technique, especially in problems involving frequencies that range over many orders of magnitude, such as terahertz generation by optical rectification.

The proposed CMT-based technique could therefore enable a better understanding of systems that current limitations in computational resources could prevent from analyzing through FDTD.

Then we theoretically investigated how one could design photonic crystals that would support diffraction-less propagation over long distances, i.e. supercollimation. While in previously done studies the supercollimation feature is confined to a narrow frequency range, we proposed a hybrid 2D PhC structure exhibiting supercollimation over an operational fractional frequency range that is 4 times that in often used structures. We performed Beam Propagation Method calculations that illustrate the supercollimation mechanism in the proposed structure, which could be of importance in the design of super-collimation-based devices. In particular, the large operational frequency range of our proposed structure suggests the possibility of achieving supercollimation of polychromatic beams, thus enabling longer interaction distances between broadband light and various components embedded in the photonic structure. Many other interesting features of the proposed structure, such as directional thermal emission and beam steering, remain to be further investigated in the future.

We finally presented detailed transfer matrix and FDTD calculations of a novel class of material systems that strongly discriminate light based on the incidence angle, over a broad range of frequencies and irrespective of the polarization. This new class of material systems which enables unprecedented control of light depending on the angle of incidence, is of great importance both to fundamental science and to applications. In fact, further investigation of such novel systems exhibiting an "angular photonic gap" would potentially initiate a whole new fascinating direction in photonics research, as important as the various interesting effects that were explored after photonic crystals exhibiting a "frequency photonic bandgap" were introduced. Moreover, these materials are of prime importance for various technological applications, and particularly in solar-energy conversion where they would enable a perfect green-house effect and thus boost the efficiency of solar-thermal systems up to the Carnot efficiency under ideal circumstances.

Appendices

Appendix A

Efficient weakly-radiative wireless energy transfer: An EIT-like approach

A.1 Analytical solution of the 3-object system in the constant-κ case

The CMT equations Eq. (3.12) admit a simple analytical solution in the special case where the coupling rates $\kappa_{12}(t)$ and $\kappa_{23}(t)$ are independent of time and equal to each other, namely when $\kappa_{12} = \kappa_{23}$ =constant independent of time. After making the following set of substitutions

$$\Sigma \equiv \frac{1}{U} \equiv \frac{\Gamma_A + \Gamma_B}{2\sqrt{2}\kappa} \tag{A.1}$$

$$\Delta \equiv \frac{\Gamma_B - \Gamma_A}{2\sqrt{2}\kappa} \tag{A.2}$$

$$T \equiv \sqrt{2}\kappa t \tag{A.3}$$

we obtain the expressions below for the time-varying amplitudes

$$a_1(T) = \frac{1}{2}e^{-i\omega t}e^{-\Sigma T}\left[\frac{\Delta}{\sqrt{\Delta^2-1}}sinh(\sqrt{\Delta^2-1}T) + cosh(\sqrt{\Delta^2-1}T) + e^{-\Delta T}\right] \quad (A.4)$$

$$a_2(T) = ie^{-i\omega t}e^{-\Sigma T}\frac{1}{\sqrt{\Delta^2-1}}sinh(\sqrt{\Delta^2-1}T) \quad (A.5)$$

$$a_3(T) = \frac{1}{2}e^{-i\omega t}e^{-\Sigma T}\left[\frac{\Delta}{\sqrt{\Delta^2-1}}sinh(\sqrt{\Delta^2-1}T) + cosh(\sqrt{\Delta^2-1}T) - e^{-\Delta T}\right] \quad (A.6)$$

The time t_{opt} at which the energy transferred to R_3 is optimum, can be obtained by setting the time derivative of the energy $|a_3(T)|^2$ in R_3 to zero, and is therefore a solution to the following equation

$$\Sigma\left[\frac{\Delta}{\sqrt{\Delta^2-1}}sinh(\sqrt{\Delta^2-1}T) + cosh(\sqrt{\Delta^2-1}T)\right] -$$

$$\Delta\left[\frac{\sqrt{\Delta^2-1}}{\Delta}sinh(\sqrt{\Delta^2-1}T) + cosh(\sqrt{\Delta^2-1}T)\right] = (\Sigma-\Delta)e^{\Delta T} \quad (A.7)$$

In general, this equation may not have an obvious analytical solution, but it does admit a simple solution in the two special cases that we'll consider below.

In the first special case, we set $\Delta = 0$, and thus we have $\Gamma_A = \Gamma_B = \Gamma$ and $\Sigma = \frac{1}{U} = \frac{\Gamma}{\sqrt{2}\kappa}$. In this case, $T_{opt} \equiv \sqrt{2}\kappa t_{opt}$ becomes

$$T_{opt} = 2\,tan^{-1}\left(\frac{1}{\Sigma}\right) = 2\,tan^{-1}U \quad (A.8)$$

and the efficiency of the 3-object system becomes

$$\eta \equiv \frac{|a_3(T_{opt})|^2}{|a_1(0)|^2} = \left[\frac{U^2}{1+U^2}exp(\frac{-2tan^{-1}U}{U})\right]^2 \quad (A.9)$$

which is just the square of the efficiency of the two-object system [36]. Therefore, when all objects are the same, the efficiency of the 3-object system at optimum is

equal to the square of the efficiency of the 2-object system, and hence is smaller than it.

In the second special case, we set $\Delta = \Sigma = \frac{1}{U} = \frac{\Gamma_B}{2\sqrt{2}\kappa}$, that is to say we set $\Gamma_A = 0$. The analytical expressions for T_{opt} and η become respectively

$$T_{opt} = \begin{cases} \frac{\pi U}{\sqrt{U^2-1}}, & U > 1 \\ \infty, & U \leq 1 \end{cases} \tag{A.10}$$

$$\eta = \begin{cases} \frac{1}{4}\left[1 + \exp\left(\frac{-\pi}{\sqrt{U^2-1}}\right)\right]^2, & U > 1 \\ \frac{1}{4}, & U \leq 1 \end{cases} \tag{A.11}$$

Therefore, the optimum efficiency in this case, is larger when $\kappa > \frac{\Gamma_B}{2\sqrt{2}}$.

A.2 Resolution of apparent paradox in EIT-like scheme

As we said earlier in the text, the explanation of the EIT-like scheme in terms of the adiabatic following of the eigenstate $\vec{V}_1$, seems to be puzzling and somewhat paradoxical. The reason is that energy is efficiently transferred through the intermediate resonator R_2 without ever being in it. This apparent contradiction can be resolved by looking at the detailed contributions to the time-rate of change of the energy E_2 in R_2. Since the energy in R_2 at time t is $E_2(t) = |a_2(t)|^2$, one can use the CMT Eq. (3.12) and calculate the power $dE_2(t)/dt$ through R_2, to obtain

$$\frac{d|a_2|^2}{dt} = -2\Gamma_B|a_2|^2 - 2\kappa_{12}\mathrm{Im}(a_2^* a_1) + 2\kappa_{23}\mathrm{Im}(a_3^* a_2). \tag{A.12}$$

The first term on the right-hand side of this equation corresponds to the total power lost in R_2. The second term can be identified with the time-rate $P_{12}(t)$ of energy transfer from R_1 to R_2, namely $P_{12}(t) = -2\kappa_{12}(t)\mathrm{Im}(a_2^*(t)a_1(t))$. Similarly, the third term can be identified with the time-rate $P_{23}(t)$ of energy transfer from R_2 to R_3: $P_{23}(t) = 2\kappa_{23}(t)\mathrm{Im}(a_3^*(t)a_2(t))$. Note that because $P_{12}(t)$ represents the rate

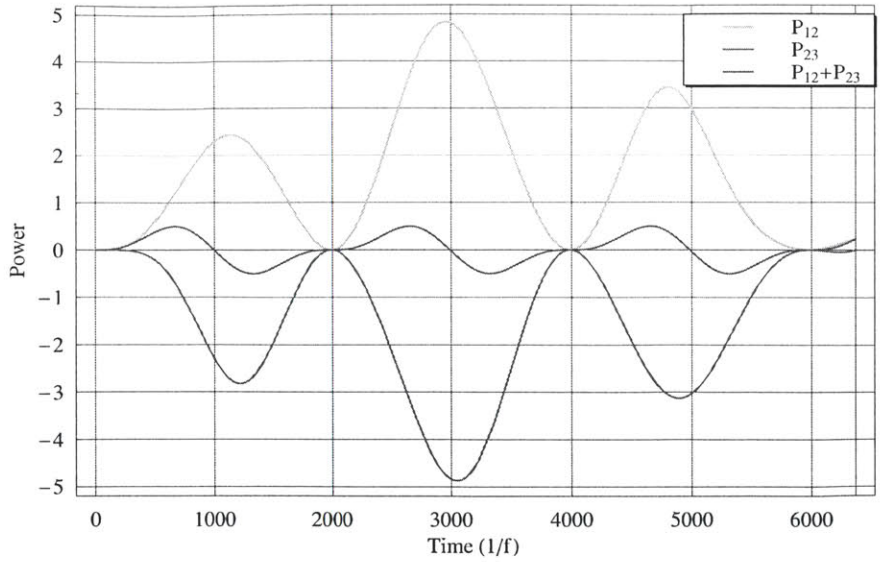

(a)

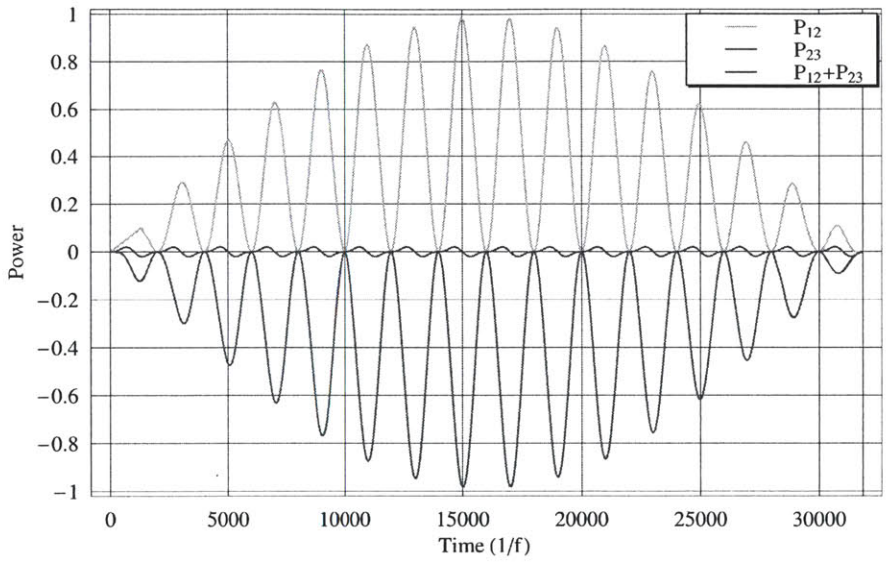

(b)

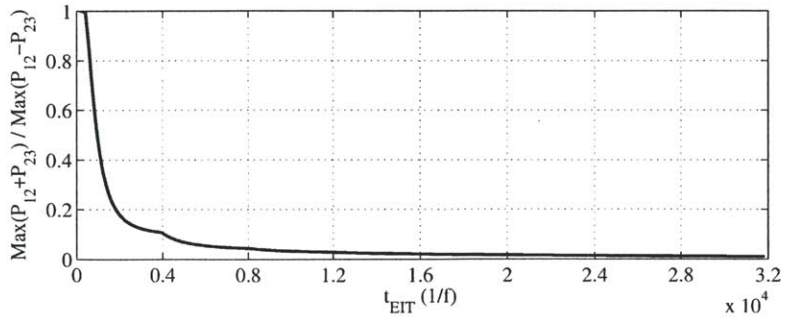

(c)

Figure A-1: (a) P_{12}, P_{23} and $P_{12} + P_{23}$ as functions of time for $\Gamma_A = \Gamma_B = 0$, $Q_\kappa = 1000$, and $t_{EIT} = 6366.2(1/f)$. (b) Same plot as in (a) but with t_{EIT} 5 times longer. (c) $\mathrm{Max}(P_{12} + P_{23})/\mathrm{Max}(P_{12} - P_{23})$ versus t_{EIT} for $\Gamma_A = \Gamma_B = 0$ and $Q_\kappa = 1000$.

at which energy gets into R_2 (coming from R_1), this term will be positive. Similarly, because $P_{23}(t)$ is the rate at which energy gets out of R_2 (going to R_3), this term will be negative. For simplicity, we will focus on the case where $\Gamma_A = \Gamma_B = 0$, and take the time variation of the coupling rates to be given by Eq. (3.10)-(3.11). In this case, the total energy in the 3-object system is conserved, and the change in the energy E_2 can arise only from the exchange of energy between R_1 and R_2, and between R_2 and R_3. In this special case, the rate of change of E_2, which equals the sum $P_{12}+P_{23}$, is oscillatory in time with amplitude A_{sum}. It turns out that as the transfer time t_{EIT} gets longer, the peak amplitude A_{sum} of the sum $P_{12} + P_{23}$ approaches zero. This means that at the moment when energy reaches R_2 from R_1, it leaves R_2 immediately to R_3. Therefore, $dE_2(t)/dt$ is almost zero $\forall\, t$, and the energy in R_2 remains approximately equal to its initial value of zero throughout the EIT-like transfer, despite the fact that all the energy initially in R_1 goes through R_2 as it gets transferred to R_3. To illustrate this point, we consider again the case $\Gamma_A = \Gamma_B = 0$, and choose the coupling rate κ such that $Q_\kappa = 1000$. In Fig. A-1 (a), we plot the powers P_{12}, P_{23} and their sum as functions of time when the duration of the transfer is $t_{EIT} = 6366.2(1/f)$. In Fig. A-1 (b), we repeat the same plots but now with a transfer time 5 times longer. As can be seen by comparing Fig. A-1 (a) and Fig. A-1 (b), we find that the relative amplitude A_{sum}, compared to characteristic magnitudes of P_{12} and P_{23}, has dramatically decreased. To get a quantitative estimate of this decrease in the amplitude of $P_{12} + P_{23}$, we show in Fig. A-1 (c), the ratio of A_{sum} over the maximum of $P_{12} - P_{23}$ as a function of t_{EIT}. We find that, indeed, as the transfer time gets longer, meaning that the adiabatic condition is better satisfied, the amplitude A_{sum} gets smaller and smaller compared to the peak of P_{12}, and consequently the deviation of the energy in R_2 from its initial zero value becomes negligible. Therefore, one way to look at why the EIT mechanism works so well, is to note that the EIT-approach ensures that the energy leaves R_2 (to R_3) as soon as it reaches R_2 (from R_1).

Bibliography

[1] Bohren C.F., Huffman D.R., *Absorption and scattering of light by small particles* (Wiley, 1983).

[2] P. A. Franken, A. E. Hill, C. W. Peters, and G. Weinreich, "Generation of Optical Harmonics," Phys. Rev. Lett. **6**, 118-119 (1961).

[3] John D. Joannopoulos, Robert D. Meade, Joshua N. Winn, *Photonic Crystals: Molding the Flow of Light* (Princeton University Press, 1995).

[4] H. A. Haus, *Waves and Fields in Optoelectronics* (Prentice-Hall, New Jersey, 1984).

[5] Pochi Yeh, *Optical Waves in Layered Media*, Chapter 9 pages 201-213 (John Wiley & Sons Inc, 1988).

[6] Ardavan Farjadpour, David Roundy, Alejandro Rodriguez, Mihai Ibanescu, Peter Bermel, J. D. Joannopoulos, Steven G. Johnson, and Geoffrey Burr, "Improving accuracy by subpixel smoothing in the finite-difference time domain," Opt. Lett. **31**, 2972-2974 (2006).

[7] J. A. Stratton, *Electromagnetic Theory* (McGraw-Hill, New York, 1941).

[8] H. C. van de Hulst, *Light Scattering by Small Particles* (Dover, New York, 1981).

[9] Craig F. Bohren, Am. J. Phys. **51**, 323 (1983).

[10] K. Bergmann, H. Theuer, and B. W. Shore, Reviews of Modern Physics **70**, 3, p.1003-1023 (1998).

[11] E. Purcell, "Spontaneous emission probabilities at radio frequencies," Phys. Rev. **69**, 681 (1946).

[12] Hideo Kosaka, Takayuki Kawashima, Akihisa Tomita, Masaya Notomi, Toshiaki Tamamura, Takashi Sato, and Shojiro Kawakami, "Self-collimating phenomena in photonic crystals," Appl. Phys. Lett. **74**, 1212-1214 (1999).

[13] Lijun Wu, Michael Mazilu, and Thomas F. Krauss, "Beam Steering in Planar-Photonic Crystals:From Superprism to Supercollimator," J. Lightwave Technol. **21**, 561-566 (2003).

[14] Dennis W. Prather, Shouyuan Shi, David M. Pustai, Caihua Chen, Sriram Venkataraman, Ahmed Sharkawy, Garrett J. Schneider, and Janusz Murakowski, "Dispersion-based optical routing in photonic crystals," Opt. Express **29**, 50-52 (2004).

[15] Jonghwa Shin and Shanhui Fan, "Conditions for self-collimation in three-dimensional photonic crystals," Opt. Lett. **30**, 2397-2399 (2005).

[16] Peter T. Rakich, Marcus S Dahlem, Sheila Tandon, Mihai Ibanescu, Marin Soljačić, Gale S. Petrich, John D. Joannopoulos, Leslie A. Kolodziejski and Erich P. Ippen, "Achieving centimetre scale super collimation in a large area 2D photonic crystal," Nature Mater. **5**, 93-96 (2006).

[17] Ta-Ming Shih, Andre Kurs, Marcus Dahlem, Gale Petrich, Marin Soljacic, Erich Ippen, Leslie Kolodziejski , Katherine Hall, and Morris Kesler, "Supercollimation in photonic crystals composed of silicon rods," Appl. Phys. Lett. **93**, 131111 (2008).

[18] Dmitry Chigrin, Stefan Enoch, Clivia Sotomayor Torres, and Grard Tayeb, "Self-guiding in two-dimensional photonic crystals," Opt. Express **11**, 1203-1211 (2003).

[19] Marian Florescu, Hwang Lee, Irina Puscasu, Martin Pralle, Lucia Florescu, David Z. Ting and Jonathan P. Dowling, "Improving solar cell efficiency us-

ing photonic band-gap materials," Solar Energy Materials and Solar Cells **91**, 1599-1610 (2007).

[20] Martin A. Green, "Limiting photovoltaic monochromatic light conversion efficiency," Progress in photovoltaics **9**, 257-261 (2001).

[21] Stephan Fahr, Carolin Ulbrich, Thomas Kirchartz, Uwe Rau, Carsten Rockstuhl, and Falk Lederer, "Rugate filter for light-trapping in solar cells," Optics Express **16**, 9332-9343 (2008).

[22] C. Ulbrich, S. Fahr, M. Peters, J. Upping, T. Kirchartz, C. Rockstuhl, J. C. Goldschmidt, P. Loper, R.Wehrspohn, A. Gombert, F. Lederer, and U. Rau, "Directional selectivity and light-trapping in solar cells," Photonics for Solar Energy Systems II 7002, 70020A (2008).

[23] Hitoshi Kuwata *et al.*, Appl. Phys. Lett. **83**, 4625 (2003).

[24] Roger G. Newton, *Scattering Theory of Waves and Particles* (Dover, New York, 2002).

[25] Marin Soljačić, Elefterios Lidorikis, Lene Vestergaard Hau, and J. D. Joannopoulos, Phys. Rev. E. **71**, 026602 (2005).

[26] P. Laven, MiePlot v3.4 (2006), http://www.philiplaven.com/mieplot.htm.

[27] J. D. Jackson, *Classical Electrodynamics* (Wiley, New York, 1999), pp. 766-768.

[28] J-L Basdevant, J. Rich, M. Spiro, *Fundamentals in Nuclear Physics* (Springer, New York, 2005).

[29] W. N. Cottingham, D.A. Greenwood, *An Introduction to Nuclear Physics* (Cambridge University Press, Cambridge, 2001).

[30] J. J. Sakurai, *Modern Quantum Mechanics* (Addison-Wesley, Reading, Massachusetts, 1994).

[31] J. M. Fernandez, and J. A. Borras, Contactless battery charger with wireless control link, US patent number 6,184,651 issued in February 2001.

[32] L. Ka-Lai, J. W. Hay, and P. G. W. Beart, Contact-less power transfer, US patent number 7,042,196 issued in May 2006 (SplashPower Ltd., <www.splashpower.com>)

[33] A. Esser, H.-C. Skudenly, IEEE Trans. Industry Appl. 27 (1991) 872.

[34] J. Hirai, T.-W. Kim, A. Kawamura, IEEE Trans. Power Electron. 15 (2000) 21.

[35] G. Scheible, B. Smailus, M. Klaus, K. Garrels, and L. Heinemann, System for wirelessly supplying a large number of actuators of a machine with electrical power, US patent number 6,597,076, issued in July 2003 (ABB, <www.abb.com>).

[36] Aristeidis Karalis, John D.Joannopoulos, and Marin Soljacic, Annals of Physics **323**, p.34 (2008).

[37] Andre Kurs, Aristeidis Karalis, Robert Moffatt, J.D.Joannopoulos, Peter Fisher, and Marin Soljacic, Science **317**, p.83 (2007).

[38] Stephen E. Harris, Phys. Today **50**, 7, p. 36-42.

[39] J. R. Kuklinski, U. Gaubatz, F. T. Hioe, and K. Bergmann, Phys. Rev. A **40**, 6741 - 6744 (1989).

[40] U. Gaubatz, P. Rudecki, S. Schiemann, and K. Bergmann, J. Chem. Phys. **92**, 5363 (1990).

[41] P. D. Maker, R. W. Terhune, M. Nisenhoff, and C. M. Savage, "Effects of Dispersion and Focusing on the Production of Optical Harmonics," Phys. Rev. Lett. **8**, 21-22 (1962).

[42] J. A. Giordmaine, "Mixing of Light Beams in Crystals," Phys. Rev. Lett. **8**, 19-20 (1962).

[43] M. Bass, P. A. Franken, A. E. Hill, C. W. Peters, and G. Weinreich, "Optical Mixing," Phys. Rev. Lett. **8**, 18-18 (1962).

[44] J. A. Armstrong, N. Bloembergen, J. Ducuing, and P. S. Pershan, "Interactions between Light Waves in a Nonlinear Dielectric," Phys. Rev. **127**, 1918-1939 (1962).

[45] N. Bloembergen and Y. R. Shen, "Quantum-Theoretical Comparison of Nonlinear Susceptibilities in Parametric Media, Lasers, and Raman Lasers," Phys. Rev. **133**, A37-A49 (1964).

[46] G. Eckardt, R. W. Hellwarth, F. J. McClung, S. E. Schwartz, D. Weiner, and E. J. Woodbury, "Stimulated Raman Scattering From Organic Liquids," Phys. Rev. Lett. **9**, 455 (1962).

[47] Jeff Squier, and Michiel Müller, "High resolution nonlinear microscopy: a review of sources and methods for achieving optimal imaging," Rev. Sci. Instrum. **72**, 2855-2867 (2001).

[48] John M. Dudley, Christophe Finot, David J. Richardson, and Guy Millot, "Self-similarity in ultrafast nonlinear optics," Nature Physics **3**, 597-603 (2007).

[49] Yuri Kivshar, "Spatial solitons: Bending light at will," Nature Physics **2**, 729-730 (2006).

[50] Günter Steinmeyer, "Laser physics: Terahertz meets attoscience," Nature Physics **2**, 305-306 (2006).

[51] Govind P. Agrawal, Akira Hasegawa, Yuri Kivshar, and Stefan Wabnitz, "Introduction to the Special Issue on Nonlinear Optics," IEEE J. Sel. Top. In Quantum Electron. **8**, 405-407 (2002).

[52] Bradley Ferguson, and Xi-Cheng Zhang, "Materials for terahertz science and technology," Nature Materials **1**, 26-33 (2002).

[53] E. Mueller, "Terahertz radiation sources for imaging and sensing applications," Photonics Spectra 40, 60 (2006).

[54] Marin Soljačić, and J.D. Joannopoulos, "Enhancement of non-linear effects using photonic crystals," Nature Materials **3**, 211-219 (2004).

[55] G. DAguanno, M. Centini, M. Scalora, C. Sibilia, Y. Dumeige, P. Vidakovic, J. A. Levenson, M. J. Bloemer, C. M. Bowden, J. W. Haus, and M. Bertolotti, "Photonic band edge effects in finite structures and applications to $\chi(2)$ interactions," Phys. Rev. E. **64**, 016609 (2001).

[56] Taflove A., *Computational Electrodynamics: The Finite-Difference Time-Domain Method* (Artech House, Norwood, 1995).

[57] Jorge Bravo-Abad, Alejandro Rodriguez, Peter Bermel, Steven G. Johnson, John D. Joannopoulos, and Marin Soljačić, "Enhanced nonlinear optics in photonic-crystal microcavities," Opt. Express **15**, 16161-16176 (2007).

[58] Thierry Laroche, Fadi Issam Baida, and Daniel Van Labeke, "Three-dimensional finite-difference time-domain study of enhanced second-harmonic generation at the end of a apertureless scanning near-field optical microscope metal tip ," J. Opt. Soc. Am. B **22**, 1045-1051 (2005).

[59] Kazuaki Sakoda, and Kazuo Ohtaka, "Optical response of three-dimensional photonic lattices: Solutions of inhomogeneous Maxwells equations and their applications," Phys. Rev. B **54**, 5732-5741 (1996).

[60] Kazuaki Sakoda, and Kazuo Ohtaka, "Sum-frequency generation in a two-dimensional photonic lattice," Phys. Rev. B **54**, 5742-5749 (1996).

[61] Chiyan Luo, Mihai Ibanescu, Evan J. Reed, Steven G. Johnson, and J. D. Joannopoulos, "Doppler Radiation Emitted by an Oscillating Dipole Moving inside a Photonic Band-Gap Crystal," Phys. Rev. Lett. **96**, 043903 (2006).

[62] D. H. Auston, K. P. Cheung, J. A. Valdmanis, and D. A. Kleinman, "Cherenkov Radiation from Femtosecond Optical Pulses in Electro-Optic Media," Phys. Rev. Lett. **53**, 1555-1558 (1984).

[63] Mihai Ibanescu, Evan J. Reed, and J. D. Joannopoulos, "Enhanced Photonic Band-Gap Confinement via Van Hove Saddle Point Singularities," Phys. Rev. Lett. **96**, 033904 (2006).

[64] Guoqing Chang, Charles J. Divin, Jun Yang, Malakeh A. Musheinish, Steven L. Williamson, Almantas Galvanauskas, and Theodore B. Norris, "GaP waveguide emitters for high power broadband THz generation pumped by Yb-doped fiber lasers ," Opt. Express **15**, 16308-16315 (2007).

[65] Tadao Tanabe, Ken Suto, Jun-ichi Nishizawa, Kyosuke Saito, and Tomoyuki Kimura, "Frequency-tunable terahertz wave generation via excitation of phonon-polaritons in GaP," J. Phys. D: Applied Physics **36**, 953-957 (2003).

[66] Steven G. Johnson and J. D. Joannopoulos, "Block-iterative frequency-domain methods for Maxwell's equations in a planewave basis ," Opt. Express **8**, 173-190 (2001).

[67] Robert W. Boyd, *Nonlinear Optics* (Academic Press, 2002).

[68] J. N. Winn, Y. Fink, S. Fan, and J. D. Joannopoulos, "Omnidirectional reflection from a one-dimensional photonic crystal," Opt. Lett. **23**, 1573-1575 (1998).

[69] P. St. J. Russella, S. Tredwella and P. J. Roberts, "Full photonic bandgaps and spontaneous emission control in 1D multilayer dielectric structures," Opt. Commun. **160**, 66-71 (1999).

[70] D.N. Chigrin, A.V. Lavrinenko, D.A. Yarotsky and S.V. Gaponenko, "Observation of total omnidirectional reflection from a one-dimensional dielectric lattice," Appl. Phy. A: Materials Science & Processing **68**, 25-28 (1999).

[71] R. D. Meade, A. Devenyi, J. D. Joannopoulos, O. L. Alerhand, D. A. Smith, and K. Kash, "Novel applications of photonic band gap materials: low-loss bends and high Q cavlties," J. Appl. Phys. **75**, 4753-4755 (1994).

[72] S. Fan, P. R. Villeneuve, J. D. Joannopoulos, and E. F. Schubert, "High Extraction Efficiency of Spontaneous Emission from Slabs of Photonic Crystals," Phys. Rev. Lett. **78**, 3294-3297 (1997).

[73] Eli Yablonovitch, "Inhibited Spontaneous Emission in Solid-State Physics and Electronics ," Phys. Rev. Lett. **58**, 2059-2062 (1987).

[74] C. Luo, S. G. Johnson, and J. D. Joannopoulos, "All-angle negative refraction in a three-dimensionally periodic photonic crystal," Appl. Phys. Lett. **81**, 2352-2354 (2002).

[75] Hideo Kosaka, Takayuki Kawashima, Akihisa Tomita, Masaya Notomi, Toshiaki Tamamura, Takashi Sato, and Shojiro Kawakami, "Superprism phenomena in photonic crystals," Phys. Rev. B **58**, R10096-R10099 (1998).

[76] M. Soljačić and J. D. Joannopoulos, "Enhancement of nonlinear effects using photonic crystals ," Nature Mater. **3**, 211-219 (2004).

[77] M. Soljačić, E. Lidorikis, J. D. Joannopoulos, and L. V. Hau , "Ultralow-power all-optical switching," Appl. Phys. Lett. **86**, 171101 (2005).

[78] D. L. C. Chan and M. Soljačić, and J. D. Joannopoulos, "Thermal emission and design in 2D-periodic metallic photonic crystal slabs", Opt. Express **14**, 8785 (2006).

[79] Ashcroft & Mermin, *Solid State Physics* (Saunders College, 1976).

[80] M. L. Povinelli, Steven G. Johnson, Shanhui Fan, and J. D. Joannopoulos, "Emulation of two-dimensional photonic crystal defect modes in a photonic crystal with a three-dimensional photonic band gap," Phys. Rev. B **64**, 075313 (2001).

[81] As explained in [21], one could embed a slab of our proposed 2D PhC into a 3D PhC having a complete photonic bandgap, and design things in such a way that the extended frequency range supporting supercollimation falls inside the complete bandgap of the 3D PhC. This would prevent radiation losses from the 'slab version' of our proposed 2D PhC structure.

[82] Demetrios N. Christodoulides, Falk Lederer & Yaron Silberberg, "Discretizing light behaviour in linear and nonlinear waveguide lattices," Nature **424**, 817 (2003).

[83] T. Rowan, "Functional Stability Analysis of Numerical Algorithms," Ph.D. thesis, Department of Computer Science, University of Texas at Austin, (1990).

[84] C. Luo, M. Soljacic, and J. D. Joannopoulos, "Superprism effect based on phase velocities," Opt. Lett., **29**, 745747 (2004).

[85] Eugene Hecht, *Optics*, Chapter8 (pages 331-339), Fourth Edition, (Addison-Wesley, 2002)

[86] John D. Joannopoulos, Steven G. Johnson, Joshua N. Winn, and Robert D. Meade, *Photonic Crystals: Molding the Flow of Light*, second edition (Princeton University Press, 2008).

[87] Pochi Yeh, *Optical Waves in Layered Media*, Chapter 9 page 209 (John Wiley & Sons Inc, 1988).

[88] Since we know that a TM reflection window opens at 45^o, we choose the relative thickness h_A of layer A such as to maximize the size of the TM fractional gap, which happens at the quarter-wave condition ($h_A n_A^{TM} \cos\theta_A^{TM} \omega_o/c = h_B n_B^{TM} \cos\theta_B^{TM} \omega_o/c$), ω_o being the central frequency of the gap. This results in $h_A = 0.46 \times a$.

[89] In a 2D square lattice of dielectric rods, modes having their E-field along the rods are substantially more concentrated inside the rods and therefore experience

the high ϵ of the rods. On the other hand, modes having their E-field in the periodicity plane experience average ϵ smaller than that along the rods, hence the anisotropy in effective epsilon. Our frequency domain simulations (not discussed here) show that in the low frequency limit, the metamaterial indeed has effective $\epsilon = (1.23, 1.23, 2.43)$.

[90] Pochi Yeh, *Optical Waves in Layered Media*, Chapter 5 (pages 102-110) and Chapter 6 (pages 118-128) (John Wiley & Sons Inc, 1988). In TMM, we model each layer as being uniform; e.g. in the case of layer A of Fig. 1, uniform $\epsilon = (1.23, 1.23, 2.43)$.

[91] Note that a structure having $\varepsilon_A = \mu_A = (\gamma_1, \gamma_1, \gamma_2)$ and $\varepsilon_B = \mu_B = \gamma_1$ would work equally well and would have a larger fractional frequency gap (at the quarter-wave condition which is satisfied differently at different incidence angles), however the structure that we analyze in Fig. 6-2 offers somewhat more flexibility in the material choice, in the sense that anisotropic ε and μ do not have to occur in the same material.

[92] Note that this choice of $h_A = h_B$ does not result in the largest possible fractional gap for either polarization, which actually occurs at the quarter-wave condition, satisfied non-simultaneously for the two different polarizations when $\varepsilon_A = \mu_B = (\gamma_1, \gamma_1, \gamma_2 \neq \gamma_1)$.

[93] J. B. Pendry, A. J. Holden, D. J. Roddins, and W. J. Stewart, IEEE transactions on microwave theory and techniques **47**, NO. 11, November 1999.

[94] T. Barwicz, M. R. Watts, M. A. Popovic, P. T. Rakich, L. Socci, F. X. Kaertner, E. P. Ippen, and H. I. Smith, Nature Photonics, 1, 57, (2007).